DYNAMICS MODELING AND CONTROL OF A QUAD-ROTOR HELICOPTER

MOHAMMED RAJU HOSSAIN

Dynamics Modeling and Control of a Quad-rotor Helicopter

by

© Mohammed Raju Hossain

A thesis submitted to the

School of Graduate Studies

in partial fulfilment of the

requirements for the degree of

Master of Engineering

Faculty of Engineering & Applied Science

Memorial University of Newfoundland

September 2010

St. John's Newfoundland

to my Mom & Dad

Abstract

Unmanned Aerial Vehicles (UAVs) have become a promising field of research due to the enormous potential for both military and civilian applications. This thesis focuses on increasing the autonomy of one type of rotary wing UAV; namely a Quadrotor Helicopter.

In this work a detailed mathematical model was introduced for simulation of the dynamics and control of this system. The dynamic model evolved from a simple set of equations, valid only for hovering, to a complex mathematical model with more realistic aerodynamic factors like thrust factor and drag factor. A simple yet precise tool was developed to measure these aerodynamic factors. An intelligent vision based control technique has been proposed for the critical, near-hovering flight of the vehicle. Finally, a platform was developed and a PD controller was implemented with inertial sensors in order to prepare the platform for implementing the vision-based control in the future.

Acknowledgements

I would like to express my deepest appreciation for my supervising professor Dr. Nicholas Krouglicof who throughout this work offered his guidance and conveyed a spirit of adventure in regard to this research. Without his persistent help and encouragement this thesis would not have been possible.

I gratefully thank my family and friends for their patience and inspirations.

Contents

List of Tables

List of Figures

Chapter 1

Introduction

Flying objects and robotics have always been of great interest to human beings. Advancements in modern electronics and sensor technology have directed human interest towards unmanned flying for a variety of applications including surveillance, security, and exploration. This thesis focuses on the study of a rotor based unmanned aerial vehicle (UAV) capable of vertical takeoff/landing (VTOL). This UAV is referred to as a "quad-rotor helicopter" because of its structure and four propeller configuration.

1.1 Quad-rotor UAV

A quad-rotor is an under-actuated, dynamic vehicle with four actuating propellers and six degrees of freedom; yaw, pitch, roll as well as translational movement along three axes. Unlike regular helicopters that have variable pitch angle rotors, a quad-rotor helicopter has four fixed-pitch angle rotors. The basic motions of a quad-rotor are generated by varying the speeds of all four propellers, thereby changing the lift forces. The helicopter tilts towards the direction of the slow spinning rotor, which

enables acceleration along that direction. Therefore, control of the tilt angles and the motion of the helicopter are closely related and estimation of orientation (roll and pitch) is critical. In order to balance the moments created by propeller rotation, two opposing propellers rotate in the clockwise direction and the other two rotate in the counter-clockwise direction. This mechanism eliminates the need for the tail rotor used in a regular helicopter. This principle is also used to produce the desired yaw motions. A good controller can properly adjust the speed of each rotor to get desired state change.

1.2 Why Quad-rotor UAV?

The most established UAVs in operation today are Fire Scout, Predator, Global Hawk, Yamaha RMAX. Some of them are fixed wing while others employ rotor based wings; however, all of them perform in tele-operated mode [1]. This semi-autonomous (tele-operated) strategy requires the ground operator's full attention to keep the veheicle under control. For this reason there is a requirement for modern UAVs to become more autonomous. Today many UAVs have on-board control systems that reduce the amount of control required from the ground operator. A typical example of this kind of on-board control includes observation of UAV states and commands for recording surveillance video, identifying targets, navigating to certain GPS waypoints, returning to base, etc. This type of control is well established for fixed-wing UAVs; however, research into autonomous, on-board control of rotor-based UAV is a relatively new direction [1].

Another motivation behind this work is the broad field of applications of UAVs in

both military and civilian scenarios as well as the limitations of manned vehicles in special environments. Some of these applications are surveillance, imaging and data collection in dangerous environments, indoor navigation and mapping. The selection of this type of quad-rotor UAV was due to its unique ability for vertical, stationary and low speed flight. Several structures and configurations has been developed in this field so far (e.g., fixed wing planes, single rotor helicopter, bird-like aircraft, two-rotor helicopter, four-rotor helicopters). Each of these has its own advantages and drawbacks. The structure chosen in this research has good maneuverability, simple in terms of mechanics and good payload capacity; however, high energy consumption is one of the main drawbacks.

1.3 Objectives

The initial goal of this thesis was to understand the quad-rotor UAV dynamics by developing detailed analytical and computational models as well as implementing a control strategy for improved stability. The kinematic/dynamic study provides a better understanding of the physics behind the quad-rotor behavior. The control modeling will assist in calculating appropriate control gains before implementing a controller.

The next immediate goal was to measure the parameters involved in the simulation in order to increase the accuracy of the model. There are a variety of parameters that play a vital role in the dynamics of the quad-rotor including rotor parameters (thrust constant, drag constant, rotational inertia) and platform parameters (size, weight, moments of inertia).

The final goal is to construct a cost effective quad-rotor platform to validate the mathematical model and implement a control strategy for stabilizing the vehicle both in terms of orientation and position. Stabilization is accomplished through the integration of a non-contact, real-time sensor system that can track targets on the ground and use the information as feedback for controlling the UAVs position and orientation. The ultimate goal is to land or take off on a moving platform by tracking targets placed on that platform/ground.

1.4 Contributions

The main contributions of this work were divided in four major steps.

- A faithful mathematical representation of the quad-rotor vehicle was developed in order to analyze the system as well as model the control strategy.
- A UAV Propeller dynamometer was developed to characterize the combined motor, controller and propeller system as well as to identify the aerodynamic factors involved in the dynamic model.
- An intelligent landing (with the associated mathematical model) was proposed based on a single outwardly looking camera and a ground target.
- A prototype quad-rotor helicopter was developed and controlled.

1.4.1 Analytical and Computational Modeling

An accurate mathematical model was developed in successive steps. The first version was a simple model describing the vehicle in hovering flight where only yaw, pitch, roll

and altitude were controlled (i.e., attitude and altitude). This model was evaluated using bond graph modeling and simulation techniques (specifically 20-Sim bond graph based software). Chapter 3 presents this dynamic model as well the associated control strategy. The model then evolved into a more complete form through the incorporation of X-Y position control resulting in a complete 6 DOF dynamic representation. Chapter 5 describes the more elaborate model. Matlab-Simulink was used as a tool for simulation of this model. Both Proportional-Derivative (PD) and Proportional-Integral Derivative (PID) controllers were evaluated for stabilization and control of the system.

1.4.2 Precession Tool for Characterizing small UAV Propeller

To ensure fidelity in the mathematical modeling, propeller characterization became an important issue. A high resolution dynamometer was developed to measure the propeller characteristics and refine the dynamic model for higher accuracy. Six load cells and a 24 bit analog-to-digital converter were used for this purpose. A miniature load frame was developed for decoupling the thrust and torque force components produced by the propeller.

1.4.3 Vision Based Quad-rotor Stabilization Technique

A vision based technique for controlling all six degrees of freedom of a quad-rotor helicopter is proposed. Unlike many other landing/take-off approaches using dual cameras, this approach employs a pose estimation technique based on a single camera.

The camera is on-board and a ground based landmark (i.e., landing pad) consisting of five control points serves as a visual reference for estimating pose. By continuously monitoring the position of the control points with the on-board camera, the relative orientation and position of the quad-rotor platform relative to the landing pad is calculated. The vision-based pose information serves as feedback to a PD controller which controls the vehicle. The algorithm and its implementation are described in chapter 5.

1.4.4 Quad-rotor Platform Development

The "open-source" quad-rotor platform was developed through the integration of a number of systems and devices. Four brushless direct current (BLDC) motors with appropriate controllers were used to directly drive the propellers for producing and controlling thrust in the system. In terms of on-board sensor platforms, Micro-Electro-Mechanical (MEM) accelerometers and gyros were used to measure attitude and angular rate information. The data processing and control algorithms were implemented on a small format single board computer based on a Vortex processor. This board includes a variety of analog and digital IO interfaces to control the BLDC motors and read the sensor data.

1.5 Thesis Outline

This thesis consists of three manuscripts, the first two publications has been accepted and published and the third one has been submitted for publication.

- **Chapter 1** introduces the thesis and the research topic. It defines the ultimate

objectives of this work and provides a synopsis of the goals and the outcomes obtained.

- **Chapter 2** is a survey of the state of art in the field of UAV research. It also presents other related research work.

- **Chapter 3** is the first published manuscript that evaluates the basic dynamic model of a quad-rotor helicopter focusing only on hovering which refers to the stabilization of attitude and altitude but not position. The adopted method for implementing the simulation model was the bond graph modeling technique.

- **Chapter 4** is the second publication, which describes the aforementioned high performance propeller dynamometer for characterizing small UAV propellers. This chapter presents the method and discusses the results obtained from this specialized hardware.

- **Chapter 5** is the third publication which is pending publication. This paper proposes a vision augmented control technique for quad-rotor vehicles specifically for take-off and landing or flying relative to another unmanned vehicle. The chapter provides the complete model with simulation results using the proposed technique.

- **Chapter 6** presents the quad-rotor hardware development along with the implementation of a controller and validation of its performance.

- **Chapter 7** reviews the research work and outcomes focusing on the challenges faced during each step of the development and how they have been overcome. Possible future work is also addressed.

- **Appendix A** provides the mathematical derivation of a quad-rotor vehicle model. The dynamics are explained from the basic concept of Newton-Euler formalism. Particular attention is given to the quad-rotor architecture and maneuvering mechanism.

- **Appendix B** presents an introduction to bond graph modeling. The importance of this appendix lies in understanding the first simulation model developed to evaluate the control of a quad-rotor helicopter.

- **Appendix C** presents rotational inertia theory which describes the dynamic behavior of a body in rotation about a fixed axis.

- **Appendix D** discusses the analytical identification of thrust and drag factors for a propeller.

The status of each publication and contributions made by the authors are provided as a preface before each paper/chapter.

Chapter 2

Literature Review

2.1 Brief History of Helicopter

The history of the helicopter is relatively short in comparison with fixed-wing aircraft. Probably the first flying toy was a Chinese top inspired by auto rotating-seeds of trees. In 1490 Leonardo Da Vinci created the Helical Air Screw (Figure 2.1a) which it is often cited as the first serious attempt to produce a working helicopter.

(a) Air Screw (b) Gyro Plane no: 1

Figure 2.1: Historical Images of Helicopter

In 1863, Ponton d'Amecourt was the first person to use the word helicopter. He also developed a coaxial helicopter with steering capabilities. Inspired by this, in 1877 Forlanini developed a reduced scale, steam powered model which was neither steerable nor stable. Then, in 1887, Frenchmen Louis and Jacques Breguet in association with Professor Charles Richet developed the manned "Gyroplane no. 1" (Figure 2.1b), a large quad-rotor with double layers of propellers; however, it lacked any control strategy. This is the first known quad-rotor aerial vehicle in history. In 1907 the first manually controlled free flight was achieved by Paul Cornu. This is considered as the beginning of helicopter [2] flight.

2.2 Evolution of UAV

Right after the development of the automatic gyroscopic stabilizer by Dr. Peter Cooper and Elmer Sperry, a US Navy N-9 trainer aircraft was converted into the first radio controlled UAV using the above mentioned technology which helped to keep the aircraft straight and level during autonomous flight. The first fixed wing UAV was tested during World War I but was not deployed in combat. The first battlefield deployment of UAVs was by the Germans during World War II [2]. The potential was later recognized by the US and Israel who initiated the commercial development of UAVs with the incorporation of more sophisticated technology (e.g., Predator). Motivated by the tremendous technological advancements of World War II, US based Gyrodyne became the first company to commercialize an unmanned helicopter, the Hummingbird. In the years that followed academic researchers started showing interest in the development of unmanned helicopters. Extensive research is currently being

conducted on UAVs of various configurations and sizes for both military and civilian applications such as search and rescue. A brief survey of these projects is presented in [3]. Due to the application of UAVs in special environments, researchers have started focusing on small rotor-based UAVs where the challenges include miniaturization, aerodynamics, control, autonomy and above all energy storage.

2.3 Rotor Based UAV

Although fixed wing UAVs are more stable when compared to rotor based UAVs, the latter offer advantages when it comes to hovering, "perching", flying close to an object of interest, or maneuvering in confined environments (e.g., indoors). Not only do fixed wing UAVs require large areas for takeoff and landing, they cannot back up, make sharp turns, or stop and maintain a specific position. Because of these limitations fixed wing UAVs cannot observe objects at close proximity making it difficult to obtain high resolution images of an object of interest. Close inspection of hazardous environments, indoor/outdoor surveillance, and stationary monitoring of objects of interest are just a few mission scenarios where rotor based UAVs offer advantages over fixed wing UAV. Other applications of rotor based UAVs appearing in the literature include remote sensing [4], aerial mapping [5], tracking [6], inspection, surveillance [7].

2.4 State of the Art

Among the researches in rotary wing UAVs, most of the attention has been focused on quad-rotor type configurations. Some projects are based on commercially available platforms including Draganflyer [8], MD4-200 [9], and X-UFO [10]. Some researchers have preferred building their own platforms such as X4-Flyer, Mesicopter, and STAR-MAC. Hybrid configurations such as aerial vehicles with non-symmetric rotation direction or with two different directional rotors [11, 12] have also been presented in the literature. A few other works focused only on the derivation of the dynamics model [13, 14] as well as on efficient configuration of the rotors [15].

2.4.1 Research on Dynamics Modelling

In developing a quad-rotor aerial vehicle, the first step that needs to be addressed is the dynamic modeling of the vehicle system [16]. Recent work involves two different approaches for deriving the system model; the Lagrangian approach [17] and the Newton-Euler formulation [18]. Reference [19] also incorporates blade flapping effects in the dynamic model. Other secondary aerodynamic effects such as airflow disruption have been taken into consideration by the authors in [20].

2.4.2 Research on Control and Stabilization

Among the researches in quad-rotor helicopter the majority of the publications are focused either on control laws or comparison of the performance of control laws. The most important techniques and their respective publications are summarized below:

The first control strategies adopted for quad-rotor stabilization include PID and PD^2 feedback strategies [16, 21, 22]. PID control is the simplest control strategy. In addition, it is relatively easy to implement and does not require specific model parameters. However, PD^2 feedback offers exponential convergence due mainly to the compensation of the Coriolis and Gyroscopic terms. The next most widely used control strategy is based on Lyapunov Theory [17, 23, 24, 25]. According to this technique it is possible to ensure, under certain condition, asymptotical stability for quad-rotor hovering. Other more sophisticated control strategies include Back-stepping Control [26, 27, 28] where convergence of the quad-rotor internal states is guaranteed, but at the expense of computational complexity. Several researchers have demonstrated quad-rotor stabilization using dynamic feedback strategy [29, 30]. This technique basically transforms the closed loop part of the system into a linear, controllable and decoupled subsystem. Authors in [31, 32] implemented adaptive techniques for stabilization where satisfactory performance was obtained despite of parametric uncertainties and un-modeled dynamics. Researchers have also experimented with the Linear Quadratic Regulator (LQR) [16, 33] which involves solving the "Ricatti equation". This approach is computationally expensive.

Other than the mathematical approaches of stabilization, researchers have implemented control based on visual feedback with a camera mounted on-board [34, 35, 36] or placed off-board [37, 38]; however, the off-board camera scenario would appear to be impractical for implementation in the environment considered for this application. In most cases, the on-board camera did not provide sufficient pose information or may have only provided partial state estimation. There are some control algorithms published which demonstrate control with Neural Networks [39] and Fuzzy Techniques

[40].

2.4.3 Research on Platform Design

The platform design of a quad-rotor involves selection of all the active and passive components of the platform, namely the frame (i.e. chassis), motors with controller, propellers, power sources, sensors and processor. In the case of building a quad-rotor structure most researchers either came up with their custom built structures as reported in [15, 20, 41, 42, 43] or may have used available structures like "RCToys" helicopter [14, 44]. The most common material used for building the frame is carbon fiber rod due to its light weight characteristics. In selecting the propeller drive researchers have focused on two different approaches: direct drive of the propeller from motor or through gear train while using light weight low torque high speed motors. However, in both cases brushless DC motors were used. The sensor suite typically included an inertial measurement unit (IMU) either commercially purchased or built by the research team for attitude estimation. Along with this IMU sensor some other sensors have been used to obtain altitude information like SOund NAvigation and Ranging (SONAR), infrared sensor etc. In some cases, special rooms with calibrated cameras to observe the quad-rotor have been used to satisfy this need, as have electromagnetic positioning sensors, infrared, ultrasonic sensors, small GPS units, and onboard cameras [16, 17, 38, 45, 46, 47]. For data processing light-weight, low-power embedded systems were used that are available today such as the single board computer (e.g. Gumstix) or PC-104 platforms [48] etc.

2.4.4 Research on Pose Estimation

The stabilization of a quad-rotor helicopter and a practical approach for autonomy mainly depends on intelligent pose estimation. That is why many researchers have focused their study on different state estimation approach. In this sub-section an overview of major developments made on quad-rotors state estimation is given.

The authors in [49] have stated a very basic strategy for state estimation where four perpendicular infrared distance sensors and an ultrasonic sensor were used. The experiments were conducted in an empty room and the relative position to the room and the aircraft was directly obtained from the sensors. The authors in [15] estimated the pose using motion capture system (two IR-cameras suite) to compute position information. They extracted the yaw orientation and the coordinate information relative to the motion tracker's origin. Authors in [37] used a dual camera system for pose estimation where a pan and tilt ground camera and an on-board camera were used. Their technique involved multi-color blob tracking strategy where the ground camera is used to calculate orientation of the vehicle and the on-board camera is used to calculate position relative to its origin. Researchers at MIT has conducted two consecutive quad-rotor projects named as STARMAC-I and STARMAC-II [20, 45]. They have implemented a position estimation algorithm using a navigation filter that combines horizontal position and velocity information from GPS, vertical position and estimated velocity information from the ultrasonic ranger with acceleration and angular information from the IMU. In both projects a Kalman Filter was used to combine GPS and raw inertial measurements for an accurate full state estimation. At the time of writing this thesis there is currently no other research work related to

pose estimation of small UAV's known to the author.

Chapter 3

Bond Graph Dynamic Modeling and Stabilization of a Quad-Rotor Helicopter

M. Raju Hossain, D. Geoff Rideout, Nicholas Krouglicof
Faculty of Engineering and Applied Science
Memorial University of Newfoundland
St. John's, Newfoundland, Canada

Keywords: Bond graph in aerospace, quad-rotor helicopter dynamics, stabilization of quad-rotor helicopters.

Abstract: *Four-rotor/quad-rotor helicopters are emerging as a popular unmanned aerial vehicle configuration because of their simple construction, easy maintenance and high payload capacity. A quad-rotor is an under-actuated mechanical system with six degrees of freedom and four lift-generating propellers arranged in cross configuration. Maneuvers are executed by varying the speed of the propellers, which causes moments that affect attitude control; and by varying thrust, which affects altitude control. This makes stabilization challenging.*

This work presents a dynamic model of such a vehicle using bond graphs. Both an open loop unstable model and a closed loop stable model using different controllers are demonstrated in this paper. The Newton-Euler formalism with body fixed coordinates is used to model the dynamics of the platform. Rotor drag torque is assumed proportional to thrust of the rotor.

The graphical nature and explicit power flow paths inherent in the bond graph formalism facilitated model construction and troubleshooting. Existing commercial bond graph software allowed simultaneous modeling and control implementation.

The model results for different maneuvers and combinations of propeller thrust agree with existing theoretical results. Open loop simulation shows an uncontrolled revolving effect with increasing linear speed which results in instability of the system. The closed loop PID-controlled result nicely demonstrates the stabilization of the system from an initial roll, pitch, yaw and altitude to the desired steady state configuration.

A version of this paper has been published in the *International Conference of Bond Graph Modeling and Simulation (ICBGM 2010)*. It has also won the "Best Paper Award". The lead author is Mohammed Raju Hossain and the co-authors are Dr. Geoff Rideout and Dr. Nicholas Krouglicof. Mr. Hossain's contribution to this paper is as follows:

- Wrote the paper.
- Developed dynamic model for quad-rotor helicopter.
- Simulated the dynamic model using Bond Graph as a tool.
- Designed Controller for the quad-rotor helicopter.
- Simulated the controlled model.
- Analysed the results.

Dr. Geoff Rideout and Dr. Nicholas Krouglicof provided technical guidance and editing of the manuscript. In this chapter the manuscript is presented with altered figure numbers, table numbers and reference formats in order to match the thesis formatting guidelines set out by Memorial University. The modeling presented in this work is based on bond graph modeling technique. For better understanding of the concept of bond graph modeling; a brief introduction is presented in Appendix B.

3.1 Introduction

Recently, quad-rotors have been considered the best platform for experiments and applications in the field of unmanned aerial vehicles (UAVs) because of their capacity of hovering and slow flight as well as reduced mechanical complexity with relatively higher safety and higher payload. Research is mostly motivated due to their size and autonomous flight, which has practical implications for surveillance, targeting and disaster search in partially collapsed buildings [1]. Mesicopter [2] was an ambitious project which explored ways to fabricate centimetre-sized vehicles. The OS4 project [3] was started in March 2003, with an aim to develop devices for searching and monitoring hostile indoor environments. The X4 Flyer project of Australian National University [4] aims at developing a quad-rotor for indoor and outdoor applications. However, control of a quad rotor helicopter is very complex and virtually impossible without modern computer based control systems due to its under actuated nature with 6 degrees of freedom and only 4 actuating motors. Different researchers have modeled and simulated the system in different ways. This paper introduces bond-graph modeling to the field of UAVs. The complex dynamics of quad-rotor helicopters motivated the use of bond graphs for modeling their dynamics. Other available models are mostly code based differential equations which have less provision for modification and model expansion. This paper mostly emphasizes the theory behind quad-rotor dynamic modeling and maneuver control. The control system of the vehicle is based on classical control methodology. The bond graph that is produced here follows the Newton-Euler formalism which has been widely used for modeling this kind of helicopter [5, 6, 7, 8].

3.2 Quad-rotor Helicopter

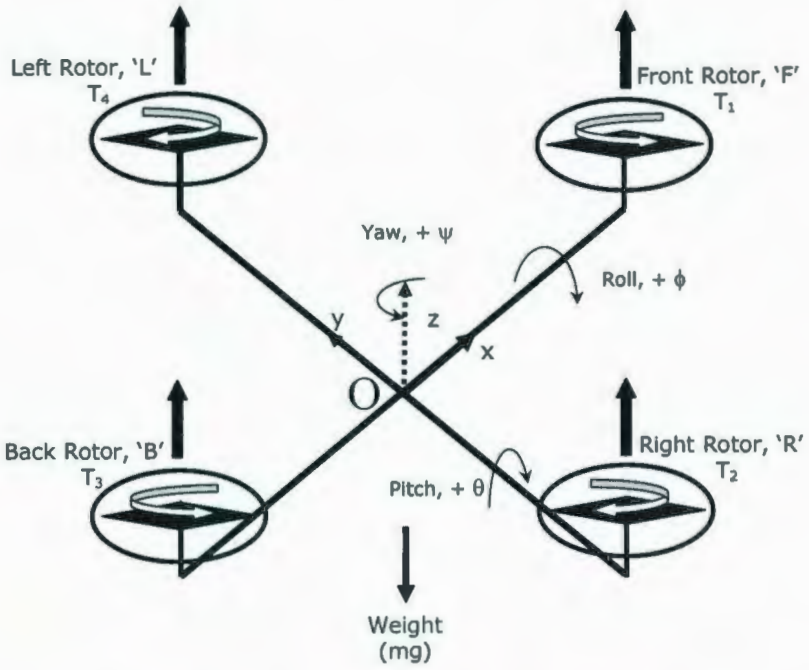

Figure 3.1: Quad-rotor Helicopter Schematic

The quad-rotor helicopter is an aircraft whose lift is generated by four rotors. Control of such a craft is accomplished by varying the speeds of the four rotors relative to each other. Quad-rotors have four fixed propellers in cross configuration (Figure 3.1).

The front and the rear rotors rotate counter-clockwise while the other two rotate clockwise, so that the gyroscopic effects and aerodynamic torque are cancelled in trimmed flight. The rotors generate thrust forces (T) perpendicular to the plane of the rotors and moments (M) about x and y axes; moment about z-axis is obtained using counter torques of the rotor. Increasing or decreasing the speed of the four

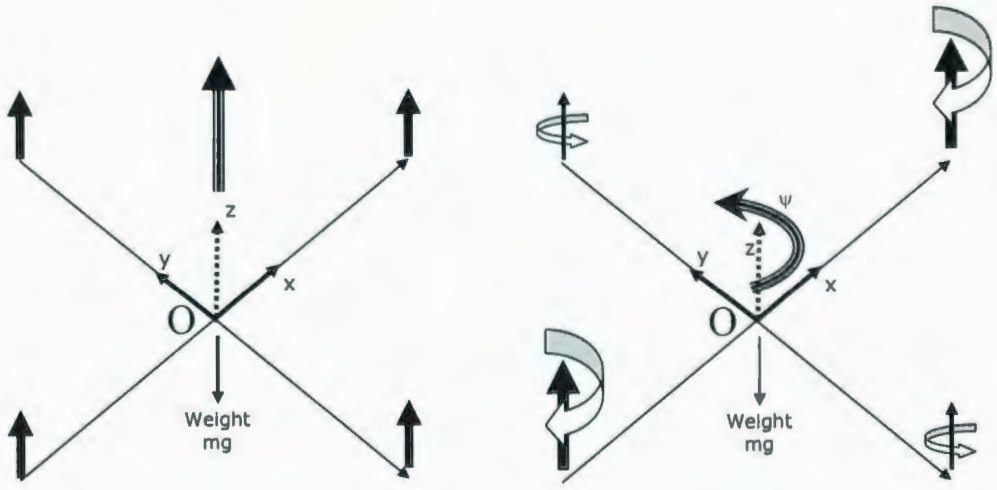

(a) Climb/Descend

(b) Yaw Motion

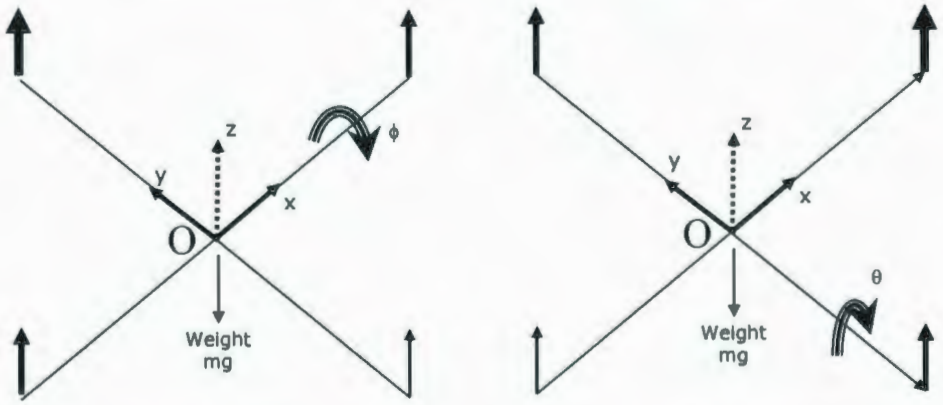

(c) Roll Motion

(d) Pitch Motion

Figure 3.2: Theoretical Maneuvers of a Quad-rotor

propellers simultaneously permits climbing and descending (Figure 3.2a). Vertical rotation (yaw) is achieved by creating an angular speed difference between the two pairs of rotors which in turn creates reactive torques (Figure 3.2b). Rotation about the longitudinal axis (pitch) and lateral axis (roll), and consequently horizontal motions, are achieved by tilting the vehicle. This is possible by changing the relative propeller speed of one pair of rotors (Figure 3.2c, 3.2d)

3.3 Development of System Model

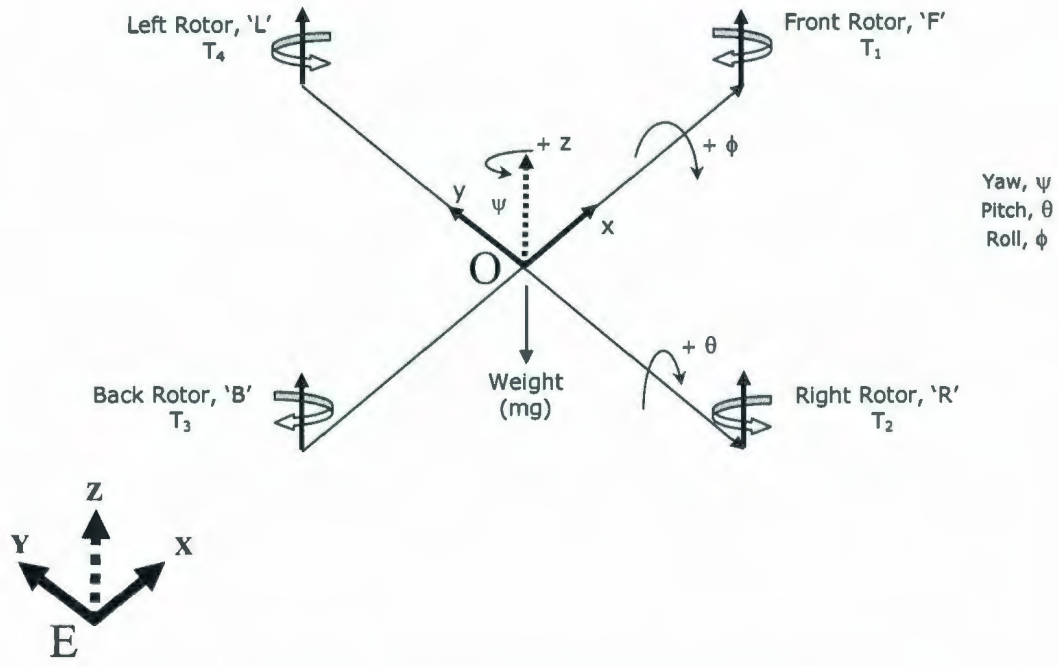

Figure 3.3: Co-ordinate System for Modeling

The derivation of the system equations is now shown along with the evolution of the bond graph for the quad-rotor vehicle. To derive the equations we assume the airframe is rigid, all the propellers are in the same horizontal plane and the quad-rotor structure is symmetric. Figure 3.3 shows the coordinate system of a quad-rotor helicopter where body fixed frame $O = x, y, z$ is assumed to be at the centre of gravity and aligned with the principal axes of the body. The z-axis is considered to be positive upward. Due to the double symmetry of the quad-rotor, it is logical to set the origin O at the intersection of the axes of the vehicle. Choosing the directions of

the axes according to the common conventions in the literature results a set of axes which is shown in figure 3.3. The body fixed frame $O = x, y, z$ is considered to be moving with respect to earth frame/inertial frame $E = X, Y, Z$.

The equation of motion of such a rigid body, under external forces ($F_{external}$ and $M_{external}$) applied at the center of mass and expressed in the body frame, are developed in the Newton-Euler formalism [9, 10]. With respect to these body fixed coordinates, the rotational inertia properties remain invariant and the products of inertia are all zero.

$$\left.\begin{aligned} F_{x,external} &= m\dot{v}_x - mv_y\omega_z + mv_z\omega_y \\ F_{y,external} &= m\dot{v}_y - mv_z\omega_x + mv_x\omega_z \\ F_{z,external} &= m\dot{v}_z - mv_x\omega_y + mv_y\omega_x \\ M_{x,external} &= I_{xx}\dot{\omega}_x - (I_{yy} - I_{zz})\omega_y\omega_z \\ M_{y,external} &= I_{yy}\dot{\omega}_y - (I_{zz} - I_{xx})\omega_z\omega_x \\ M_{z,external} &= I_{zz}\dot{\omega}_z - (I_{xx} - I_{yy})\omega_x\omega_y \end{aligned}\right\} \tag{3.1}$$

The bond graph representation [11] of this Newton-Euler equation is shown in Figure 3.4 where the upper triangle relates the energy flow in translational dynamics and the lower triangle defines rotational dynamics. The three 1-junctions both in the upper and lower triangle provide the nodes for external forces and moments respectively.

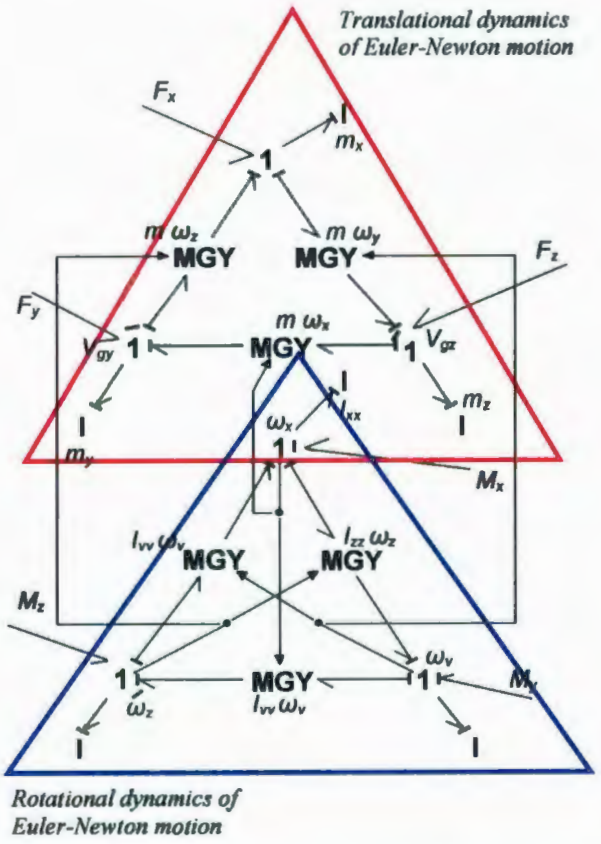

Figure 3.4: Bond Graph Representation of Euler Equation

3.3.1 Modeling of Translational Dynamics

The translational dynamics of such a helicopter can be rewritten from Equation 3.1 as,

$$\begin{bmatrix} m & 0 & 0 \\ 0 & m & 0 \\ 0 & 0 & m \end{bmatrix} \begin{bmatrix} \dot{v}_x \\ \dot{v}_y \\ \dot{v}_z \end{bmatrix} = \begin{bmatrix} F_x \\ F_y \\ F_z \end{bmatrix} - \begin{bmatrix} 0 & v_z & -v_y \\ -v_z & 0 & v_x \\ v_y & -v_x & 0 \end{bmatrix} \begin{bmatrix} \omega_x \\ \omega_y \\ \omega_z \end{bmatrix} \tag{3.2}$$

The external force contribution on the quad-rotor body is mainly the rotor thrust and the drag torque. The drag force is defined as [12] $F_{drag} = \frac{1}{2} C_d \rho A v^2$, where C_d is

the coefficient of drag, ρ is the density of medium (air), A is the frontal area of the body and v is the velocity. Considering all the constants involved in this equation we rewrite $F_{drag} = C_D v^2$ where C_D is the combination of the constant terms and is defined as 'Drag Constant' in this paper. Therefore,

$$\begin{bmatrix} F_x \\ F_y \\ F_z \end{bmatrix} = \begin{bmatrix} -C_{D_x}\dot{x}^2 \\ -C_{D_y}\dot{y}^2 \\ \sum_{i=1}^{4} T_i - C_{D_z}\dot{z}^2 - R \cdot mg \end{bmatrix} \tag{3.3}$$

Here, C_D has components in all three directions and T_i is the thrust mainly generated by the four rotors which are spinning with a velocity of ω and is given by [12].

$$T = bL = \frac{\rho}{4}\,\omega^2\,R^3\,a\,b\,c\,(\theta_t - \varphi_t)$$

where R is the radius of rotor, a is the constant blade lift curve slope, b is the number of blades, c is the blade chord, θ_t and φ_t are pitch at blade tip and inflow angle at the tip respectively. Combining all the constants as C_T we get

$$T_i = C_T \omega^2$$

$R = SO(3)$ is the rotation matrix representing ZYX Euler angles of roll(ϕ), pitch(θ) and yaw(ψ).

$$R = \begin{bmatrix} \cos\psi\cos\theta & \cos\psi\sin\theta\sin\phi - \sin\psi\cos\phi & \cos\psi\sin\theta\cos\phi - \sin\psi\sin\phi \\ \sin\psi\cos\theta & \sin\psi\sin\theta\sin\phi - \cos\psi\cos\phi & \sin\psi\sin\theta\cos\phi - \cos\psi\sin\phi \\ -\sin\theta & \cos\theta\sin\phi & \cos\theta\cos\phi \end{bmatrix} \quad (3.4)$$

Due to the discontinuity of the time variation of angles ϕ, θ, and ψ the body angular rates ω_x, ω_y, ω_z need to be transformed by Euler angles using the matrix below [13],

$$\begin{bmatrix} \omega_x \\ \omega_y \\ \omega_z \end{bmatrix} = \begin{bmatrix} 1 & 0 & -\sin\theta \\ 0 & \cos\phi & \sin\phi\cos\theta \\ 0 & -\sin\phi & \cos\phi\cos\theta \end{bmatrix} \begin{bmatrix} \dot{\phi} \\ \dot{\theta} \\ \dot{\psi} \end{bmatrix} \quad (3.5)$$

These transformation angles though suffer from singularity at $\theta = \pm\frac{\pi}{2}$ known as 'Gimbal Lock' but this does not affect UAVs in regular flight maneuvers. In the bond graph the translational efforts arise from one gravitational effort source and four rotor effort sources, where gravitational effort is transformed from earth reference to body reference using Euler rotation angles. The upper red triangular bounding box of figure 3.5 illustrates the translational dynamics of the quad-rotor. As the quad-rotor moves at low speed we can consider the drag constant C_D as negligible and for the simulation, rotor thrust is considered as a source of effort.

3.3.2 Modeling of Rotational Dynamics

Rotational dynamics of a quad-rotor consist of three angular motions, namely roll, pitch and yaw. Roll and pitch rotation are produced due to moments generated by the thrust difference of the rotors at y-axis and x-axis respectively, which are basically acting at a certain perpendicular distance from the center of gravity. However, yaw is produced due to reactive torque in the rotor. From Equation 3.1 we can redefine that,

$$\begin{bmatrix} I_{xx} & 0 & 0 \\ 0 & I_{yy} & 0 \\ 0 & 0 & I_{zz} \end{bmatrix} \begin{bmatrix} \dot{\omega}_x \\ \dot{\omega}_y \\ \dot{\omega}_z \end{bmatrix} = \begin{bmatrix} M_x \\ M_y \\ M_z \end{bmatrix} - \begin{bmatrix} 0 & \omega_z & -\omega_y \\ -\omega_z & 0 & \omega_x \\ -\omega_y & \omega_x & 0 \end{bmatrix} \begin{bmatrix} I_{xx}\omega_x \\ I_{yy}\omega_y \\ I_{zz}\omega_z \end{bmatrix} \tag{3.6}$$

where,

$$\begin{bmatrix} M_x \\ M_y \\ M_z \end{bmatrix} = C_T \begin{bmatrix} 0 & -l & 0 & l \\ -l & 0 & l & 0 \\ -\lambda & \lambda & \lambda & -\lambda \end{bmatrix} \begin{bmatrix} \omega_1^2 \\ \omega_2^2 \\ \omega_3^2 \\ \omega_4^2 \end{bmatrix} = \begin{bmatrix} 0 & -l & 0 & l \\ -l & 0 & l & 0 \\ -\lambda & \lambda & \lambda & -\lambda \end{bmatrix} \begin{bmatrix} T_1 \\ T_2 \\ T_3 \\ T_4 \end{bmatrix} \tag{3.7}$$

In the above equation, l is the distance between centre of gravity and the centre of the rotors and λ $[NmS^2]$ is the proportionality constant between thrust T_i and motor torque τ_i. In this case for the simplicity of simulation we consider λ as 1 (assuming quasi steady state). However, in practice motor reactive torque is a function of

velocity according to [12]

$$\tau_i = C_R \omega_i^2 + I_r \dot{\omega}_i$$

where C_R is the reactive torque constant due to drag terms and I_r is the rotational inertia of the rotor.

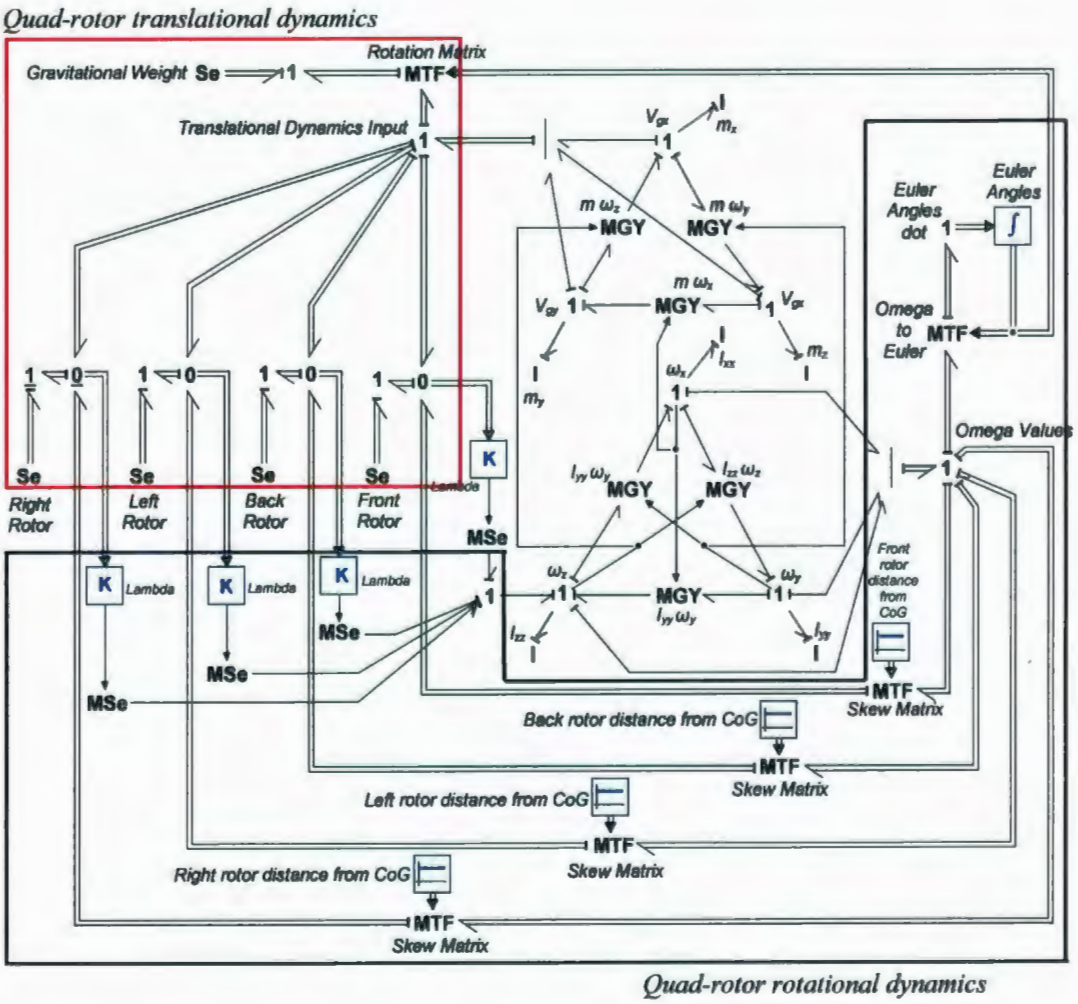

Figure 3.5: Open Loop Model of Quad-rotor Helicopter

In Figure 3.5 contributions of the rotor efforts are given to the three angular velocity ports using a skew symmetric matrix containing distances between the rotors and the center of gravity, which creates moments along their respective axis. However the yaw occurs due to the reactive torque of the rotors which for simplicity of calculation is considered as proportional to thrust difference and is provided straight from the rotor to the z-axis rotation port. This gives a complete open loop model for the quad-rotor vehicle. Obviously, only the dominant effects are modeled neglecting aerodynamic forces and moments exerted by drag and the dynamics of motor and propeller which can be extended easily by adding more external forces to their respective directional ports. The double lines used in Figure 3.5 are vector bonds proposed in [14].

3.4 Control Modeling

Stabilization is very important for an under-actuated system like a quad-rotor, as it is inherently unstable due to its six degrees of freedom and four actuators. A control system is modeled for the quad-rotor using four PID (Proportional-Integral-Derivative) controllers, where the input parameters are attitude and altitude (i.e, roll, pitch, yaw and height) and the controlling devices are the actuators or the rotors of the quad-rotor. By controlling the thrust from the rotor one can have a stabilized system as well as a desired attitude and altitude due to the nature of the quad-rotor maneuver control.

Table 3.1 shows the combinations of rotor excitations for any kind of positive maneuvers. For example, if we want to increase the pitch (CCW of θ) we have to

Table 3.1: Combinations of Actuation for Controlling Altitude and Attitude

	Front Rotor, F	Back Rotor, B	Right rotor, R	Left rotor, L
Lift	+	+	+	+
Roll			+	-
Pitch	+	-		
Yaw	+	+	-	-

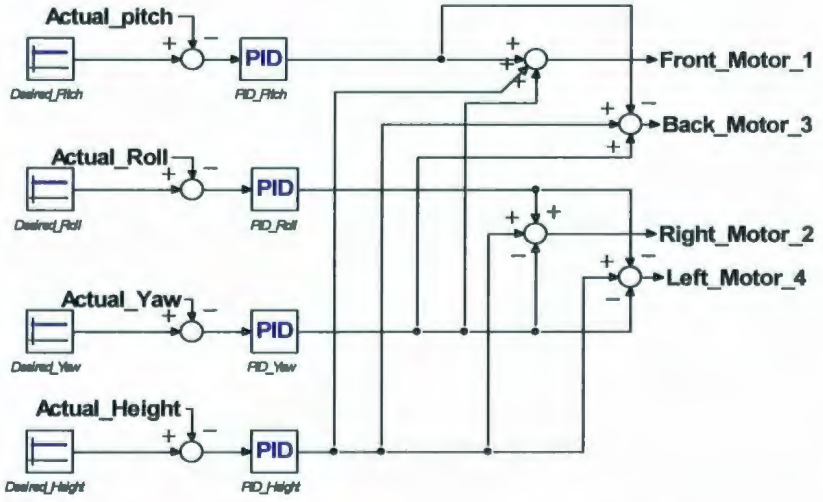

Figure 3.6: Block Diagram of Quad-rotor Craft Controller

increase thrust at the back rotor as well as decrease thrust in the front rotor. The bond graph in Figure 3.6 shows the combination of the four PID controllers that stabilizes the quad-rotor. The controller measures the error between the desired and actual attitude and actuates the rotors accordingly. Figure 3.7 shows the complete closed loop model utilizing this controller into the open loop system. However, as the attitude governs the position and velocity vector of the system, this controller can be further extended to move to any desired coordinate by adding position controller into the closed loop model. P, PI and PID controllers were tested. The PID controller stabilizes the system faster and more accurately than the other two.

3.5 Simulation Results

Initially the performance of the model were explored performing open loop simulations. The simulations were performed using '20-SIM' software, which converted the bond graph into a simulation model and performed numerical integration using a Backward Differentiation method with tolerance of 1×10^{-5}. The simulation demonstrates the flight maneuver which satisfies the theoretical trajectories that the quad-rotor is supposed to perform at certain combinations of the rotor thrust.

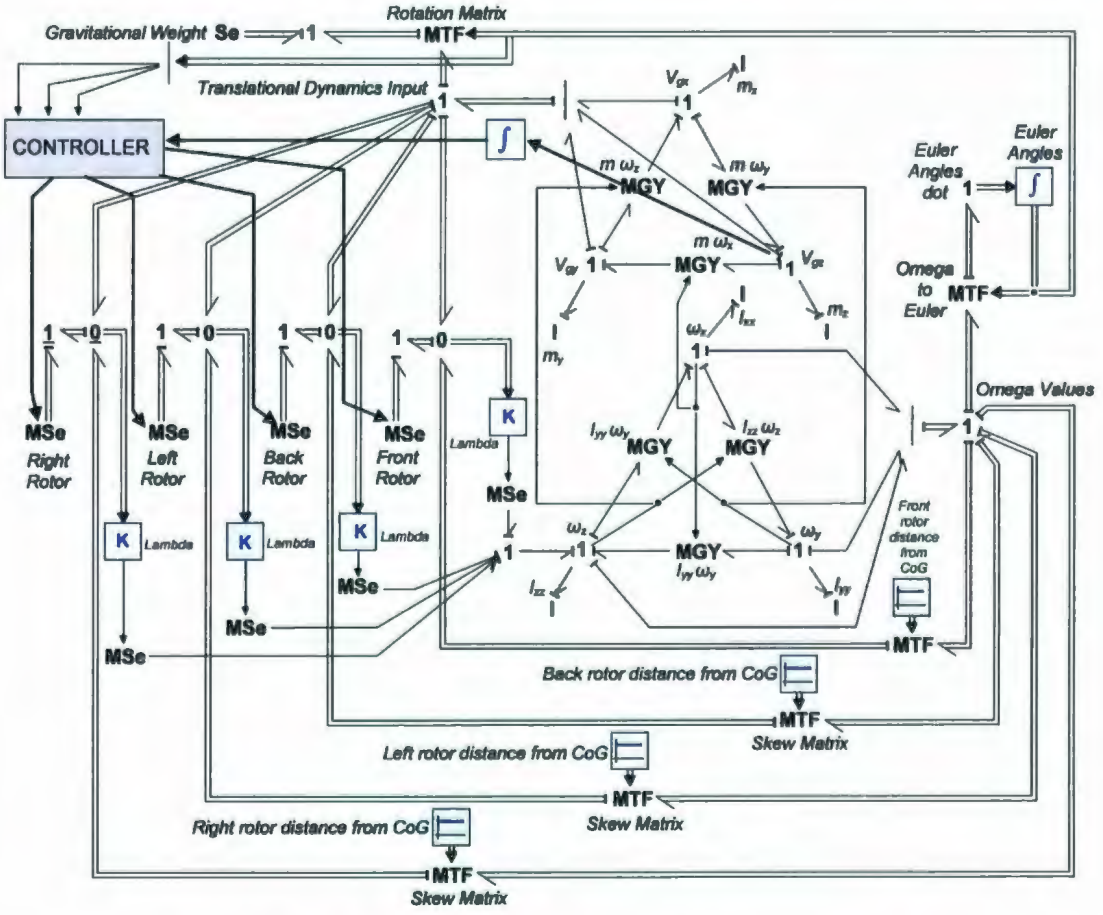

Figure 3.7: Closed Loop Bond Graph of Quad-rotor Craft

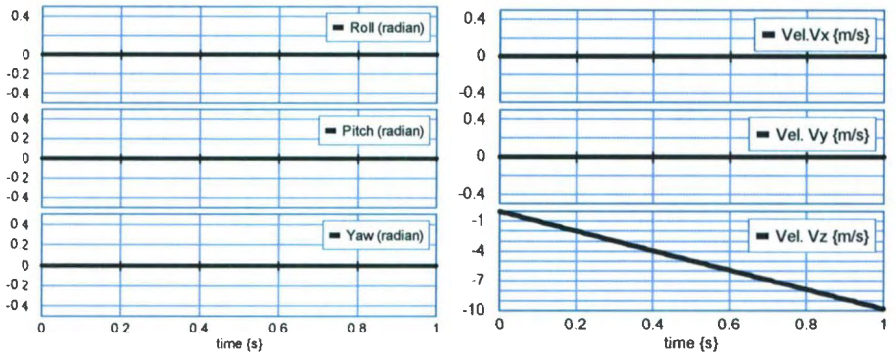

(a) Rotation Angles (b) Linear Velocities

Figure 3.8: Open Loop Free Fall Simulation for Zero Thrust

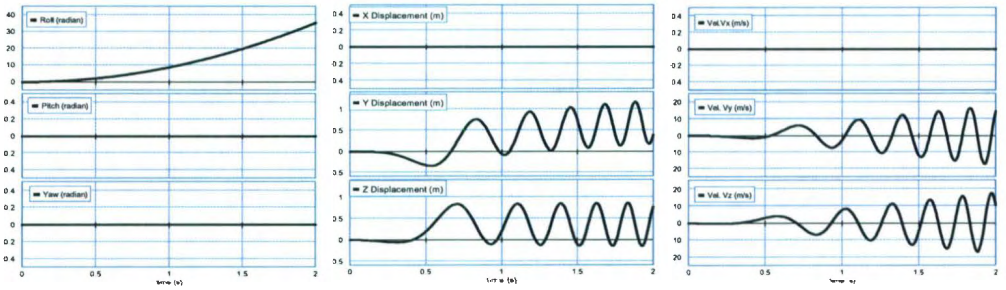

(a) Angular Motion (b) Linear Motion (c) Linear Velocities

Figure 3.9: Open Loop Roll Motion due to $(T_1, T_2, T_3, T_4) = (1.5, 1.5, 1.5, 0.5)N$

Figure 3.8 shows the free-fall test. Providing no thrust to the quad-rotor causes it to fall down due to gravity at a rate of 9.8 ms^{-1}. The parameters considered for simulation are realistic quad-rotor parameters from [15] where the mass of the vehicle $m = 0.5\ kg$. For lifting the helicopter it is obvious that there should be minimum combination vertical thrust of 4.9 N provided by all the four rotors. Figure 3.9 demonstrates the roll motion when subjected to an equal thrust at front and back rotor and unequal thrust at right and left rotor. In this case, front and back rotor

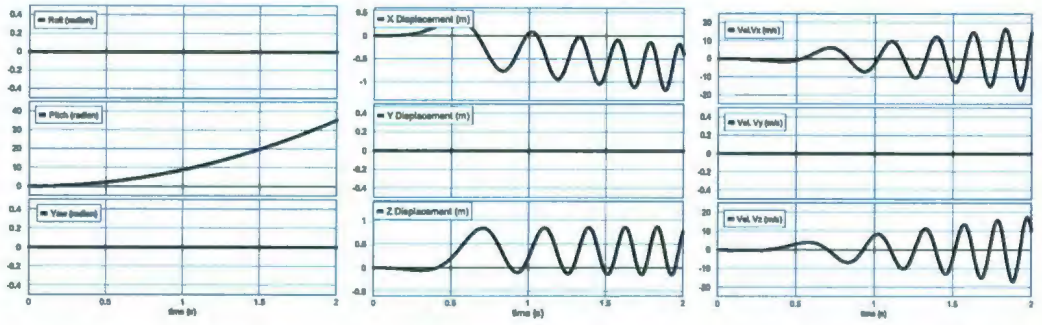

(a) Angular Motion (b) Linear Motion (c) Linear Velocities

Figure 3.10: Open Loop Pitch Motion due to $(T_1, T_2, T_3, T_4) = (0.5, 1.5, 1.5, 1.5)N$

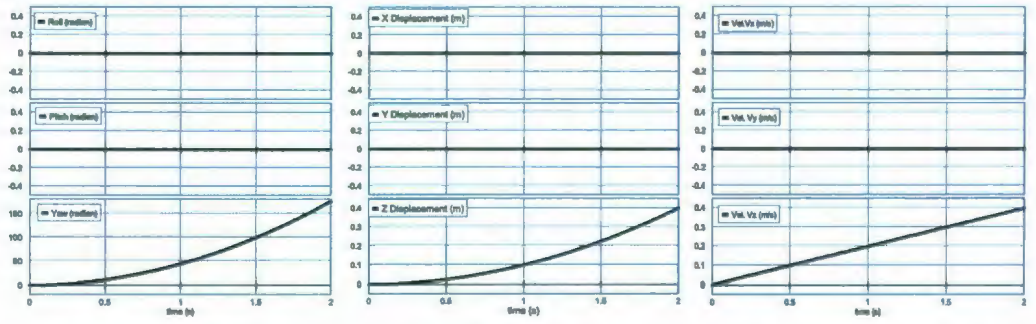

(a) Angular Motion (b) Linear Motion (c) Linear Velocities

Figure 3.11: Open loop Yaw Motion due to $(T_1, T_2, T_3, T_4) = (1.0, 1.5, 1.0, 1.5)N$

was given a thrust of 1.5 N while right and left rotors were given thrusts of 1.5 N and 0.5 N respectively. Figure 3.9(a,b) shows a revolving nature of the body around its x-axis with no movement in the direction of the x-axis except the angular roll motion. However, the revolving effect is increasing due to inertia of the body according to Newtons law of rotation which can be seen in Figure 3.9(c). Pitch motion is very similar to roll motion due to the body symmetry as well as the mechanism of the pitch and roll motion. Figure 3.10 shows effects very similar to roll, but the actuating controls have been interchanged to create pitch motion.

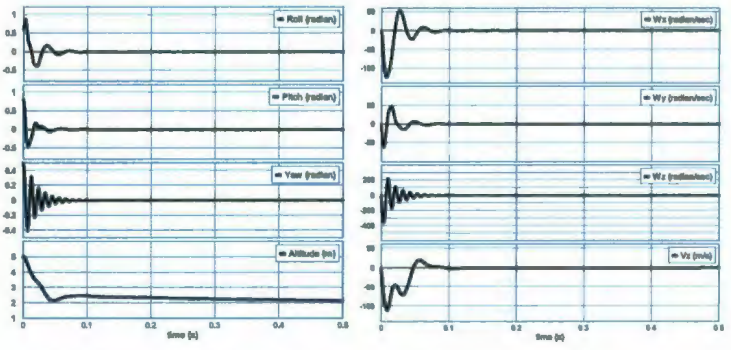

(a) Controlled Angles (b) Angular Velocities

Figure 3.12: Simulated Closed Loop Response of Quad-rotor

The yaw motion was achieved by providing front and back rotor thrusts of 1.0 N and 1.5 N to the right and left rotors. As the right and left rotors rotate clockwise with higher magnitude of thrust compared to the front and back rotor, the reactive torque is dominated by the right and left rotors rotational direction. Thus the motion of the body is in the counter-clockwise direction which creates the positive yaw as seen in Figure 3.11. However in this case there is no other linear motion in any other direction but z, which means the helicopter is moving upward with yaw motion. The craft moves up as the total thrust of rotors has overcome the gravitational weight.

All the responses show that the system is highly unstable and coupled. The closed loop controlled model stabilizes the craft as expected. The response of the controller is shown in Figure 3.12. As the linear motion along x and y is dominated by pitch and roll respectively (in the absence of external disturbance i.e, wind), stabilization of angular motions stabilizes the linear motion along x and y direction. The only remaining required control is for altitude. Thus control of roll, pitch, yaw and height creates a complete stabilization the system. Figure 3.12a shows how the body is stabilized from an intermediate condition of (roll, pitch, yaw, height = 0.6 rad, 0.8

rad, 0.5 *rad*, 5 *m*) to a stabilized condition of no angular motion, no lateral and longitudinal motion, and a desired height of 2 *m*. The closed loop system can also create a desired orientation of the body from a stable position which can be further used for controlling the position vector of the helicopter.

3.6 Summary & Conclusion

This paper presents the application of bond graph modeling to quad-rotor unmanned aerial vehicles (UAV). A primary contribution of this paper is to demonstrate that bond graphs facilitate modeling of the complex and coupled dynamics of the system, as well as extension or simplification of the system model or its controller. As the quad-rotor is a mechatronic system, involvement of different energy domains is a must. That is why selection of the modeling language is a significant decision if a future extension is expected. The bond graph model presented herein is anticipated to be of value and interest to the UAV design community. Future model extensions include higher-fidelity rotor dynamics and actuator modeling. Possible extensions to the controller might involve control of its position or co-ordinates in space that may lead the model to be even more accurate and practical.

References

[1] D. Greer, P. M. Kerrow, and J. Abrantes, "Robots in urben search and rescue operations," in *proceedings Australian Conference on Robotics and Automation*, Aukland, New Zealand, November 2002, pp. 25 – 30.

[2] I. Kroo and F. Prinz, "The mesicopter: A meso-scale flight vehicle," Stanford University, Stanford, USA, Tech. Rep., May 1999.

[3] P. Pounds, R. Mahony, and P. Corke, "Modeling and control of quad-rotor robot," in *Proceedings of the Australasian Conference on Robotics and Automation*, Auckland, New Zealand, December 2006.

[4] S. Bouabdallah, P. Murrieri, and R. Siegwart, "Towards autonomous indoor micro VTOL," *Autonomous Robots*, vol. 18, pp. 171 – 183, 2005.

[5] A. Tayebi and S. McGilvray, "Attitude stabilization of a four-rotor aerial robot," in *Proc. of the 43rd IEEE Conference on Decision and Control*, Atlantis, Paradise Island, Bahamas, December 2004, pp. 1216 – 1221.

[6] S. Bouabdallah, A. Noth, and R. Siegwart, "Course lecture of dynamic modeling of UAVs," Autonomous Systems Laboratory, Ecole Polytechnique, France, May 2006.

[7] S. Park, D. Won, M. Kang, T. Kim, and H. Lee, "RIC (robust internal-loop compensator) based flight control of a quad rotor type UAV," in *Proc. of the Intelligent Robots and Systems*, August 2005, p. 3542 3547.

[8] A. Ahmad and D. Wang, "Dynamic modeling and nonlinear control strategy for an underactuated quad rotor rotorcraft," *Journal of Zhejiang University (Science A)*, vol. 9 (4), p. 539 545, 2008.

[9] R. Murray, S. Sastry, and L. Zexiang, *A Mathematical Introduction to Robotic Manipulation.* CRC Press, Inc. ISBN: 0849379814, 1994.

[10] J. Ginsberg, *Advanced Engineering Mechanics - 2nd Edition.* Cambridge University Press, 1995.

[11] D. Karnopp, L. Margolis, and R. Rosenberg, *System Dynamics: Modeling and Simulation of Mechatronic Systems - 4th Edition.* A Wiley-Interscience Publication. ISBN: 9780471709657, 2005.

[12] R. Prouty, *Helicopter Performance, Stability and Control.* Kreiger Publishing Company, June 1995.

[13] R. F. Stengel, *Flight dynamics.* Princeton University Press, 2004.

[14] P. C. Breedveld, "Proposition of unambiguous vector bond graph notation," *Journal of Dynamics System, Measurement and Control*, vol. 104, no. 3, pp. 267 – 270.

[15] S. Bouabdallaha, A. Noth, and R. Siegwart, "PID vs LQ control techniques

applied to an indoor micro quadrotor," in *Proc. of the Intelligent Robots and Systems (IROS)*, vol. 3, October 2004, pp. 2451– 2456.

APPENDIX

Table 3.2: Bond Graph Parameters

Model Parameters	Value	Unit
Thrust Co-efficient, C_T	1	Ns^2
Drag Co-efficient, C_D	1	Nms^2
CoG to rotor distance, l	0.2	m
Inertial moment on x and y, I_{xx}=I_{yy}	0.0226	kgm^2
Inertial moment on z, I_{zz}	0.0227	kgm^2
quad-rotor mass, m	0.5	kg
PID Controller Parameters	Value	
Gain constants for roll and pitch		
K_p	0.9	
K_i	0.3	
K_d	0.2	
Gain constants for yaw and height		
K_p	0.06	
K_i	0.30	
K_d	0.02	

Chapter 4

Propeller Dynamometer for Small Unmanned Aerial Vehicle

M. Raju Hossain, Nicholas Krouglicof
Faculty of Engineering and Applied Science
Memorial University of Newfoundland
St. John's, Newfoundland, Canada

Abstract: *This paper details the design and development of a small scale air propeller dynamometer based on thin beam strain gauge load cells. The dynamometer will be used to characterize the performance of small propellers for Unmanned Aerial Vehicles (UAVs) in order to obtain an accurate system model and design an appropriate controller for hovering and smooth flight. A brief description of the design concept and calibration procedure along with test results is presented here. A static calibration was performed to determine thrust/torque measurement sensitivity as well as cross-sensitivity. Measurement data was captured and processed using a Sigma-Delta data acquisition board. Test results confirm that the dynamometer can be used to reliably measure thrust and torque produced by UAV propellers up to 10 inch in diameter with an accuracy of $\pm 1\%$ of full scale.*

A version of this paper has been published in the "*IEEE Canadian Conference on Electical and Computer Engineering (CCECE 2010)*". The lead author is Mohammed Raju Hossain and the co-author is Dr. Nicholas Krouglicof. Mr. Hossain's contribution to this paper is as follows:

- Wrote the paper.
- Designed and developed the Propeller Dynamometer which was started as a graduate course project and was extended later. The title of the graduate course was "Mechatronics Design".
- Calibrated and verified the setup.
- Performed test and gather data for different propellers.
- Analysed the results.
- Performed all literature searches required for background information.

Dr. Nicholas Krouglicof provided continuous technical guidance and editing of the manuscript. In this chapter the manuscript is presented with altered figure numbers, table numbers and reference formats in order to match the thesis formatting guidelines set out by Memorial University.

4.1 Introduction

The application of Unmanned Aerial Vehicle (UAV) is increasing dramatically as design and control technologies for small flying objects merge with today's advanced sensors and embedded systems. This synthesis has made the control of UAV's more accurate and reliable. One of the critical steps in the development of a UAV is the characterization of the propeller that is to be used in the vehicle. This defines the maximum payload the vehicle can accommodate as well as the torque/thrust response as a function of rotational speed. The propeller performance information is critical to accurately model the vehicle for various flight maneuver and to design an appropriate controller. The dynamometer presented in this paper was developed to identify and characterize the optimum propeller for a quadrotor helicopter UAV [1] and to design a suitable, robust controller. This narrowed down the size of the propeller to a maximum of 10 inches.

Researchers have developed different types of propeller dynamometers depending on the propeller size and characteristics. The Stewart platform based dynamometer instrumented with strain gauges [2] has a fairly good decoupled thrust/torque response; but is complex in structure and not suitable for very small loads. A marine propeller dynamometer developed at the University of British Columbia (UBC) [3] using load cells is fairly simple in design and effective in operation but is limited to large load measurements. In applications beyond propeller characterization, dynamometers have been developed using strain gauge and piezo-electric accelerometers to measure the cutting force in milling machines [4]. This design is not suitable for use with propellers. The only dynamometer that was designed to specifically measure the

performance of small UAV propellers is described in [5] and [6]; however these were designed for characterizing propellers above 10 inches in diameter. The design that is proposed in this paper characterizes propellers ranging from 3 inches to 10 inches in diameter and is geared towards analyzing and finding the optimum propeller for a quadrotor helicopter [1] which requires propellers with an excellent thrust to weight ratio.

4.2 Hardware Design

The dynamometer shown in Figure 4.1(b) is approximately 80 *mm* in diameter, 90 *mm* in length and is comprised of three major components:

- A brushless DC outrunner motor (MSYS-LRK 195.03) is used to drive the propellers.
- Six full bridge thin beam load cells with a full scale accuracy of 0.25% are employed to measure the response; three (model LCL 227G) to measure thrust and three (model LCL 113G) to measure torque.
- An optical tachometer was used to measure speed (RPM).

These components with the exception of the tachometer are housed within an ABS housing which is assembled from three main parts (Figure 4.1c). The top most part (part 1) holds the propeller with motor and is coupled to the next part (part 2) through ball bearing leaving a vertical gap between these two parts. Three load cells are placed in this vertical gap to measure torque; i.e., the deflection that results when rotation occurs in the top part. The remaining three load cells are placed between

the middle part (part-2) and base part (part-3) to measure the thrust response. All of the ABS parts were manufactured on a rapid prototyping machine using Fused Deposition Modeling (FDM).

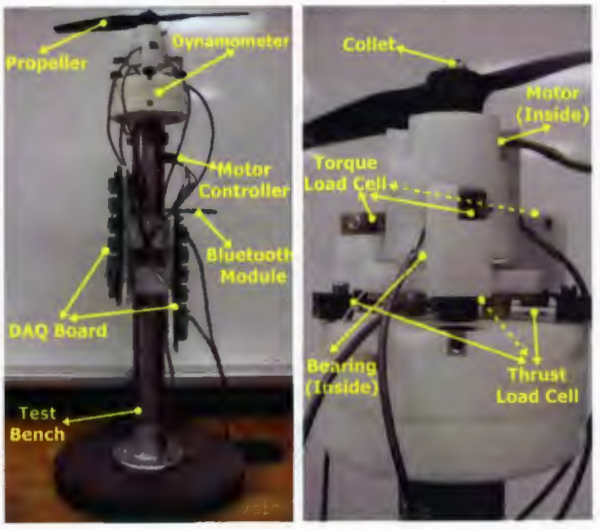

(a) Test-rig (b) Dynamometer

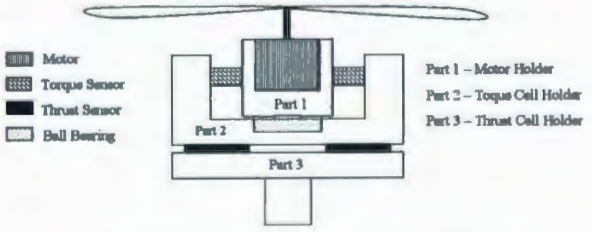

(c) Schematic Diagram of Dynamometer

Figure 4.1: Air Propeller Test Bench

4.2.1 Mechanism

While the propeller rotates it creates thrust and torque at the same time. As a consequence it pushes against the airflow and pulls away from the dynamometer assembly. The top part and middle part responds to this vertical lift as a single

entity (both these parts are secured to the ball bearing with an interference fit). This creates bending in the lower three load cells resulting in a thrust response.

On the other hand when top part produces torque due to the rotation of the propeller, it creates bending in the top three load cells resulting in a torque response; No response in torque load cells was observed due to thrust load and vice versa; i.e, the two sets of load cells were completely decoupled. The tachometer was directed towards light reflecting tape installed below the propeller in order to record the RPM response.

4.2.2 Instrumentation

The brushless out-runner motors were controlled by a MOS-FET Speed Controller (Model BL-6) capable of delivering 4 *amps* of continuous current. A Pulse width modulated (PWM) command signal to the speed controller was generated by a microcontroller board that communicated with a Windows PC via a Universal Serial Bus (USB) interface. The load cells output signals were conditioned and captured by a custom data acquisition board based on a high resolution Sigma-Delta Analog-to-Digital (A/D) converter. For improved electrical isolation, the data acquisition board communicated with the Windows PC using Bluetooth technology.

As mentioned earlier, the dynamometer described in this work was designed to find the best propeller for developing a quadrotor helicopter as described in reference [1]. To achieve the maximum payload of the quadrotor helicopter it is important to minimize the weight of the motors as well as other components that constitute the quadrotor platform. This narrowed down the selection of motor and speed controller

(12 gm for the MSYS-LRK 195.03 motor and 6 *gm* for the speed controller).For these reasons the dynamometer was designed to accommodate this specific motor. However, by modifying the top part (part 1) other motors can be tested.

4.2.3 Data acquisition

The strain gauge data acquisition board is based on a 24 bit Sigma Delta A/D with integrated signal conditioning and bridge reference voltage. A microcontroller (PIC 18F4550) on the data acquisition board was interfaced to the A/D and handled the wireless communications with the Windows PC via a bluetooth modem. The board was programmed to read the six different strain gauge sensors using commercially available microcontroller development software (MPLAB). A digital median (rank) filter was implemented to augment the resolution of the load cell signals by incorporating the median code in the program. The individual load cells and data acquisition system were calibrated using known weights.

4.3 Calibration

The torque and thrust load cells were statically (i.e., non rotating condition) calibrated using known weights. An arrangement of supports and pulleys allowed thrust to be applied in positive direction by suspending known weights. A known torque was applied in a similar manner as a couple based on a lever arm of ± 20 *mm*. A mathematical relationship between weight and A/D count was found using this calibration setup. This was later used to find the thrust and torque produced by propellers.

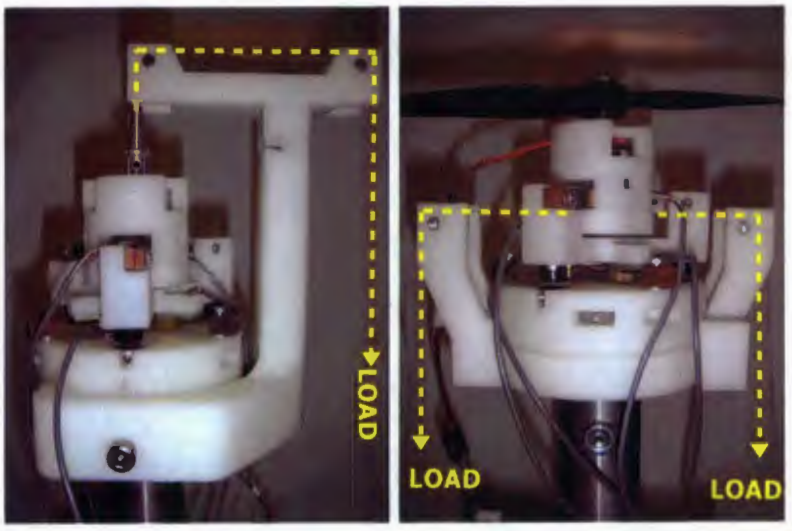

(a) Thrust Calibration (b) Torque Calibration

Figure 4.2: Calibration Apparatus

4.3.1 Thrust Calibration

The thrust calibration apparatus is shown in Figure 4.2(a). Two pulleys were arranged to produce positive thrust on the motor shaft. Weights were used to calibrate the three thrust thin beam load cells which are sensitive to very small loads. Due to the limited full-scale capacity of the load cells, the calibration was performed up to 250 gm. This is consistent with the expected thrust load from the propellers which is less than 300 gm. During thrust calibration it was necessary to impart some vibration to the rig prior to recording the zero reading or reading at low thrust levels. This was done to overcome the friction in the two pulleys. This phenomena was not observed during the torque calibration because only a single pulley was used. The inherent friction of the pulleys used in this work is assumed to be equal.

A third order polynomial was found to accurately represent the thrust readings

(Figure 4.3). The accuracy of this equation was validated by imparting random loads on the calibration bench and comparing with the measured load. This confirmed the accuracy of the equation as 0.9% of full scale. The calibration curve is shown in Figure 4.3. The thrust sensor hysteresis was found to be negligible by performing the calibration with both increasing and decreasing applied loads.

4.3.2 Torque Calibration

The torque calibration frame is shown in Figure 4.2(b). The maximum weight suspended from each of the two load platforms was 94 gm which resulted in the maximum calibration input load of 188 gm for a lever arm of 20 mm. Calibration was performed with both increasing and decreasing applied torques, with no discernible difference in the results which demonstrates that torque sensor hysteresis is negligible. The torque calibration curve in Figure 4.3 shows that a best fit was obtained for a third order polynomial equation in much the same way as the thrust calibration curve. This was later subsequently validated with random loads resulting in an accuracy of $\pm 0.6\%$ of full scale.

4.3.3 Interactions

To ensure the interaction of 'thrust on torque' and 'torque on thrust' both the torque and thrust readings were monitored simultaneously during the calibration procedures mentioned above. Changes in the reading for one variable due to application of the other were always negligible and within the measurement accuracy. The interaction plots are shown in Figure 4.4(a) and (b). There were no interaction observed in the

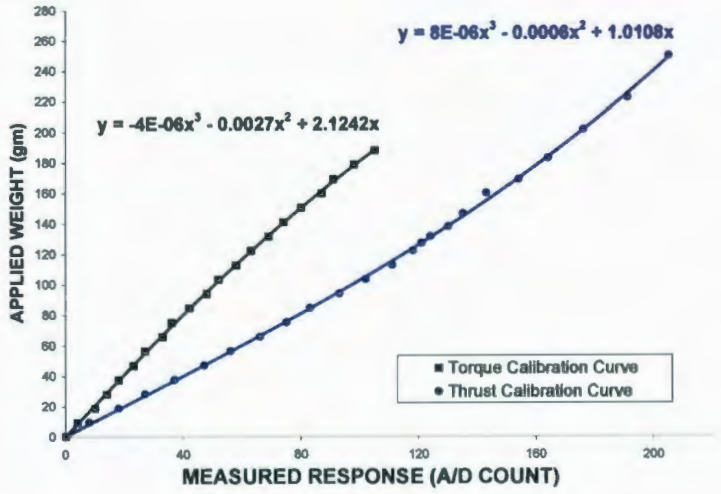

Figure 4.3: Calibration Curves

thrust cells when torque was applied to the rig (Figure 4.4(a)); however, a small torque was observed in the torque load cells during thrust calibration. This was due to a "twist" tendency in the torque cells at higher thrust loading. It was therefore concluded that interactions were minimal and effectively negligible.

4.3.4 Accuracy and Repeatability

The results of the calibration and interactions indicate the accuracy of the thrust and torque readings are within $\pm 1\%$ of full scale. In addition to the accuracy calibration, repeatability was also tested and found to be consistent.

4.4 Propeller Testing

During the characterization of propellers the dynamometer was mounted on top of a 25 *inch* hollow shaft to create distance between the ground and the propeller plane (see Figure 4.1(a)). This effectively reduces the ground effect phenomenon that may

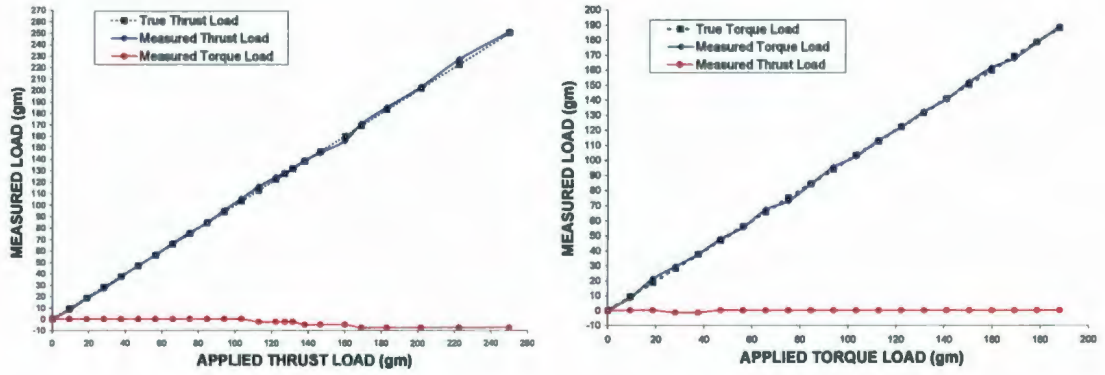

(a) Thrust affecting torque

(b) Torque affecting thrust

Figure 4.4: Interaction Curves

affect the thrust of the propeller when operating at high speeds. The performance variables of interest in this study are thrust, torque, rotational speed and power supplied to the motor under hovering condition (i.e., zero forward velocity). However, the effect of airflow around load cells were considered negligible in this work. By placing the test rig in a wind tunnel, a more extensive performance analysis of the propeller can be performed. Although the rig was designed to accommodate any propeller less than that 10 *inches* in diameter, this study reports some typical results for selected propellers based on their use. The nomenclature used here describes propeller manufacturer, diameter, pitch and weight. The first number after the propeller company name indicates the propeller diameter in inches and second number followed by a 'X' indicates pitch in *inches* and the information in the brackets is the weight. For example, APC 7 X 3 (5 *gm*) means it is an APC manufactured propeller with a diameter of 7 *inches*, a pitch of 3 *inches* and weight of 5 *gm*.

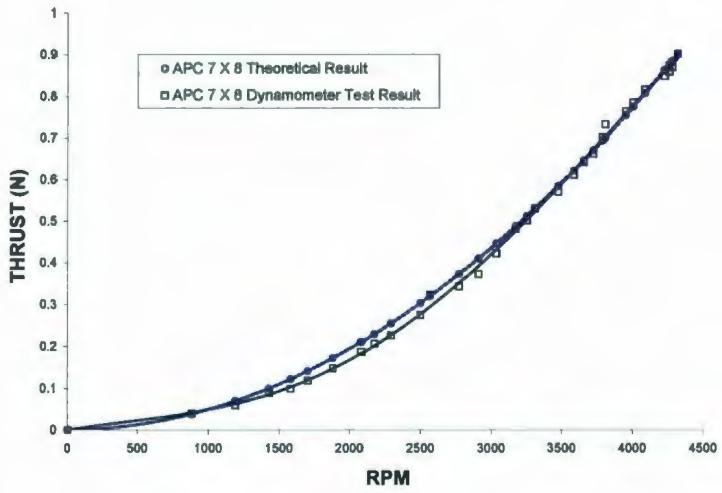

Figure 4.5: Data Validation

4.5 Results & Discussion

The propeller rig has been used extensively since its development. The first few runs were aimed towards the validation of the dynamometer accuracy, verifying repeatability and checking overall data quality. The validation of data was performed using a basic property of propeller performance. Namely, at zero wind speed the thrust produced by the propeller is proportional to the square of the rotational speed [7]. The comparative results in Figure 4.5 demonstrates the accuracy of the dynamometer. The data collected are for an APC 7 X 8 (12.38 gm). Figure 4.5 compares the two RPM versus thrust curves; one obtained from the dynamometer and the other from the theory mentioned above (i.e., thrust proportional to square of RPM). The coefficient used in this case is the standard value obtained from manufacturer. The validation and repeatability of the data found here were impressive and acceptable for this kind of dynamometer. Later a large number of propellers were tested. Since

all the results cannot be reported here, only a few representative results have been shown for the purpose of illustration. A website is currently under development which will provide the results of all the tests that were performed with this dynamometer.

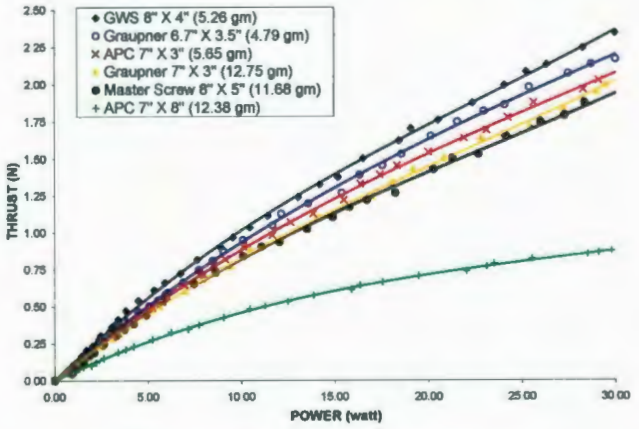

(a) Propeller Thrust Comparison

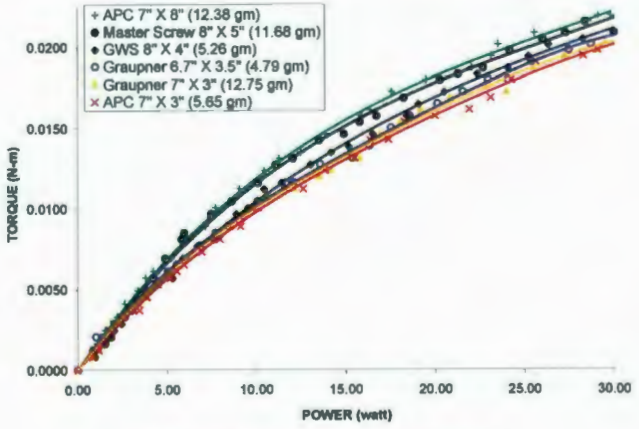

(b) Propeller Torque Comparison

Figure 4.6: Dynamometer Test Results

Figure 4.6(a) and 4.6(b) shows the test results for seven different propellers. Figure 4.6(a) clearly confirms that an increase in propeller diameter increases its capability in terms of producing thrust at a certain rotational speed; however, the result also

suggest that increasing the diameter may also result in an increase in weight of the propeller which contributes to a reduction of the thrust (e.g., APC 7 X 8 *in* Figure 4.6a). The tests performed in this study indicate that the highest thrust obtained was from an 8 *inch* diameter propeller and with a pitch of 4 *inches* and a weight of 5 *gm*. On the other hand Figure 4.6(b) confirms that an increase in pitch as well as the corresponding weight of a propeller increases torque required for a certain operational speed. These conclusion can be used to narrow down the selection of propellers for any particular application.

4.6 Conclusion

In this study, Fused Deposition Modeling was used to build the different parts of a dynamometer designed to characterize the performance of small propellers less than 10 *inches* in diameter for use in Unmanned Aerial Vehicles(UAVs). The basic design concept resulted in a very cost effective and efficient dynamometer that can be used to accurately measure the performance of propellers. Dynamic analysis of propellers can also be performed if the dynamometer is used in conjunction with a wind tunnel. The dynamometer was thoroughly tested and thrust and torque were recorded for a series of propellers.

4.7 Acknowledgments

This work is supported through the NSERC Discovery Grant Program as well the Boeing Chair in Mechatronic Design for Autonomous Systems at Memorial University.

The authors would also like to acknowledge the assistance of Mr. Don Taylor, a machinist in the Engineering Machine Shop, who assisted with the manufacture of the dynamometer.

References

[1] M. R. Hossain, G. Rideout, and N. Krouglicof, "Bond graph dynamic modeling and stabilization of a quadrotor helicopter," in *Proc. of International Conference on Bond Graph Modeling*, 2010.

[2] T. A. Dwarakanath, B. Dasgupta, and T. S. Mruthyunjaya, "Design and development of a stewart platform based force-torque sensor," *Mechatronics*, vol. 11, pp. 793–809, 2001.

[3] H. H. Li, K. R. Davis, M. H. Davy, and S. I. Green, "A marine propeller aerodynamic test facility," *Strain*, vol. 43, pp. 125–131, 2007.

[4] S. Yaldiz, F. Unsacar, H. Saglam, and H. Isik, "Design, development and testing of a four-component milling dynamometer for the measurement of cutting force and torque," *Mechanical Systems and Signal Processing*, vol. 21, pp. 1499–1511, 2007.

[5] K. M. Asson and P. F. Dunn, "Compact dynamometer system that can accurately determine propeller performance," *Journal of Aircraft*, vol. 29, pp. 8–9, January-February 1992.

[6] M. P. Marchent, "Propeller performance measurement for low reynolds number unmanned aerial vehicle applications," Master's thesis, Wichita State University, Kansas, USA, 2004.

[7] R. W. Prouty, "Helicopter performance, stability, and control," Krieger Publishing Company, Malabar, Florida, 1995.

Chapter 5

Visual Servoing of a Quad-rotor Helicopter Using Onboard Outwardly Looking Camera

M. Raju Hossain, Nicholas Krouglicof
Faculty of Engineering and Applied Science
Memorial University of Newfoundland
St. John's, Newfoundland, Canada

Abstract: *This paper presents the vision based pose estimation and control of a quad-rotor Unmanned Aerial Vehicle (UAV) using a single onboard camera observing a ground target that incorporates a minimum of five control points. The objective is to achieve control in six degrees of freedom as required for stabilization and maneuvering of a quad-rotor UAV for take-off/landing or flying at a relative distance from another unmanned vehicle. The ground target consists of five control points with known geometry and within the field of view of the camera. A quad-rotor dynamics and control model along with vision based pose estimation model is presented here. The pose estimation is achieved by processing the target image information and extracting the attitude and position information of the vehicle relative to that target.*

The pose of the vehicle is then utilized for stabilization and control of its maneuvers. A numerical experiment demonstrates a successful vision based control from an initial unstable pose of the vehicle and proves the algorithm feasibility as an option for precise takeoff/landing as well as relative navigation of a quad-rotor helicopter.

A version of this paper will be submitted to the "*IEEE International Conference on Mechatronics, 2011*" at the end of September 2010. The lead author is Mohammed Raju Hossain and the co-author is Dr. Nicholas Krouglicof. Mr. Hossain's contribution to this paper is as follows:

- Wrote the paper.
- Developed dynamics and control model for quad-rotor helicopter.
- Implemented vision based pose estimation technique for stabilization of quad-rotor helicopter.
- Performed Simulation and analysed the results.

Dr. Nicholas Krouglicof provided technical guidance and editing of the manuscript. In this chapter the manuscript is presented with altered figure numbers, table numbers and reference formats in order to match the thesis formatting guidelines set out by Memorial University.

5.1 Introduction

The study of Unmanned Aerial Vehicles is an intense field of research because of its various applications where human intervention is impossible, risky or expensive. Potential applications include exploration, search and rescue, and scientific data collection. A rotary wing unmanned vehicle (helicopter) if made fully autonomous can turn into a versatile platform for these applications due to its high maneuverability, ability to takeoff/land vertically, fly in limited spaces, etc. Unfortunately this agility makes its control more difficult due to dynamical instabilities and sensitive to disturbances.

For an autonomous helicopter to function successfully, take-off/landing is a crucial capability. Landing is particularly challenging since it requires precise knowledge of the relative orientation and position of the vehicle with respect to the landing surface. By applying vision based techniques, the pose of the vehicle can be estimated accurately, in real-time, and in a non-contact manner.

A great deal of active research has been conducted using vision for stabilization. Two major vision-based approaches can be found in the literature; the first is based on a single "outwardly looking" camera incorporated directly on the vehicle whereas the second approach relies on ground-based observation of the vehicle. From a practical point of view an on-board camera provides greater versatility. The authors in [1] demonstrate stabilization of position and yaw using four ground fixed markers. The remaining two degrees of freedom were collected using Inertial Measurement Units (IMU). Authors in [2] have exploited onboard cameras and special patterns on the ground to control and estimate the positions and the poses of aerial vehicles. However,

a stereo approach was adopted in this case. Some researchers have tried colored blobs as reference targets [3, 4, 5, 6]. The authors in [7] have estimated the attitude and position of the aerial vehicle based on sensing a target consisting of a Moire's Pattern. This technique is highly accurate when maintaining a very close distance between the target and the sensor. Besides all these vision based methods, various combination of lasers and GPS systems can also be used to determine vehicle pose in six Degrees of Freedom (DoF). Although all of these systems perform well, the quantity and quality of the camera or of the other sensors required to locate the object make their use either impractical or not cost effective. The solution proposed here is accurate, cost effective and easy to implement; however, it is computationally expensive.

5.2 Problem Definition

In urban or indoor environments as well as while taking off or landing from or on a moving platform, GPS is not always available or sufficiently accurate. Furthermore, integration of signals from inertial sensors like gyros and accelerometers leads to drift in the estimated variables. To solve this problem of feedback estimation, this paper proposes a solution for accurate estimation of states of a quad-rotor helicopter. The solution is achieved in two major steps. First we developed a realistic dynamic and control model of a four-rotor helicopter and later a model for determining its pose from a single perspective view of a redundant set of body fixed points (target). The vehicle model is based on Newton-Euler formalisms and is an extended version of the model previously presented by the same authors in [8]. On the other hand the pose estimation model is based on Euler-Rodriguez parameters and the quaternion

representation of the Finite Rotation Formula [9]. The estimation is performed using least square analysis on an overdetermined system of nonlinear equations. Finally, the pose estimation model is merged with the dynamic model as a state estimation sensor where the target orientation relative to the initial frame is known. The overall performance of the visual servoing model is evaluated as a first step towards future hardware implementation.

5.3 Helicopter Model

A quad-rotor helicopter is an underactuated dynamic vehicle whose lift is generated by four rotors (Figure 5.1). Control of such a craft is accomplished by varying the speeds of the four rotors relative to each other.

The front and the rear rotors rotate counterclockwise while the other two rotate clockwise, so that the gyroscopic effects and aerodynamic torque are canceled in trimmed flight. The rotors generate thrust forces (T) perpendicular to the plane of the rotors and moments (M) about x and y axes; moment about z-axis is obtained using counter torques of the rotor. Increasing or decreasing the speed of the four propellers permits climbing and descending.

Vertical rotation (yaw) is achieved by creating an angular speed difference between the two pairs of rotors which in turn creates reactive torques. Rotation about the longitudinal axis (pitch) and lateral axis (roll), and consequently horizontal motions, are achieved by tilting the vehicle. This is possible by decreasing the speed of one rotor while increasing the speed of the opposing rotor.

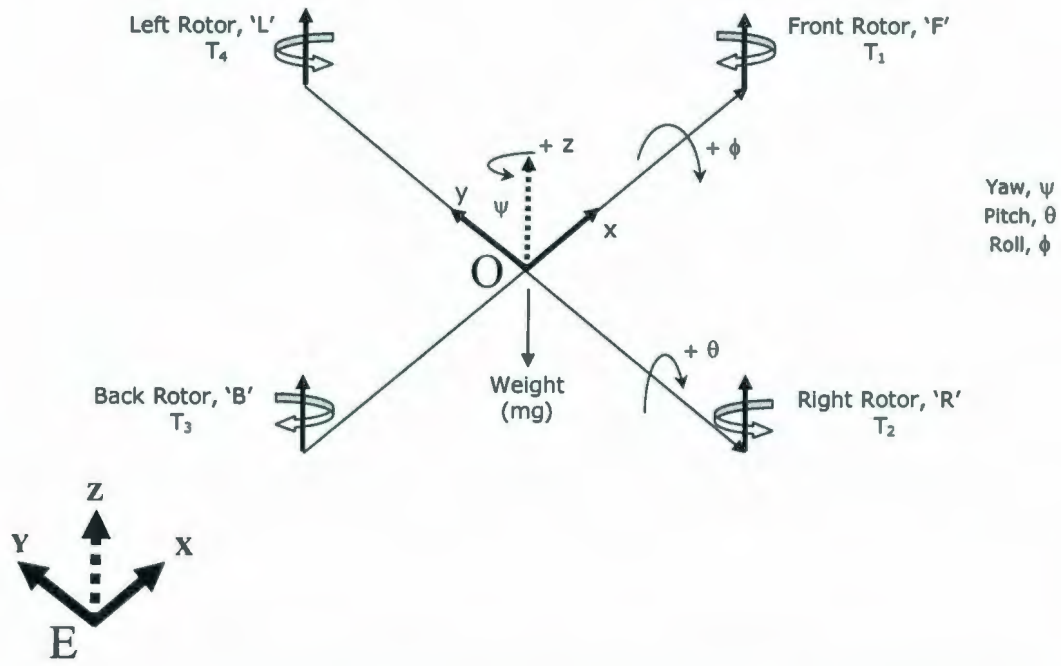

Figure 5.1: Quad-rotor Helicopter Schematic & Coordinates Considered for Modeling

5.3.1 Dynamics Model

A rigid airframe model of a three dimensional quad-rotor is given in Figure 5.1. All four propellers are assumed to be in the same horizontal plane and the quad-rotor structure is symmetric. A right-handed body fixed frame $O = x, y, z$ is placed at the centre of gravity of the quad-rotor and the z axis is pointing upward. Due to the double symmetry of the quad-rotor, it is logical to set the origin O at the intersection of the axes of the vehicle. The directions of the axes are chosen according to the most common convention in the literature. This results in a set of axes as shown in Figure 5.1. The body fixed frame $O = x, y, z$ is considered to be moving with respect to inertial frame (i.e., earth frame) $E = X, Y, Z$.

The equation of motion of such a rigid body, under external forces ($F_{external}$ and $M_{external}$) applied at the center of mass and expressed in the body fixed frame (O), are developed in the Newton-Euler formalism [10, 11]. With respect to these body fixed coordinates, the rotational inertia properties remain invariant and the products of inertia are all zero.

$$\begin{bmatrix} mI_{3\times3} & 0_{3\times3} \\ 0_{3\times3} & I \end{bmatrix} \begin{bmatrix} \dot{v}^b \\ \dot{\omega}^b \end{bmatrix} = \begin{bmatrix} F^b_{external} \\ M^b_{external} \end{bmatrix} - \begin{bmatrix} \omega^b \times (mv^b) \\ \omega^b \times (I\omega^b) \end{bmatrix} \tag{5.1}$$

Here, the body has absolute linear velocity $v^b \in \Re^3$ and absolute angular velocity $\omega^b \in \Re^3$. Total mass of the helicopter (neglecting added mass) and inertia of the body is denoted by $m \in \Re$ and $I \in \Re^{3\times3}$ respectively. $I_{3\times3} \in \Re^{3\times3}$ is an identity matrix.

However, in this case it can be useful to express the linear dynamic equation with respect to earth frame (E) and the angular dynamics equation with respect to body fixed frame (O). Therefore Equation 5.1 becomes:

$$\begin{bmatrix} mI_{3\times3} & 0_{3\times3} \\ 0_{3\times3} & I \end{bmatrix} \begin{bmatrix} \dot{v}^e \\ \dot{\omega}^b \end{bmatrix} = \begin{bmatrix} F^e_{external} \\ M^b_{external} \end{bmatrix} - \begin{bmatrix} 0_{3\times3} \\ \omega^b \times (I\omega^b) \end{bmatrix} \tag{5.2}$$

Here, $v^e \in \Re^3$ is linear velocity of the vehicle with respect to earth fixed frame and $F^e_{external}$ is the forces applied to the body with respect to earth fixed frame. Evaluating the external forces and moments produced in the vehicle due to the rotors speeds (Ω), earth gravity (g) yields:

$$\begin{bmatrix} F_x^e \\ F_y^e \\ F_z^e \\ M_x^b \\ M_y^b \\ M_z^b \end{bmatrix} = \begin{bmatrix} 0 \\ 0 \\ -m\,g \\ \mathbf{0_{3\times1}} \end{bmatrix} + I_r \begin{bmatrix} \mathbf{0_{3\times1}} & \mathbf{0_{3\times1}} & \mathbf{0_{3\times1}} & \mathbf{0_{3\times1}} \\ \omega_y & -\omega_y & \omega_y & -\omega_y \\ -\omega_x & \omega_x & -\omega_x & \omega_x \\ 0 & 0 & 0 & 0 \end{bmatrix} \begin{bmatrix} \Omega_1 \\ \Omega_2 \\ \Omega_3 \\ \Omega_4 \end{bmatrix} + \begin{bmatrix} \boldsymbol{R} & \mathbf{0_{3\times3}} \\ \mathbf{0_{3\times3}} & \boldsymbol{I_{3\times3}} \end{bmatrix} \begin{bmatrix} 0 \\ 0 \\ U_1 \\ U_2 \\ U_3 \\ U_4 \end{bmatrix} \tag{5.3}$$

The first contribution on the right hand side of Equation 5.3 is due to the gravitational force on the vehicle, whereas the next contribution is due to gyroscopic effects produced by the propeller rotation speed (Ω). Gyroscopic effects are only related to the angular motion of the vehicle. I_r is the total rotational moment of inertia of the motor and propeller about the axis of rotation. The third contribution is due to forces and moments created by changing the propeller speeds in order to control the vehicle. R is a 3×3 rotation matrix and U_1, U_2, U_3, U_4 are the maneuvering signal vector components which are defined as:

$$\begin{bmatrix} 0 \\ 0 \\ U_1 \\ U_2 \\ U_3 \\ U_4 \end{bmatrix} = \begin{bmatrix} 0 & 0 & 0 & 0 \\ 0 & 0 & 0 & 0 \\ b & b & b & b \\ 0 & -bl & 0 & bl \\ -bl & 0 & bl & 0 \\ -d & d & -d & d \end{bmatrix} \begin{bmatrix} \Omega_1^2 \\ \Omega_2^2 \\ \Omega_3^2 \\ \Omega_4^2 \end{bmatrix} \tag{5.4}$$

The length l is the distance between the center of gravity and the center of the rotors and Ω_1, Ω_2, Ω_3, Ω_4 are the four propeller speeds. b and d are thrust and drag factors which can be obtained experimentally as presented in [12] using a UAV propeller dynamometer. However, this can also be verified using the model described in [13]. A ZYX Euler angle representation has been chosen to represent rotations. Based on this representation, the rotation matrix R can be expressed in terms of the three Euler angles, yaw(ψ), pitch(θ) and roll(ϕ) as follows:

$$\boldsymbol{R} = \begin{bmatrix} \cos\theta\cos\psi & -\cos\phi\sin\psi + \sin\phi\sin\theta\cos\psi & \sin\phi\sin\psi + \cos\phi\sin\theta\cos\psi \\ \cos\theta\sin\psi & \cos\phi\cos\psi + \sin\phi\sin\theta\sin\psi & -\sin\phi\cos\psi + \cos\phi\sin\theta\sin\psi \\ -\sin\theta & \sin\phi\cos\theta & \cos\phi\cos\theta \end{bmatrix} \tag{5.5}$$

Thus Equation 5.2 and 5.3 leads to the system dynamics equation given below.

$$\left.\begin{aligned} \ddot{X} &= \frac{1}{m}(\sin\phi\sin\psi + \cos\phi\sin\theta\cos\psi)\,U_1 \\ \ddot{Y} &= \frac{1}{m}(-\sin\phi\cos\psi + \cos\phi\sin\theta\sin\psi)\,U_1 \\ \ddot{Z} &= \frac{1}{m}(\cos\phi\cos\theta)\,U_1 - g \\ \dot{\omega}_x &= \frac{I_{YY} - I_{ZZ}}{I_{XX}}\,\omega_y\,\omega_z - \frac{I_r}{I_{XX}}\,\omega_y\,\Omega + \frac{U_2}{I_{XX}} \\ \dot{\omega}_y &= \frac{I_{ZZ} - I_{XX}}{I_{YY}}\,\omega_x\,\omega_z + \frac{I_r}{I_{YY}}\,\omega_x\,\Omega + \frac{U_3}{I_{YY}} \\ \dot{\omega}_z &= \frac{I_{XX} - I_{YY}}{I_{ZZ}}\,\omega_x\,\omega_y + \frac{U_4}{I_{ZZ}} \end{aligned}\right\} \tag{5.6}$$

5.3.2 Control Model

The model given above is a highly non-linear system. It includes Newton-Euler equations, rotor dynamics, Gyroscopic effects, Coriolis effects and drag. For simplicity and ease of implementation of the controller, the roll, pitch and yaw angles are assumed to be small (as is the case during hovering). Under this assumption, the body angular parameters can be approximated by the Euler angle parameters. Thus we can rewrite the rotational acceleration function from Equation 5.6 as:

$$\left.\begin{aligned} \ddot{\phi} &= \frac{I_{YY} - I_{ZZ}}{I_{XX}}\,\dot{\theta}\,\dot{\psi} - \frac{I_r}{I_{XX}}\,\dot{\theta}\,\Omega + \frac{U_2}{I_{XX}} \\ \ddot{\theta} &= \frac{I_{ZZ} - I_{XX}}{I_{YY}}\,\dot{\phi}\,\dot{\psi} + \frac{I_r}{I_{YY}}\,\dot{\phi}\,\Omega + \frac{U_3}{I_{YY}} \\ \ddot{\psi} &= \frac{I_{XX} - I_{YY}}{I_{ZZ}}\,\dot{\phi}\,\dot{\theta} + \frac{U_4}{I_{ZZ}} \end{aligned}\right\} \tag{5.7}$$

Note that the linear motion of the helicopter is related to change in the tilt angle of the vehicle. A PD controller can be designed to control the vehicle motion in the x direction by controlling the pitch (θ) angle. Similarly motion in the y direction can be achieved by controlling roll (ϕ). The form of the PD controller to control motion in the x direction is given by:

$$U_X = \left(k_{p,X}\,(X_d - X) + k_{d,X}\,(\dot{X}_d - \dot{X}) \right) \frac{m}{U_1} \tag{5.8}$$

In Equation 5.9 below, the desired tilt angle is obtained using the first relationship presented previously in Equation 5.6. The form of the PD controller to control the desired tilt angle is illustrated in Equation 5.10.

$$\theta_d = \arcsin(U_X - \frac{\sin\phi \ \sin\psi}{\cos\phi \ \cos\psi}) \tag{5.9}$$

$$U_3 = \ k_{p,pitch} \ (\theta_d - \theta) + k_{d,pitch} \ (\dot{\theta}_d - \dot{\theta}) \tag{5.10}$$

Similarly we can define the PD controller to control the motion in the y direction.

$$U_Y = (\ k_{p,Y} \ (Y_d - Y) + k_{d,Y} \ (\dot{Y}_d - \dot{Y}) \ ) \ \frac{m}{U_1} \tag{5.11}$$

The above control signal defines the required roll using Equation 5.8 and the second relation in Equation 5.6.

$$\phi_d = \arcsin(U_X \ \sin\psi - U_Y \ \cos\psi) \tag{5.12}$$

$$U_2 = \ k_{p,roll} \ (\phi_d - \phi) + k_{d,roll} \ (\dot{\phi}_d - \dot{\phi}) \tag{5.13}$$

On the other hand, the altitude and the yaw angle can also be controlled by PD controllers,

$$U_1 = \frac{m}{\cos\phi \ \cos\theta}(g + k_{p,Z} \ (Z_d - Z) + k_{d,Z} \ (\dot{Z}_d - \dot{Z})) \tag{5.14}$$

$$U_4 = k_{p,yaw} \ (\psi_d - \psi) + k_{d,yaw} \ (\dot{\psi}_d - \dot{\psi}) \tag{5.15}$$

Note that a stable flight/hovering condition can be achieved simply by controlling altitude, U_1 and tilt angles (U_2, U_3, U_4). k_p and k_d represent the proportional and derivative gains respectively of the PD controller.

5.4 Pose Estimation

In this section the target based vision system is modeled to determine the position and orientation of a rigid body in six DoF. A brief introduction into quaternion algebra, the Finite Rotation Formula, as well as Euler's theorem is presented in order to better understanding the approach.

5.4.1 Finite Rotation Formula

Euler theorem states that the most general displacement of a rigid body with a fixed point A is equivalent to a rotation of that body about an axis through A. Let the axis of rotation be defined by a unit vector $\bar{n}$ and the angle of rotation by Φ. The four Euler-Rodriguez parameters a, b, c and d are defined in terms of $\bar{n}$ and Φ as follows

$$a = n_x \sin(\frac{\Phi}{2}), b = n_y \sin(\frac{\Phi}{2}), c = n_z \sin(\frac{\Phi}{2}), a = \cos(\frac{\Phi}{2}) \tag{5.16}$$

Note that the parameters a, b and c represent the components of a vector with the direction $\bar{n}$ and magnitude $\sin(\frac{\Phi}{2})$ whereas the parameter d represents the scalar quantity $\cos(\frac{\Phi}{2})$. The advantage of using Euler-Rodriguez representation is, it does not degenerate for any angular orientation, and the computational cost associated is less compared to direction cosine or Euler angles [14]. One of the main applications of Euler-Rodriguez Parameters is found in the quaternion representation of Finite Rotation Formula. Thus a brief introduction to quaternion representation is given below.

Let, the set $A = 1, \bar{i}, \bar{j}, \bar{k}$ be a basis of a vector space $\boldsymbol{V}$ of dimension four over

the set of real numbers. The first element in the set is the scalar unit 1. The other three elements are mutually perpendicular unit vectors which obey the following laws of combination.

$$\begin{aligned} \bar{i}^2 = \bar{j}^2 = \bar{k}^2 = -1 \\ \bar{i} \times \bar{j} = \bar{k},\ \bar{j} \times \bar{i} = -\bar{k} \\ \bar{j} \times \bar{k} = \bar{i},\ \bar{k} \times \bar{j} = -\bar{i} \\ \bar{k} \times \bar{i} = \bar{j},\ \bar{i} \times \bar{k} = -\bar{j} \end{aligned} \tag{5.17}$$

The equation q is a linear combination of the elements of the basis A, i.e.:

$$q = d + a\bar{i} + b\bar{j} + c\bar{k} \tag{5.18}$$

Here $a, b, c, d \in \Re$. Every nonzero quaternion has a multiplicative inverse given by,

$$q^{-1} = \frac{q^*}{qq^*} \quad where, q^* = d - a\bar{i} - b\bar{j} - c\bar{k} \tag{5.19}$$

The quaternion q^{-1} and q^* are referred to as the reciprocal and conjugate of q respectively.

Now let us consider, $\bar{r}$ and $\bar{r}'$which defines the position of a body-fixed point P before and after a general change in the orientation.

$$\begin{aligned} \bar{r} = x\bar{i} + y\bar{j} + z\bar{k} \\ \bar{r}' = x'\bar{i} + y'\bar{j} + z'\bar{k} \end{aligned} \tag{5.20}$$

The two vectors $\bar{r}$ and $\bar{r}'$ can be related by the quaternion representation of finite

rotation formula.

$$\bar{r}' = q\,\bar{r}\,q^{-1} \tag{5.21}$$

The coefficients of the quaternion q appearing in equation 5.21 are the four Euler Rodriguez parameters a, b, c and d defined by the Equation 5.16. By performing the quaternion multiplication indicated in the Equation 5.21 and collecting the coefficients of $1, \bar{i}, \bar{j}, \bar{k}$ the finite rotation formula can be written in matrix form. Note that in the quaternion algebra, a vector is simply a quaternion whose scalar part d is equal to zero.

$$\begin{bmatrix} x' \\ y' \\ z' \end{bmatrix} = \begin{bmatrix} T \end{bmatrix} \begin{bmatrix} x \\ y \\ z \end{bmatrix} \tag{5.22}$$

$$\text{where, } \begin{bmatrix} T \end{bmatrix} = \frac{1}{a^2+b^2+c^2+d^2} \begin{bmatrix} d^2+a^2+b^2+c^2 & 2(ab-cd) & 2(ac+bd) \\ 2(ab+cd) & d^2-a^2+b^2-c^2 & 2(bc-ad) \\ 2(ac-bd) & 2(bc+ad) & d^2-a^2-b^2+c^2 \end{bmatrix}$$

The coefficients of the scalar component in Equation 5.22 are equal to zero, therefore $\bar{r}'$ is clearly a vector. Since it is difficult to visualize the orientation of a rigid body given the Euler-Rodriguez parameters, the orthogonal transformation matrix $[T]$ in Equation 5.22 is useful in converting to more conventional kinematics representation of the rigid body motion (i.e. direction cosines or Euler angles).

If both the sides of Equation 5.21 are multiplied by quaternion q, then:

$$\bar{r}' \, q = q \, \bar{r} \tag{5.23}$$

Since this is a statement of equality between two quaternions, their corresponding components must be equal. There are four components, hence four equations which are linear with respect to the Euler-Rodriguez parameters a, b, c, d. These equations can be found by performing the two quaternion multiplications and collecting the coefficients of $1, \bar{i}, \bar{j}, \bar{k}$.

$$\left.\begin{array}{rrrrl} (x'-x)a & +(y'-y)b & +(z'-z)c & +0 & =0 \\ 0 & -(z'+z)b & +(y'+y)c & +(x'-x)d & =0 \\ -(z'+z)a & 0 & -(x'+x)c & +(y'-y)d & =0 \\ -(y'+y)a & +(x'+x)b & 0 & +(z'-z)d & =0 \end{array}\right\} \tag{5.24}$$

Note that these homogeneous equations are not only linear with respect to the Euler-Rodriguez parameters a, b, c, d but also with respect to the coordinates of the body-fixed points before and after a general change in orientation. The determinant of the matrix formed by the coefficients of the parameters equals to zero, as does the determinant of every sub matrix of the order three, hence there are only two independent equations in this set. Furthermore, the four Euler-Rodriguez parameters are not independent and must satisfy the relation:

$$a^2 + b^2 + c^2 + d^2 = 1 \tag{5.25}$$

Since only the ratios of the four Euler-Rodriguez parameters are defined, one of the parameters can be arbitrarily set to unity. This operation can be reworded as

"normalizing" with respect to one of the parameters. Normalizing with respect to the parameter d, for example, yields the following set of orientative parameters:

$$\rho_1 = n_x \tan(\frac{\Phi}{2}),\ \rho_2 = n_y \tan(\frac{\Phi}{2}),\ \rho_3 = n_z \tan(\frac{\Phi}{2}) \tag{5.26}$$

The three orientative parameters ρ_1, ρ_2, ρ_3 which are referred to in the literature as the Rodriguez parameters can be used to efficiently represent rigid body motion. However, they tend to degenerate as the angle of rotation Φ about the unit vector $\bar{n}$ approaches π. Consequently, as Φ approaches π, the Euler-Rodriguez parameters must be normalized with respect to one of the remaining non-zero parameters, a, b or c [15].

5.4.2 Monocular Pose Estimation

The pose estimation technique considered here involves lens-camera assembly which looks into a target consisting of five unique points. The lens-camera assembly and a brief study of the geometry of the camera are in order.

Figure 5.2 represents a conventional lens-camera assembly in which each point in the viewing space is projected towards the focal center C of the lens and onto the sensitive surface of the camera. The position of the image point is defined by two coordinates, x_d and y_d which are provided by the camera. The vector $\bar{R}_i$ defines the position of target point P_i with respect to the focal center of the lens. The angles α_i, β_i and γ_i are formed by the vector and the X_s, Y_s and Z_s axes respectively. The cosines of these angles are referred to as the direction cosines of $\bar{R}_i$ with respect to the camera coordinate system.

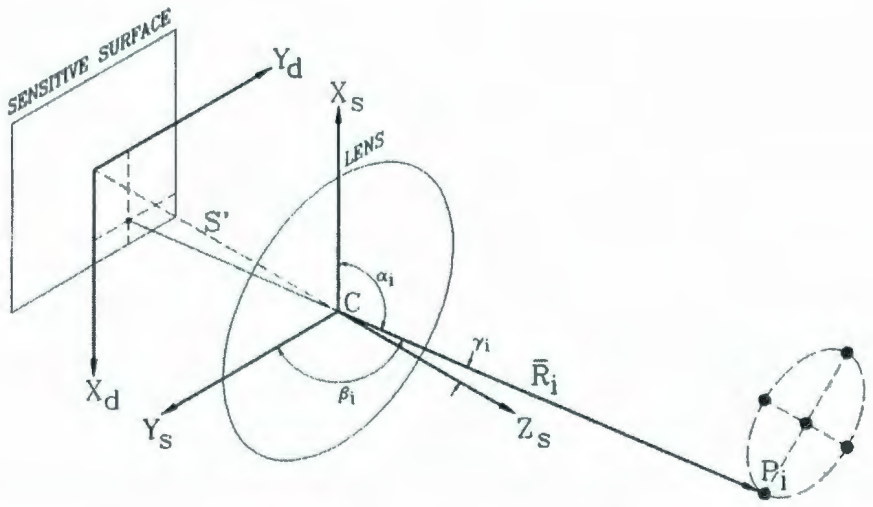

Figure 5.2: Schematic Representation of Lens Camera Assembly

The three direction cosines can be expressed as functions of the effective focal length of the lens, S', and the image coordinates, x_d and y_d as follows:

$$\left.\begin{aligned} \cos(\alpha_i) &= \frac{x_d}{D} \\ \cos(\beta_i) &= \frac{y_d}{D} \\ \cos(\gamma_i) &= \frac{S'}{D} \\ where, D &= \sqrt{S'^2 + x_d^2 + y_d^2} \end{aligned}\right\} \tag{5.27}$$

The vector $\bar{R}_i$ is completely specified by its length, l_i, which is as yet unknown and its direction cosines.

$$\bar{R}_i = l_i[\cos(\alpha_i)\bar{i}_s + \cos(\beta_i)\bar{j}_s + \cos(\gamma_i)\bar{k}_s] \tag{5.28}$$

In order to apply the finite rotation formula, one of the target points must be arbitrarily selected to represent the origin of the body-fixed coordinate system (i.e.,

the fixed point A in Euler's theorem). This point, which remains stationary during a pure change in orientation, is denoted as P_o. For each of the remaining points, the vector $\bar{r}_i'$ defines the final position of the point P_i with respect to the origin of the body-fixed coordinate system. The vector $\bar{r}_i'$ can be expressed in terms of the position vectors $\bar{R}_i$ and $\bar{R}_o$ as follows:

$$\bar{r}_i' = \bar{R}_i - \bar{R}_o \tag{5.29}$$

Recall that while the directions of $\bar{R}_i$ and $\bar{R}_o$ are known relative to the camera coordinate system, their lengths, l_i and l_o, have yet to be determined.

Equation 5.30 provides a means of expressing the final point coordinates, x_i', y_i' and z_i' in terms of the measured direction cosines.

$$\left.\begin{aligned} x_i' &= l_i \cos(\alpha_i) - l_o \cos(\alpha_o) \\ y_i' &= l_i \cos(\beta_i) - l_o \cos(\beta_o) \\ z_i' &= l_i \cos(\gamma_i) - l_o \cos(\gamma_o) \end{aligned}\right\} \tag{5.30}$$

By substituting Equation 5.30 into Equation 5.24, the quaternion representation of the finite rotation formula can be expressed in terms of the measured direction cosines:

$$
\left.
\begin{array}{lll}
(\mathrm{l}_i \cos(\alpha_i) - l_o \cos(\alpha_o) - x)a & +(\mathrm{l}_i \cos(\beta_i) - l_o \cos(\beta_o) - y)b & \\
+(\mathrm{l}_i \cos(\gamma_i) - l_o \cos(\gamma_o) - z)c & 0 & = 0 \\
 & & \\
0 & -(\mathrm{l}_i \cos(\gamma_i) - l_o \cos(\gamma_o) + z)b & \\
+(\mathrm{l}_i \cos(\beta_i) - l_o \cos(\beta_o) + y)c & +(\mathrm{l}_i \cos(\alpha_i) - l_o \cos(\alpha_o) - x)d & = 0 \\
 & & \\
-(\mathrm{l}_i \cos(\gamma_i) - l_o \cos(\gamma_o) + z)a & 0 & \\
-(\mathrm{l}_i \cos(\alpha_i) - l_o \cos(\alpha_o) + x)c & +(\mathrm{l}_i \cos(\beta_i) - l_o \cos(\beta_o) - y)d & = 0 \\
 & & \\
-(\mathrm{l}_i \cos(\beta_i) - l_o \cos(\beta_o) + y)a & +(\mathrm{l}_i \cos(\alpha_i) - l_o \cos(\alpha_o) + x)b & \\
0 & +(\mathrm{l}_i \cos(\gamma_i) - l_o \cos(\gamma_o) - z)d & = 0
\end{array}
\right\} \quad (5.31)
$$

In this case, the quaternion representation of the finite rotation formula results in a set of $4(n-1)$ nonlinear equations of which only $2(n-1)$ are independent. A two-dimensional perspective projection of a set of n body-fixed points yields $(3+n)$ unknowns; three independent orientative parameters as well as one range parameter for each of the body-fixed points. Thus a minimum of five body-fixed points are required to arrive at a unique solution. A set of six or more body-fixed points represents an overdetermined set of equations which can increase the accuracy of the measurement through the application of least-squares analysis. In order to take full advantage of the redundancy, the orientative and range parameters are evaluated iteratively through the application of nonlinear least-squares estimation.

Based on the arbitrary starting point, the pose of the body can be generally determined within six iterations. However, if the velocity of the body is small and tracked continuously which in the case of the quad-rotor is very reasonable, then the initial estimates of the unknown parameters are typically accurate and significantly fewer iterations are required.

5.5 Results

In this section the simulated response of the overall vision-based control model for a quad-rotor helicopter is presented. An ideal lens-camera model with no distortion and known focal length has been considered for the purposes of the simulation. The coordinates of the five control points with known geometry are projected onto the image sensor and then fed into the pose estimation model in order to get the orientation and position the camera with respect to target. Based on the pose information provided by the vision system, the controller defines the required command signals for thrust, roll, pitch and yaw. This combination of signals drives the four propellers and creates the dynamics in the quad-rotor which follows the model derived earlier. The new states are considered as the next input from the camera model is received. A block diagram of the complete system is presented in Figure 5.3.

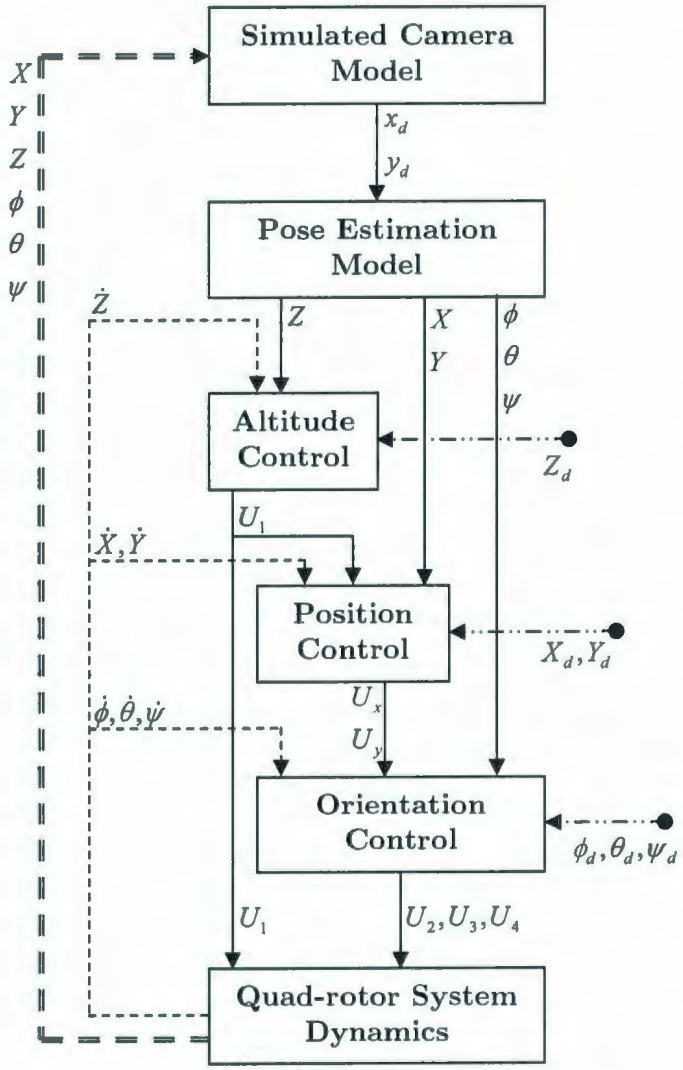

Figure 5.3: Block Diagram of Vision Based Quad-rotor Control Model

Figure 5.4 shows the dynamic performance of the quad-rotor vehicle starting from an arbitrary orientation and returning to the zero or hovering position. The desired orientation in roll(ϕ), pitch(θ) and yaw(ψ) are set to zero since this is generally the normal steady-state condition for a quad-rotor vehicle that is transitioning between two locations in space.

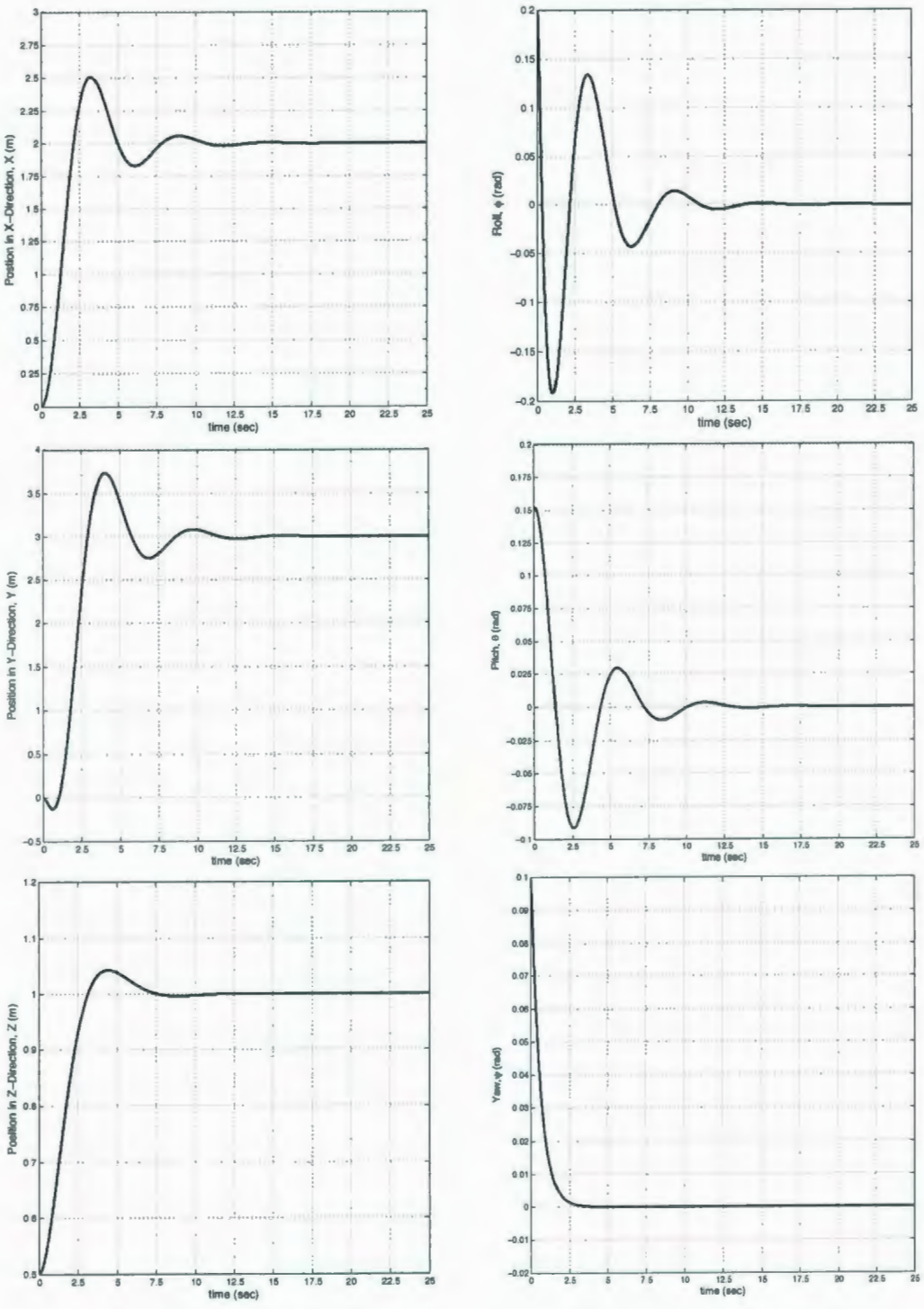

Figure 5.4: PD Controller Simulation Using Vision System as Feedback

The desired X_d, Y_d positions and altitude Z_d are 2 m, 3 m and 1 m respectively. The transient responses confirm a stable flight of the quad-rotor as it transitions between the two positions and confirms the success of the overall algorithm presented in this work.

5.6 Conclusion

The implementation of the vision based pose estimation technique involves an iterative, least-squares solution to an overdetermined system of nonlinear equations. Such an approach is generally ill-suited to real-time implementations; however, the technique presented here can be implemented using floating point addition and multiplication alone and can be easily run on contemporary embedded platforms.

This paper demonstrates that a vision-based approach to determining pose based on a single "outwardly looking" camera offers an accurate and cost effective means of stabilizing and controlling a quad-rotor UAV. The relative motion information provided by the vision system is especially critical when landing on a moving platform such as a ship at sea or another autonomous platform.

Acknowledgements

This work is supported through the NSERC Discovery Grant Program as well the Boeing Chair in Mechatronic Design for Autonomous Systems at Memorial University.

APPENDIX

Table 5.1: Parameters Used in Vision Based Control Simulation

Symbol	Quantity	Value	Units
	Vehicle Parameters		
m	Mass of the Quad-rotor	0.973	kg
g	Gravitational Acceleration	9.81	ms^{-2}
I_{XX}	Body moment of Inertia about x-axis	8.665×10^{-3}	$kg\,m^3$
I_{YY}	Body moment of Inertia about y-axis	8.665×10^{-3}	$kg\,m^3$
I_{ZZ}	Body moment of Inertia about z-axis	16.53×10^{-3}	$kg\,m^3$
b	Thrust Factor	1.15×10^{-5}	
d	Drag Factor	2.29×10^{-7}	
	Solver Parameters (RK4)		
t_i	Initial Time	0	sec
t_f	Final Time	25	sec
Δt	Step Size	0.01	sec
	Camera Model Parameters		
f	Focal Length	0.016	m
	Pose Estimation Moldel Parameters		
$(x,y,z)_1$	Coordinate of Control Point 1	(0,0,0)	m
$(x,y,z)_2$	Coordinate of Control Point 2	(0.015,0,0)	m
$(x,y,z)_3$	Coordinate of Control Point 3	(0,0.015,0)	m
$(x,y,z)_4$	Coordinate of Control Point 4	(-0.015,0,0)	m
$(x,y,z)_5$	Coordinate of Control Point 5	(0,-0.015,0)	m
	Controller Parameters		
$k_{p,X}$	Proportional Gain for X-axis Position Control	0.8	
$k_{d,X}$	Derivative Gain for X-axis Position Control	1.1	
$k_{p,Y}$	Proportional Gain for Y-axis Position Control	0.8	
$k_{d,Y}$	Derivative Gain for Y-axis Position Control	1.1	
$k_{p,Z}$	Proportional Gain for Altitude Position Control	0.8	
$k_{d,Z}$	Derivative Gain for Altitude Position Control	0.7	
$k_{p,\phi}$	Proportional Gain for Roll Control	0.8	
$k_{d,\phi}$	Derivative Gain for Roll Control	0.9	
$k_{p,\theta}$	Proportional Gain for Pitch Control	0.8	
$k_{d,\theta}$	Derivative Gain for Pitch Control	0.9	
$k_{p,\psi}$	Proportional Gain for Yaw Control	0.8	
$k_{d,\psi}$	Derivative Gain for Yaw Control	0.5	

References

[1] H. Romero, R. Benosman, and R. Lozano, "Stabilization and location of a four rotor helicopter applying vision," in *Proc. of The American Control Conference*, 2006.

[2] C. Xu, L. Qiu, M. Liu, B. Kong, and Y. Ge, "Stereo vision based relative pose and motion estimation for unmanned helicopter landing," in *Proc. of The IEEE International Conference on Information Acquisition*, 2006.

[3] E. Altug, J. P. Ostrowski, and C. J. Taylor, "Quadrotor control using dual camera visual feedback," in *IEEE International Conference on Robotics and Automation*, 2003.

[4] M. Earl and R. D. Andre, "Real-time attitude estimation techniques applied to a four rotor helicopter," in *IEEE Conference on Decision and Control*, 2004.

[5] L. M. Mak and T. Furukawa, "A 6 DoF visual tracking system for a miniature helicopter," in *2nd International Conference on Sensing Technology*, 2007.

[6] O. Amidi, T. Kanade, and K. Fujita, "A visual odometer for autonomous helicopter flight." *Journal of Robotics and Autonomous Systems*, vol. 28, pp. 185 – 193, 1999.

[7] G. Tournier, M. Valenti, J. P. How, and E. Feron, "Estimation and control of a quadrotor vehicle using monocular vision and moire patterns," in *AIAA Guidance, Navigation, and Control Conference and Exhibit*, 2006.

[8] M. R. Hossain, D. G. Rideout, and N. Krouglicof, "Bond graph dynamic modeling & stabilization of a quad-rotor helicopter," in *9th International Conference on Bond Graph Modeling & Simulation*, 2010.

[9] N. Krouglicof, *Rigid-Body Pose Measurement.* Intelligent Autonomous Systems, ch. 37, pp. 368 – 377.

[10] R. Murray, S. Sastry, and L. Zexiang, *A Mathematical Introduction to Robotic Manipulation.* Boca Raton, FL, USA: CRC Press, Inc (ISBN: 0849379814), 1994.

[11] J. Ginsberg, *Advanced Engineering Mechanics*, 2nd ed. Cambridge University Press, 1995.

[12] M. R. Hossain and N. Krouglicof, "Propeller dynamometer for small unmanned aerial vechile," in *23rd Canadian Conference on Electrical and Computer Engineering*, 2010.

[13] R. Prouty, *Helicopter Performance, Stability and Control.* Kreiger Publishing Company, 1995.

[14] H. Cheng and K. Gupta, "An historical note on finite rotations," *ASME Journal of Applied Mechanics*, vol. 56, pp. 139 – 145, 1989.

[15] G. Schut, "On exact linear equations for the computation of the rotational elements of absolute orientation," *Photogrammetria*, vol. 17, no. 1, pp. 3 – 37, 1960.

Chapter 6

Platform Development and Control Implementation

This chapter presents the hardware development of a small quad-rotor (i.e., four rotors in a cross configuration) helicopter. The width and length are 720 mm while the height is 110 mm. The entire system including batteries weighs 1065 gm. This chapter also discusses the feedback sensors employed for controlling the platform and finally discusses the result of the preliminary testing. It should be noted that most of the components used in development of the quad-rotor are commercially available. The step by step development process is presented below.

6.1 Frame Development

The initial goal for the quad-rotor required extended payload capacity (i.e., able to carry additional sensors on top of the equipment needed for flight including the motors, frame and batteries). To reduce the weight of the platform while maintaining

strength, carbon fiber rods were used for the basic structure. The carbon fiber rods weigh 7 *gm* each and are attached at the center with a small, rapid prototyped block of Acrylonitrile Butadiene Styrene (ABS) material. The block was kept as light as possible to reduce weight. Figure 6.1(a) shows the carbon rods fixed to the center block.

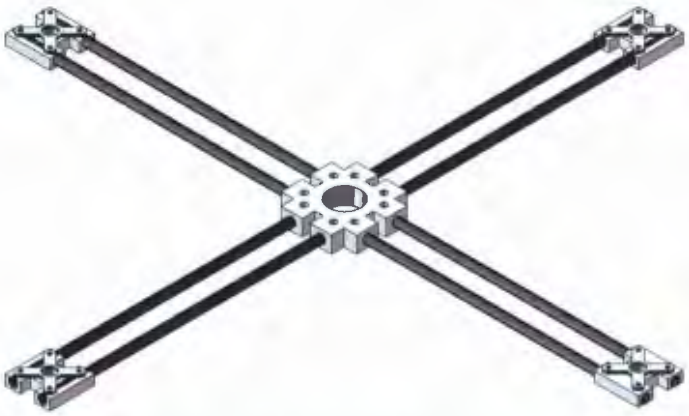

(a) Carbon Rod Attached to Center Block

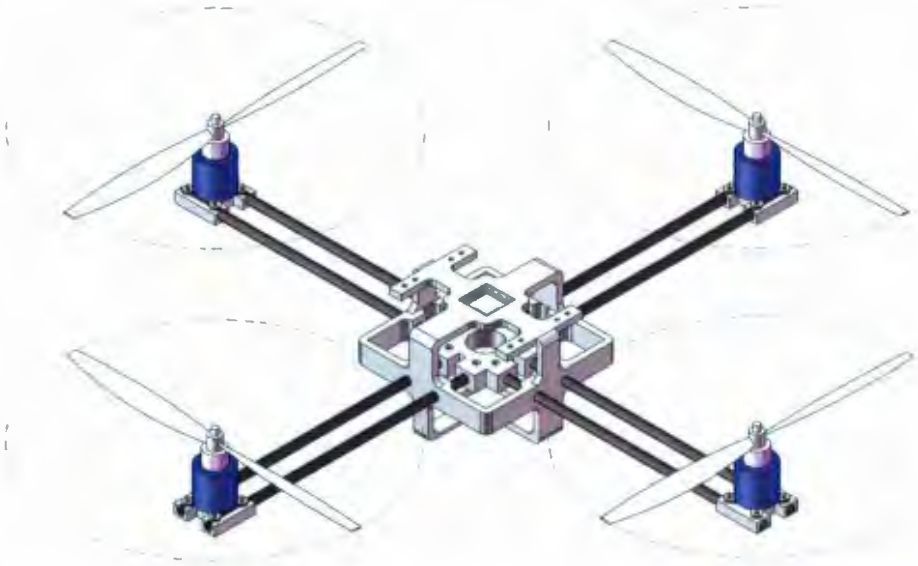

(b) Solidworks Impression of Quad-rotor

Figure 6.1: Basic Structure of the Quad-rotor Platform

Later in the design process a square skeletal frame (to reduce weight) was made to hold batteries and other electronics devices. This frame was made from the same ABS material. Figure 6.1(b) shows the basic quad-rotor structure. The platform without any equipment weights only 152 gm which is less than the amount of thrust provided by single motor-propeller arrangement. Note that a single motor-propeller arrangement used in this work is capable of providing 385 gm at full power, creating a provision to lift almost 1500 gm with all four propellers running at full power. The dimension of the quad-rotor frame is 50 cm $\times$ 50 cm without the propellers and 72 cm $\times$ 72 cm with the propellers. Four APC 12 $\times$ 4.7 propellers are used in the quad-rotor. "12" refers to the diameter of the propeller in *inches* and "4.7" is the pitch in *inches*.

6.2 Avionics

Before implementing vision based control, stabilization was obtained using rate gyros, accelerometer and magnetometer as feedback sensors. Four brushless DC (BLDC) motors have been used in conjunction with two pairs of APC 10 $\times$ 4.7 counter-rotating propellers directly coupled to the motor (i.e., direct drive). A light weight single board computer (x86 architecture-based) is used to control the four motors as well as acquire feedback from the sensors. A pair of 2200 mAh 11.1 V Lithium Polymer batteries are used for supplying power to the overall system. The description of all the avionics is provided below.

6.2.1 Rotor System

A direct drive rotor system (motor-propeller combination) has been chosen for driving the propellers. The four brushless DC motors are controlled using appropriate Electronic Speed Controllers (ESC). The propellers are mounted directly on the motor shaft; i.e., without any gears. This reduces the power consumption compared with geared system.

Figure 6.2: Direct Drive Rotor System

The onboard computer is used to generate the PWM signals used to drive the motors via the ESC. Changing the pulse width of the signal changes the speed of the motor thus adjusting the thrust produced by the propellers. The brushless motors used in this work are commercially available Hacker Style Brushless Outrunner 20-22L weighing only 59 *gm* and the controllers were "Turnigy Plush 18 *Amp* Speed Controller". The motors were arranged to operate at an average of 80 *watts*, however, they can draw a maximum of 17 *amps* @ 11 *volts*. The PWM Signals used to control the motor are standard RC servo PWM with a base frequency of 50 Hz and a pulse width of 1 to 2 *ms*.

6.2.2 Inertial Measurement Sensors

For initial stabilization of the quad-rotor helicopter two inertial sensors and a magnetic sensors have been used. The two inertial sensors are; 3-axis Micro Electro-Mechanical System (MEMS) accelerometers ("RMG-144) for measuring the accelerations in the three orthogonal axes of the body and a MEMS gyroscope ("RMG-145) for measuring rate of tilt with respect to the three body axes. All the sensors have been interfaced with the controller board through 13 bit Analog to Digital converter (ADC). The communication between the processor board and the sensors were via I^2C. Each of the sensors weighs 2.5 gm without connecting wires and the required power of operation is $5V$ DC. Figure 6.3(a) and Figure 6.3(b) shows rate gyro and a combination of accelerometer and magnetometer sensor respectively.

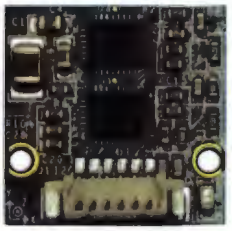

(a) Gyroscope/rate sensor

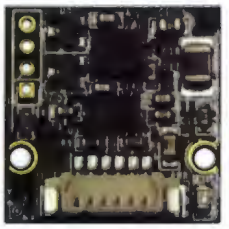

(b) Accelerometer and Magnetometer

Figure 6.3: Inertial Sensors Photo

6.2.3 Controller Board

The controller board used in this work is also a commercially available controller based on Vortex86DX processor. The commercial name of this board is "RoBoard". It is a

32bit x86 CPU running at 1000MHz with 256MB DRAM. The board weighs only 50 gm without wiring and consumes 2 $Watt$ of power. The main I/O ports used are the PWM output channel for running the motors of the quad-rotor, I^2C communication used to read the sensors, and the ADC. The C++ programming language is used to develop the code for stabilizing the quad-rotor. The controller has many other features for future development. Figure 6.4 shows the photo of the controller board and Figure 6.5 shows the architecture of the board.

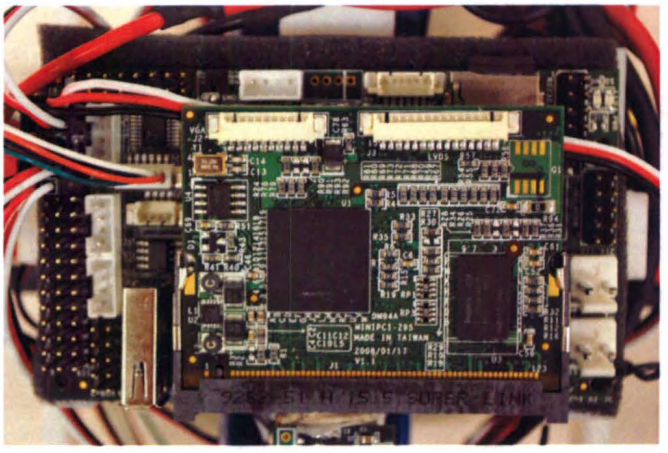

Figure 6.4: Photo of Controller Board (RoBoard)

6.2.4 Power System

The selection of the power supply for a quad-rotor depends on the required flight time as well as the maximum payload of the vehicle. In order to increase the useful payload, the battery weight must be reduced resulting in reduced flight time. On the other hand increasing the battery capacity increases flight time but reduces payload. Keeping this in mind, a pair of 2200 mAh 3S Lithium Polymer (LiPo) batteries

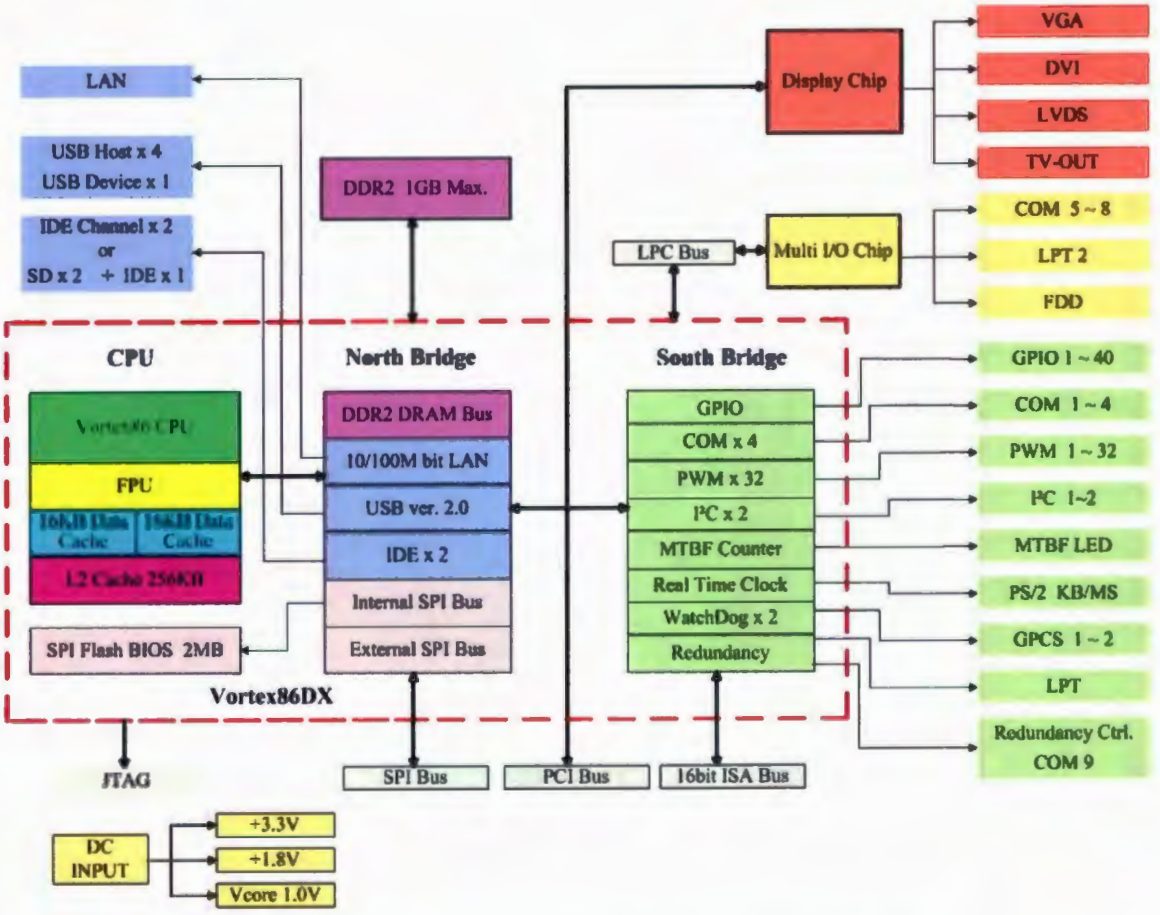

Figure 6.5: Architecture of the Controller Board

were selected. These weigh 200 *gm* each without wirings which results in 500 *gm* of payload from the vehicle and a 10 min of flight time. However, if two 4400 mAh 3S LiPo batteries are used the payload drops to 120 *gm* increasing the flight time to 20 min. The flight time is calculated considering an average power consumption of 7 *amps* per motor.

6.3 Mass Distribution and Overall Design

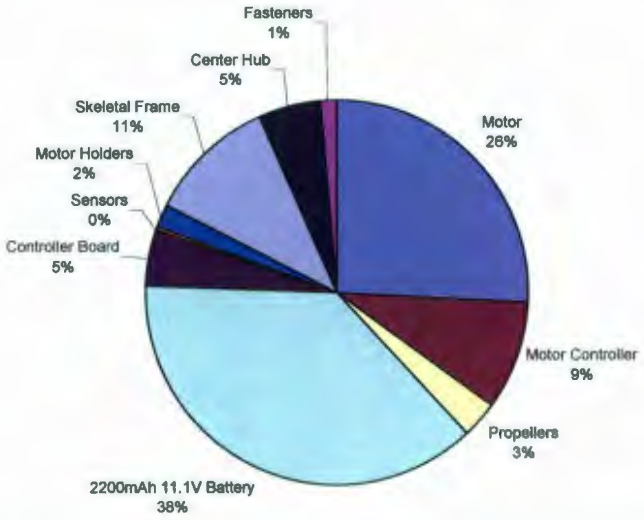

Figure 6.6: Mass Distribution of Quad-rotor (Total Mass 1065 gm)

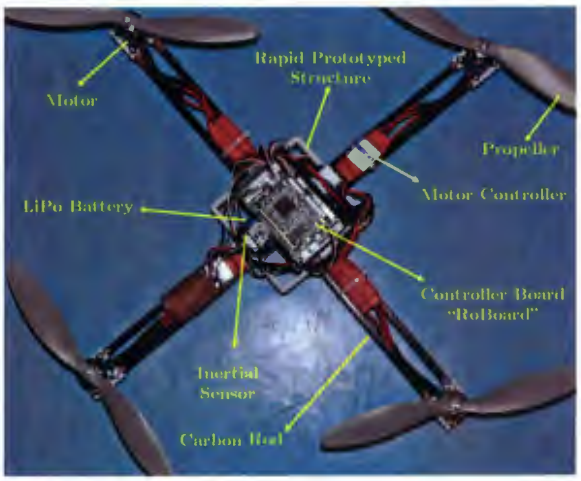

Figure 6.7: Photo of the Quad-rotor Platform

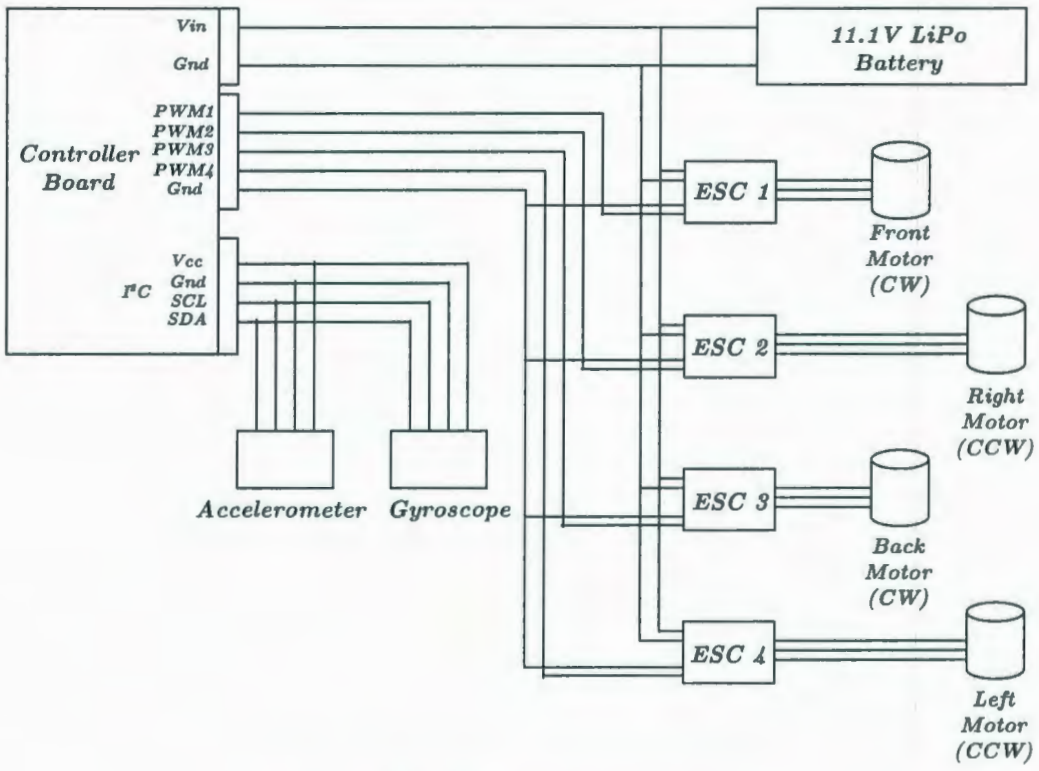

Figure 6.8: Circuitry of Quad-rotor

6.4 Identification of the constants

The quad-rotor development involves identifying numerous parameters depending on the geometry and the aerodynamics components selected. There are different approaches to estimating the various parameters. This section discusses the methods used to find the geometric and aerodynamics properties of the quad-rotor developed in this work.

6.4.1 Inertia Calculations

The identification of the inertial parameters is divided into two parts.

- Body moment of inertia.
- Rotational moment of inertia.

The body moments of inertia (I_{XX}, I_{YY} and I_{ZZ}) were identified using CAD software. Specifically, the Solidworks modeling software was used to design the frame and assemble the components as well as calculate the body moment of inertia excluding the rotational parts (motor and propeller). The rotational moment of inertia of the motor and propeller are defined below. Appendix C provides additional details on calculating the moments of inertia which is done by modeling the complex structure of the quad-rotor body as several components. The values identified from the CAD software are:

Moment of inertia about x-axis, $I_{XX} = 0.00866\ Nms^2$

Moment of inertia about y-axis, $I_{YY} = 0.00866\ Nms^2$

Moment of inertia about z-axis, $I_{ZZ} = 0.01653\ Nms^2$

The total rotational moment of inertia about the motor axis, I_r $[Nms^2]$ consists of two components: the rotational moment of inertia of the motor about the axis of rotation, I_m $[Nms^2]$ and the rotational moment of inertia of the propeller, I_p $[Nms^2]$. In order to find these values the motor was modeled as a cylinder and the propeller as a flat plate. Their moments of inertia are equal to (from Appendix C):

$$I_m = \frac{1}{2} M_m R_m^2 = 2.67 \times 10^{-5}\ [Nms^2] \tag{6.1}$$

$$I_p = \frac{1}{12} M_p (W_p^2 + L_p^2) = 9.67 \times 10^{-7}\ [Nms^2] \tag{6.2}$$

$$I_r = I_m + I_p = 28.634 \times 10^{-6}\ [Nms^2] \tag{6.3}$$

To make this chapter more readable, the symbols used in these equations as well as following equations are not reported in this chapter, but defined in their respective Appendices.

6.4.2 Aerodynamics Calculations

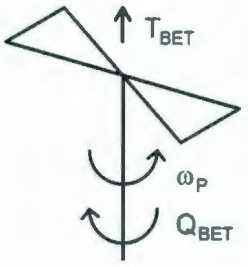

Figure 6.9: Aerodynamic Thrust and Torque

The aerodynamics calculations consist of identifying two parameters; the thrust factor b $[Ns^2]$ and the drag factor d $[N\ s^2]$. Both of these factors have been identified using the dynamometer described in Chapter 4; however, an analytical verification of one of the factors (thrust factor, b) is provided below to validate the value determined experimentally using the dynamometer (b_{EXP}). Verification of one of the factors is sufficinet to justify the experimental value. The analytical validation is based on blade element theory (b_{BET}). The blade element theory is discussed in Appendix D. Figure 6.9 illustrates the thrust, T_{BET} $[N]$, and drag torque, Q_{BET} $[Nm]$, components acting on a propeller. ω_p $[rad\ s^{-1}]$ is the angular speed of the propeller.

To estimate b_{BET} it is necessary to describe the thrust T_{BET} as a function of ω_p. Equation 6.4 shows the relation:

$$T_{BET} = N_B \, \rho_A \, a \, c \, \omega_p^2 \, R_p^3 \, (\frac{\theta_{Io}}{6} - \frac{\theta_{I,tw}}{8} - \frac{\lambda}{4}) \tag{6.4}$$

Since T_{BET} is proportional to the square of the angular speed of the propeller ω_p, it is possible to determine the ratio of T_{BET} to ω_p^2, which is the definition of thrust factor. The numeric result is provided in Equation 6.5.

$$\begin{aligned} b_{BET} &= \frac{T_{BET}}{\omega_p^2} = N_B \, \rho_A \, a \, c \, R_p^3 \, (\frac{\theta_{Io}}{6} - \frac{\theta_{I,tw}}{8} - \frac{\lambda}{4}) \\ &= 2 \times 1.2 \times 2\pi \times 0.026 \times 0.127^3 (\frac{0.349}{6} - \frac{0.1511}{8} - \frac{0.08542}{4}) \\ &= 1.44 \times 10^{-5} [Ns^2] \end{aligned} \tag{6.5}$$

Similarly, to estimate the drag factor d, it is necessary to describe the torque acting on the shaft Q_{BET} as a function of angular speed ω_p. Equation 6.6 shows the relationship.

$$Q_{BET} = N_B \, \rho_A \, c \, \omega_p^2 \, R_p^4 \, (\frac{C_D}{8} + a\lambda \, (\frac{\theta_{Io}}{6} - \frac{\theta_{I,tw}}{8} - \frac{\lambda}{4})) \tag{6.6}$$

As for the thrust T_{BET}, the torque Q_{BET} is proportional to the square of the angular speed of the propeller ω_p. The ratio of Q_{BET} and ω_p^2 is the drag factor d. The numeric result is given in equation 6.7.

$$d_{BET} = \frac{Q_{BET}}{\omega_p^2} = N_B \rho_A c \omega_p^2 R_p^4 (\frac{C_D}{8} + a\lambda (\frac{\theta_{Io}}{6} - \frac{\theta_{I,tw}}{8} - \frac{\lambda}{4}))$$
$$= 2 \times 1.2 \times 0.026 \times 0.127^4 (\frac{0.05}{8} + 2\pi \times 0.08542 (\frac{0.349}{6} - \frac{0.1511}{8} - \frac{0.08542}{4}))$$
$$= 2.576 \times 10^{-7} [Ns^2] \tag{6.7}$$

Unlike the parameter b, the drag factor d is shown with only blade element theory, hence no subscript was applied. The value of b determined experimentally is shown and is denoted by b_{EXP} . The idea is to get the relationship between the propeller angular speed and the thrust produced by the propeller. This was done by characterizing the propellers used in the quad-rotor with the dynamometer. The data are provided in table 6.1.

Table 6.1: APC 10 x 4.7 Propeller Characteristics Data

PWM Pulse Width $[ms]$	RPM	ω_p $[rads^{-1}]$	ω_p^2 $[rad^2s^{-2}]$	Thrust, T_{EXP}[N]
1.004	0	0	0	0
1.068	1150	120.428	14502.9	0.16677
1.12	1925	201.586	40636.92	0.4905
1.18	2550	267.036	71308.23	0.93195
1.236	3000	314.16	98696.51	1.3734
1.296	3500	366.52	134336.9	1.89333
1.352	3900	408.408	166797.1	2.30535
1.412	4175	437.206	191149.1	2.76642
1.468	4475	468.622	219606.6	3.19806
1.528	4825	505.274	255301.8	3.61989
1.584	5280	552.9216	305722.3	4.37526

Figure 6.10 shows the experimental data as well as the linearized model. The slope of the linear approximation between the lift and the speed squared yields, $b_{EXP} =$

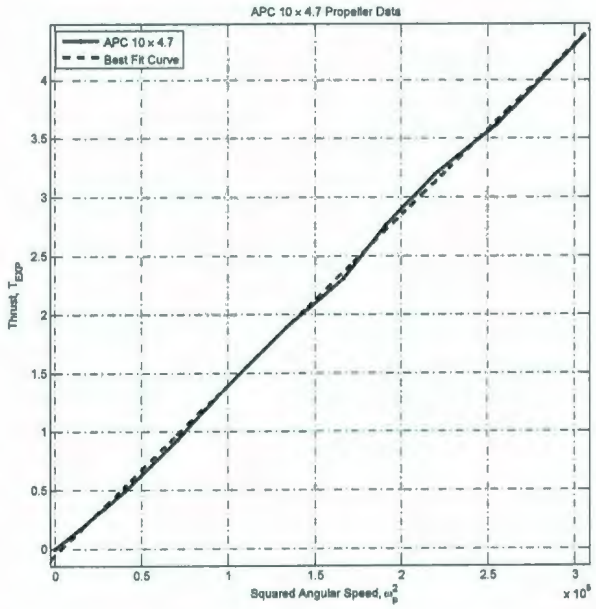

Figure 6.10: Lift vs. Speed Squared

$1.451 \times 10 - 5$ which is fairly close to b_{BET}. Thus we can say, $b_{EXP} \approx b_{BET} = 1.45 \times 10^{-5}[Ns^2]$.

6.5 Test Bench and Sensor Fusion

The initial test bench was designed to stabilize roll and pitch of the quad-rotor using PD control. Once these two states are controlled the quad-rotor is safe to start testing and stabilizing other degrees of freedom by tuning the gains of the controller. The test bench used for this purpose is a basic structure which gives it freedom in rotation about a single axis. Figure 6.11 shows the test bench.

In order to remove the bias caused by integration of gyroscope data as well as to remove the high noise of the sensors, a Kalman filter was introduced for estimating the tilt angle from the gyroscope and accelerometer readings as well as estimating the

Figure 6.11: Test Bench Used to Tune Roll and Pitch

yaw angle from gyroscope and magnetometer reading. The measurement of gyroscope data has been integrated over time in order to measure tilt angles. Due to gradual accumulation of small errors, drift occurs in the reading. On the other hand tilt angles can be measured by recording the acceleration due to gravity and yaw can be measured using the magnetometer which can be considered accurate but very slow in terms of dynamic response. These three sensors were fused using a Kalman Filter where the gyroscope data is taken as the first input and the output of the accelerometer and magnetometer as the second input which is used to estimate error and recalculate bias for removing the drift. Figure 6.12 shows a block diagram of how the Kalman Filter has been implemented to stabilize the quad-rotor. Figure 6.13 shows the filter in action.

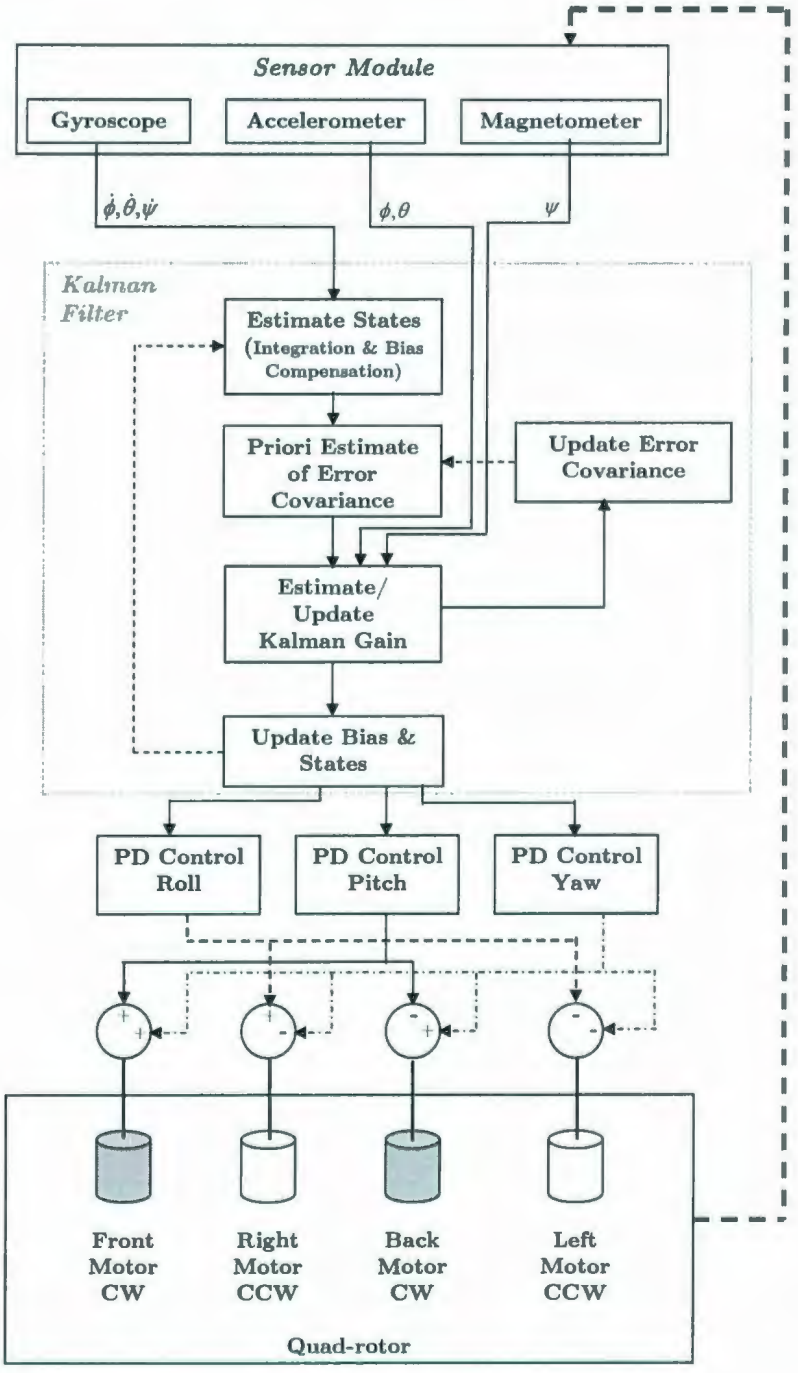

Figure 6.12: Block Diagram of Kalman Filter Based Stabilization of Quad-rotor

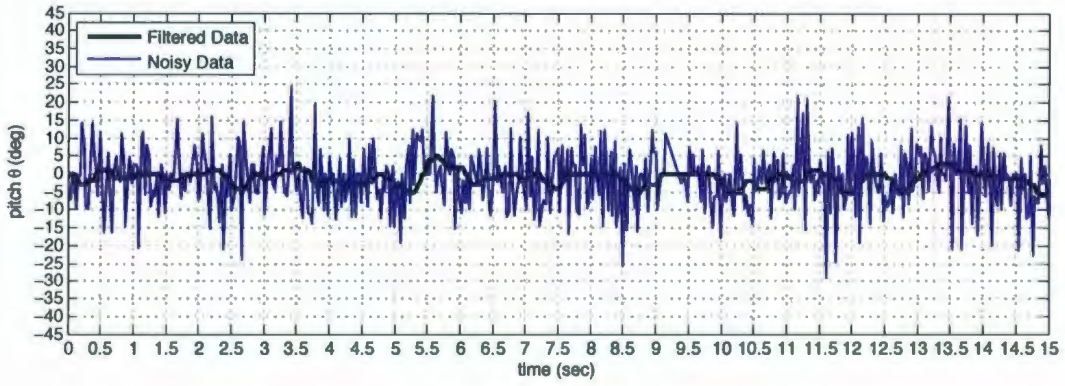

Figure 6.13: Performance of Kalman Filter

6.6 Stabilization Results

Among the six degrees of freedom of the vehicle the most important two are roll, pitch and altitude. Control of these two attitudes and the altitude makes the vehicle hover in the air. In other words, instabilities in roll and pitch makes flying impossible, whereas unstable yaw will degrade stability but is not as critical to flight. Due to this, the test bench mentioned above was designed to provide freedom only in one degree of freedom, keeping the others fixed. Using the test bench the quadrotor controller gains were tuned and evaluated for stable roll and pitch. A proportional value of 0.7 and a derivative value of 0.96 were found to offer satisfactory control of roll and pitch. Figure 6.14 shows the response of roll motion in stable flight test and Figure 6.15 shows its corresponding error. Figure 6.16 shows the robustness of the controller as the quad-rotor recovers from an external disturbance. At approximately 16 seconds, a positive roll disturbance was produced by displacing one of the motors and recording the recovery. Again at 27 seconds a negative pitch disturbance was produced by pulling the motor.

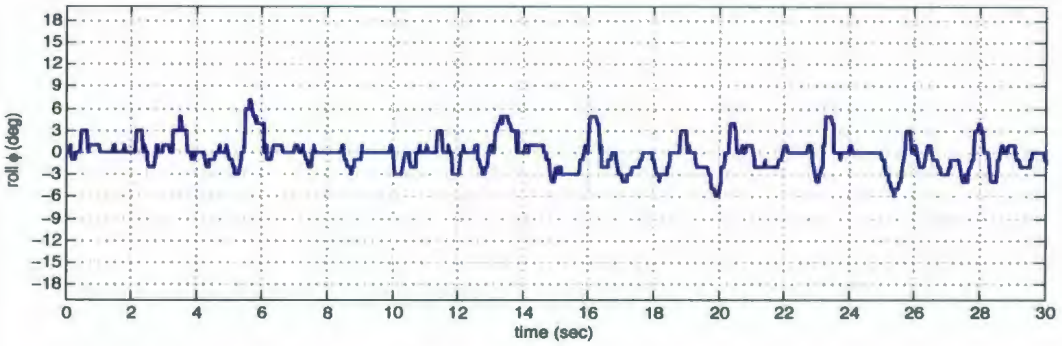

Figure 6.14: Roll Controller Performance

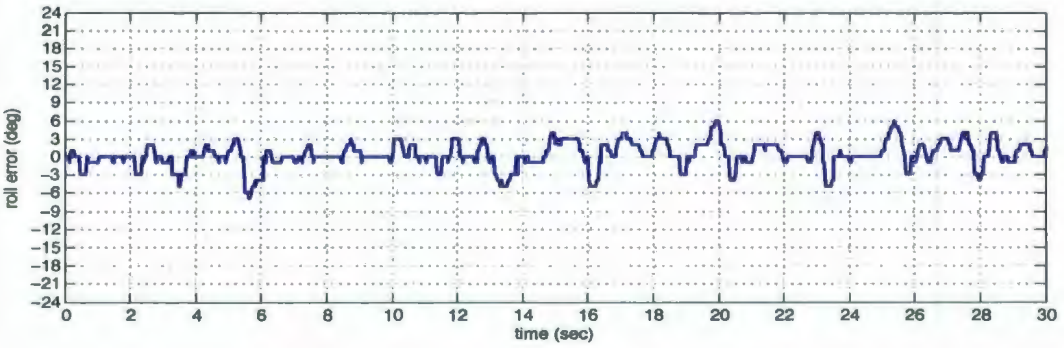

Figure 6.15: Error in Roll Control

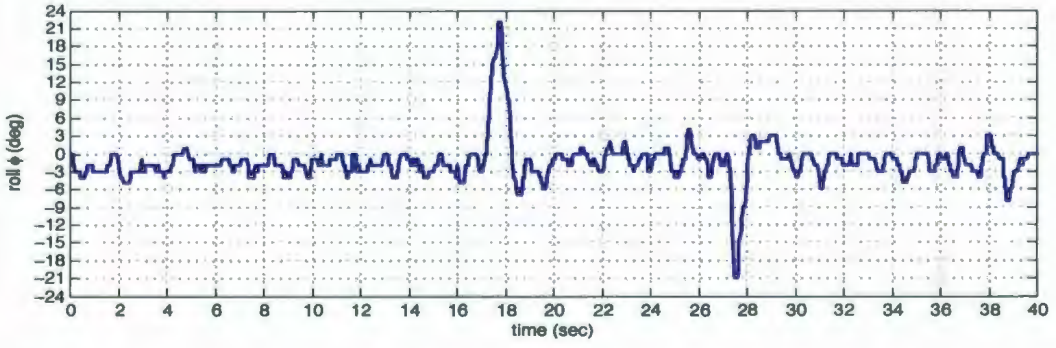

Figure 6.16: Performance of Roll Controller Against Artificial Disturbances

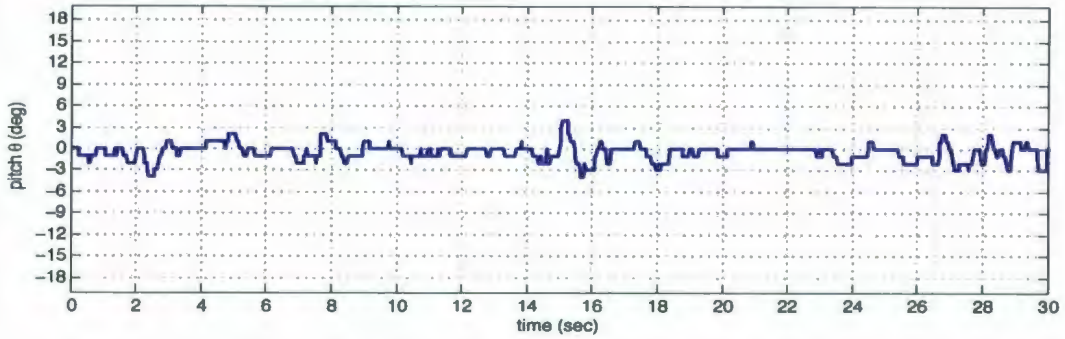

Figure 6.17: Pitch Controller Performance

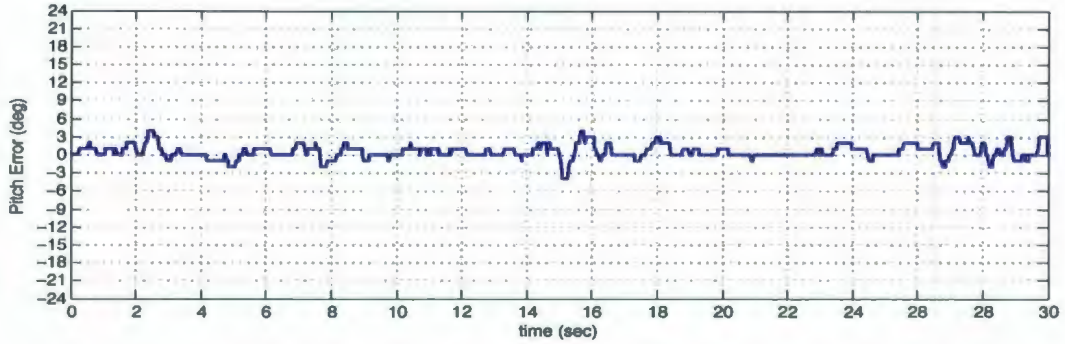

Figure 6.18: Error in Pitch control

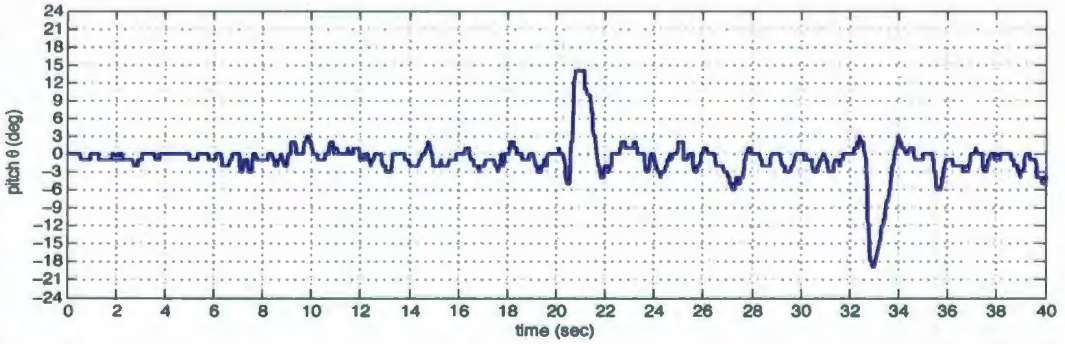

Figure 6.19: Performance of Pitch Controller Against Artificial Disturbances

The yaw, altitude and position controllers have not yet been tested using inertial sensors, due to the lack of time as well as the plan to implement visual servoing. However, inertial sensors will always be included for redundancy.

Chapter 7

Conclusion

This chapter is divided into a review of the main contributions of this thesis, followed by an outlook on future work which takes a more detailed perspective on miniature aerial robots. It tries to identify possible future steps towards intelligent miniature flying robots.

7.1 Review

This thesis focused on the development and control of an autonomous quad-rotor helicopter including the formulation of a detailed dynamic model and methods for the identification of the system parameters. An accurate tool was developed to measure the aerodynamic characteristics of the propeller which yielded parameters required for increasing the accuracy of the model. A vision based control technique has been proposed for the vehicle which is particularly important for critical near-hover conditions (landing/take-off). Finally, a test platform has been developed and primary control has been obtained. A general conclusion is drawn below for every major step

that has been undertaken in this work.

7.1.1 Modeling

The entire dynamic model was formulated based on basic physical and aerodynamic equations. The result is a set of equations describing vehicle dynamics not only in hover but also in motion. The initial model which focused only on the hovering condition was proposed using the bond graph modeling technique described in Chapter 3. A PID controller was implemented in this case for stabilizing in roll, pitch, yaw and altitude. The work has been published in the "*9th International Conference on Bond Graph Modeling and Simulation*" (April 2010) and was very well received by the reviewers. It received an award for the best paper of the conference for its originality and significance to bond graph modeling. Later the model was extended in Matlab with the inclusion of position control in order to implement the proposed vision based pose estimation technique discussed in Chapter 5.

7.1.2 Tool for Aerodynamics Parameter Identification

In keeping with the goals of the project, both the modeling and simulation were very detailed. This could not be achieved without the accurate identification of the system parameters due to the fact that accurate parameters increase the accuracy of the simulation. In this work we proposed a tool for measuring the aerodynamic characteristics of propellers with a special emphasis on small unmanned aircraft propellers. This work is described in Chapter 4. The mechanical structure designed decouples the forces and torque produced by propeller and thus helps measure the

aerodynamic contributions of the propeller. The work has been published in the "*23rd Canadian Conference on Electrical and Computer Engineering*" (May 2010) and was well received by the reviewers.

7.1.3 Platform Development

In order to validate the methods proposed in this work, a quad-rotor platform was developed. The challenge that was encountered in the development of the platform was mainly achieving maximum payload from the vehicle by designing the frame as light as possible and selecting efficient, light weight motors along with other electronic devices. In order to address this problem, the structure was designed using a combination of carbon fiber (arms), and lightweight ABS based components that were manufactured by rapid prototyping. The physical parameters of the structure were obtained from the CAD model. The sensors and the controller board used in this study were commercially available light weight inertial sensors and a single board computer. The programming language for development of the control algorithm was C++.

7.1.4 Control

The two control strategies presented in this thesis were based on feedback control techniques. The control strategy presented in Chapter 3 achieved a stable flight with a generic feedback from any inertial sensor using a PID controller, while the control strategy in Chapter 5 demonstrated stabilization based on a vision based sensor augmented with a PD controller; however, on the experimental platform the

PD controller was implemented using inertial sensors only. A number of difficulties were encountered in implementing PD controller on the real platform including sensor noise, drift due to integration of gyroscope readings, and above all robustness against disturbances and vibrations. These problems were overcome by implementing a Kalman filter. The implementation of the controller on the real platform began with the control of the two main degrees of freedom, namely roll and pitch, which are primarily responsible for stable flight. Results are presented in Chapter 6. Other tests have not yet been performed as the test bench designed for the vehicle only permits testing of roll and pitch. The work is under way to implement the vision based controller proposed in this work (Chapter 5) and it is expected that the results will be submitted for publication at the "*IEEE International Conference on Mechatronics, 2011*".

7.2 Outlook

Untethered testing of the quad-rotor using the vision based algorithm proposed in this work is the foremost concern and is under way. This approach involves a landmark (landing pad) consisting of five LEDs placed on the floor which will be constantly tracked by the onboard Position Sensitive Detector (PSD) equipped with a lens. The position of those five unique points projected on the PSD through the lens will be used as the input to the estimation technique in order to get the pose estimation of the vehicle and thus the accurate takeoff and landing of the vehicle. As a future improvement of the model, the aerodynamics at low Reynolds number needed to be taken into consideration as flight at low Reynolds number has the effect of flow

separation and ultimately unstable aerodynamics. For improving the safety of the platform the addition of carbon rod around the platform can be a promising solution which may serve as a protective barrier. On the other hand, the demands for higher capacity batteries will never cease, and miniaturized fuel-cells are a promising technology. Finally, the system level integration is the key to bringing together all these technologies in the optimal manner. Nevertheless, the goals achieved with this work represent a promising beginning towards a full automatic quad-rotor helicopter.

Bibliography

[1] M. Koeda, Y. Matsumoto, and T. Ogasawara, "Development of an immersive tele-operating system for unmanned helicopter," in *proc. 11th IEEE International Workshop on Robot and Human Interactive Communication*, 2002, pp. 47–52.

[2] J. G. Leishman, *Principles of Helicopter Aerodynamics*, 1st ed. Cambridge University Press, 2000.

[3] C. Eck, "Navigation algorithms with applications to unmanned helicopters," Ph.D. dissertation, ETH Zurich, 2001.

[4] F. Archer, A. Shutko, T. Coleman, A. Haldin, E. Novichikhin, and I. Sidorov, "Introduction, overview, and status of the microwave autonomous copter system (macs)," in *proc of IEEE International Conference on Geoscience and Remote Sensing Symposium*, vol. 5, September 2004, pp. 3574 – 3576.

[5] R. Sugiura, T. Fukagawa, N. Noguchi, K. Ishii, Y. Shibata, and K. Toriyama, "Field information system using an agricultural helicopter towards precision farming," in *Proceddings of IEEE/ASME International Conference on Advanced Intelligent Mechatronics*, vol. 2, July 2003, pp. 1073 – 1078.

[6] S. Rock, E. Frew, H. Jones, E. LeMaster, and B. Woodley, "Combined CDGPS and vision-based control of a small autonomous helicopter," in *Proceedings of the American Control Conference*, vol. 2, June 1998, pp. 694 – 698.

[7] L. Jun, X. Shaorong, G. Zhenbang, and R. Jinjun, "Subminiature unmanned surveillance aircraft and its ground control station for security," 2005 IEEE International Workshop in Safety, Security and Rescue Robotics, pp. 116 – 119, June 2005.

[8] "Rctoys." [Online]. Available: http://www.rctoys.com

[9] "Microdrones." [Online]. Available: http://www.microdrones.com

[10] "Silverlit." [Online]. Available: http://www.silverlit.com

[11] L. Beji, K. M. Zemalache, and H. Marref, "Control of an under-actuated system: Application to a four rotors rotorcraft," in *Proceedings of IEEE International Conference on Robotics and Biomimetics*, 2005, pp. 404 – 409.

[12] A. Abichou, L. Beji, and K. M. Zemalache, "Smooth control of an X4 bidirectional rotors flying robot," 5th International Workshop on Robot Motion and Control, 2005.

[13] G. Fay, "Derivation of the aerodynamic forces for the mesicopter simulation," Stanford University, Tech. Rep., 2001.

[14] P. McKerrow, "Modelling the drganflyer four-rotor helicopter," in *Proceedings of The IEEE International Conference on Robotics and Automation*, vol. 4, 2004, pp. 2596 – 3601.

[15] M. Achtelik, K. M. Doth, G. Hirzinger, D. Gurdan, J. Stumpf, and D. Rus, "Energy-efficient autonomous four-rotor flying robot controlled at 1 khz," in *Proc. of The IEEE International Conference on Robotics and Automation*, 2007, pp. 361 – 366.

[16] S. Bouabdallah, A. Noth, and R. Siegwart, "PID vs. LQ control techniques applied to an indoor micro quadrotor," in *Proc. of The IEEE/RSJ International Conference on Intelligent Robots and Systems*, vol. 3, September 2004, pp. 2451 – 2456.

[17] P. Castillo, A. Dzul, and R. Lozano, "Real-time stabilization and tracking of a four-rotor mini rotorcraft," *IEEE Transactions in Control Systems Technology*, vol. 4, pp. 510 – 516, July 2004.

[18] P. Pounds, R. Mahony, P. Hynes, and J. Roberts, "Design of a four-rotor aerial robot," in *Proc. of Australian Conference on Robotics and Automation*, Auckland, New Zealand, 2002.

[19] P. Pounds, Mahony, and J. Gresham, "Towards dynamically-favourable quadrotor aerial robots," in *Proc. of Australasian Conference on Robotics and Automation*, Auckland, New Zealand, 2004.

[20] G. Hoffmann, H. Huang, S. Waslander, and C. Tomlin, "Quadrotor helicopter flight dynamics and control: Theory and experiment," in *Proceedings of the AIAA Guidance, Navigation, and Control Conference*, 2007.

[21] Tayebi and McGilvray, "Attitude stabilization of a four-rotor aerial robot," in *Proc. of 43rd IEEE Conference on Decision and Control*, 2004, p. 1216 1221.

[22] A. Tayebi and S. McGilvray, "Attitude stabilization of a VTOL quadrotor aircraft," *IEEE Transaction on Control System Technology*, vol. 14, no. 3, p. 562 571, May 2006.

[23] P. Murrieri, S. Bouabdallah, and R. Siegwart, "Design and control of an indoor micro quadrotor," in *Proc. of The International Conference on Robotics and Automation*, 2004.

[24] R. Lozano, P. Castillo, and A. Dzul, "Stabilization of a mini rotorcraft having four rotors," in *Proceedings of 2004 IEEE/RSJ International Conference on Intelligent Robots and Systems*, 2004, p. 2693 2698.

[25] A. Palomino, S. Salazar-Cruz, and R. Lozano, "Trajectory tracking for a four rotor mini-aircraft," in *Proceedings of the 44th IEEE Conference on Decision and control, and the European Control Conference*, 2005, p. 2505 2510.

[26] T. Madani and A. Benallegue, "Backstepping control for a quadrotor helicopter," in *Proceedings of 2006 IEEE/RSJ International Conference on IntelligentRobots and Systems*, 2006, p. 3255 3260.

[27] ——, "Backstepping sliding mode control applied to a miniature quad-rotor flying robot," in *Proc. of The 32nd Annual Conference of the IEEE Industrial Electronics Society*, 2006, p. 700 705.

[28] ——, "Control of a quadrotor mini-helicopter via full state backstepping technique," in *Proceedings of the 45th IEEE Conference on Decision and Control*, 2006, pp. 1515 – 1520.

[29] A. Mokhtari and A. Benallegue, "Dynamic feedback controller of euler angles and wind parameters estimation for a quadrotor unmanned aerial vehicle," in *Proceedings of the 2004 IEEE International Conference on Robotics and Automation*, 2004, p. 2359 2366.

[30] A. Benallegue, V. Mister, and N. K. MSirdi, "Exact linearization and noninteracting control of a 4 rotors helicopter via dynamic feedback," IEEE International Workshop on Robot and Human Interactive Communication, 2001.

[31] A. Fradkov, B. Andrievsky, and D. Peaucelle, "Adaptive control experiments for laas helicopter benchmark," in *Proc. of the International Conference PhysCon 2005*, 2005, p. 760 765.

[32] Y. Morel and A. Leonessa, "Direct adaptive tracking control of quadrotor aerial vehicles," in *Proc of the Florida Conference on Recent Advances in Robotics*, 2006, pp. 1 – 6.

[33] R. Lozano, P. Castillo, and A. Dzul, "Stabilization of a mini rotorcraft with four rotors," IEEE Control Systems Magazine, 2005.

[34] T. Hamel, N. Guenard, and R. Mahony, "A practical visual servo control for an unmanned aerial vehicle," in *Proc. of the IEEE International Conference on Robotics and Automation*, 2007, p. 1342 1348.

[35] M. Valenti, G. P. Tournier, and J. P. How, "Estimation and control of a quadrotor vehicle using monocular vision and moire patterns," in *AIAA Guidance, Navigation, and Control Conference and Exhibit*, 2006.

[36] T. Hamel, N. Metni, and F. Derkx, "Visual tracking control of aerial robotic systems with adaptive depth estimation," in *Proc. of the 44th IEEE Conference on Decision and Control, and the European Control Conference*, 2005, p. 6078 6084.

[37] J. P. Ostrowski, E. Altug, and C. J. Taylor, "Quadrotor control using dual camera visual feedback," in *Proc. of the 2003 IEEE International Conference on Robotics and Automation*, 2003, p. 4294 4299.

[38] M. G. Earl and R. DAndrea, "Real-time attitude estimation techniques applied to a four rotor helicopter," in *Proc. of the 43rd IEEE Conference on Decision and Control*, 2004, p. 3956 3961.

[39] M. Tarbouchi, J. Dunfied, and G. Labonte, "Neural network based control of a four rotor helicopter," in *Proc. of the IEEE International Conference on Industrial Technology*, 2004, p. 1543 1548.

[40] C. Coza and C. Macnab, "A new robust adaptive-fuzzy control method applied to quadrotor helicopter stabilization," in *Annual Meeting of the North American Fuzzy Information Processing Society*, 2006, pp. 475 – 479.

[41] P. Pounds, R. Mahony, and P. Corke, "Modelling and control of a quad-rotor robot," in *Proc. of the Australasian Conference on Robotics and Automation*, Canberra, ACT, Australia, 2006.

[42] S. Hanford and H. Long, L., "A semi-autonomous quad-rotor micro air vehicle," in *AIAA InfoTechAerospace Conference*, Washington, DC, 2005.

[43] S. Bouabdallah and R. Siegwart, "Towards intelligent miniature flying robots," in *In Proceedings of Field and Service Robotics*, Port Douglas, Australia, 2005.

[44] H. Poonawala, K. Krishnanand, and D. Ghose, "Design of a quadrotor micro air vehicle," in *Proc. of the Conference on Advances in Space Science and Technology*, 2007.

[45] S. L. Waslander, G. M. Homann, J. S. Jang, and C. J. Tomlin, "Multi-agent quadrotor testbed control design: Integral sliding mode vs. reinforcement learning," in *Proceedings of the IEEE/RSJ International Conference on Intelligent Robots and Systems*, Edmonton, AB, Canada, August 2005, pp. 468 – 473.

[46] D. Lee, T. C. Burg, B. Xian, and D. M. Dawson, "Output feedback tracking control of an under actuated quad-rotor UAV," in *American Control Conference*, July 2007, pp. 1775 – 178.

[47] B. Erginer and E. Altug, "Modeling and PD control of a quadrotor VTOL vehicle," in *IEEE Intelligent Vehicles Symposium*, June 2007, pp. 894 – 899.

[48] G. Homann, D. G. Rajnarayan, S. L.Waslander, D. Dostal, J. S. Jang, and C. J. Tomlin, "The stanford testbed of autonomous rotorcraft for multi-agent control (STARMAC)," in *Proceedings of the 23rd Digital Avionics Systems Conference*, Salt Lake City, UT, November 2004, pp. 12.E.4/1 – 10.

[49] J. Roberts, T. Stirling, and J. Zufferey, "Quadrotor using minimal sensing for autonomous indoor flight," in *3rd US-European Competition and Workshop on Micro Air Vehicle Systems (MAV07) & European Micro Air Vehicle Conference and Flight Competition (EMAV)*, Toulouse, France, 2007.

[50] "Aerospaceweb." [Online]. Available: http://www.aerospaceweb.org

Appendix A

Quad-rotor Kinematics and Dynamics

This appendix begins with the general equations that identify the 6 DoF of a rigid body. The Newton-Euler formulation has been adopted for this work. Later the general kinematics and dynamics has been implemented to derive quad-rotor dynamics equations.

A.1 Kinematics

Kinematics is a branch of mechanics which studies the motion of a body or a system of bodies without consideration of the forces and torques acting on it. To describe the motion of a 6 DoF rigid body it is usual to define two reference frames:

- Earth inertial reference (E-frame)
- Body fixed reference (O-frame)

The E-frame (E, X, Y, Z) is chosen as the inertial right-hand reference. X points towards the North, Y points towards the West, Z points upwards respect to the earth and E is the axis origin. This frame is used to define the linear position (Γ^e $[m]$) and the angular position ($\boldsymbol{\Theta^e}$ $[rad]$) of the quad-rotor.

The O-frame (O, x, y, z) is attached to the body. x points towards the quad-rotor front, y points towards the quad-rotor left, z points upwards and O is the axis origin. O is chosen to coincide with the center of the quad-rotor cross structure. This reference is right-hand too. The linear velocity ($\boldsymbol{v^b}$ $[ms^{-1}]$), the angular velocity ($\boldsymbol{\omega^b}$ $[rads^{-1}]$), the forces ($\boldsymbol{F^b}$ $[N]$) and the moments ($\boldsymbol{M^b}$ $[Nm]$) are defined in this frame.

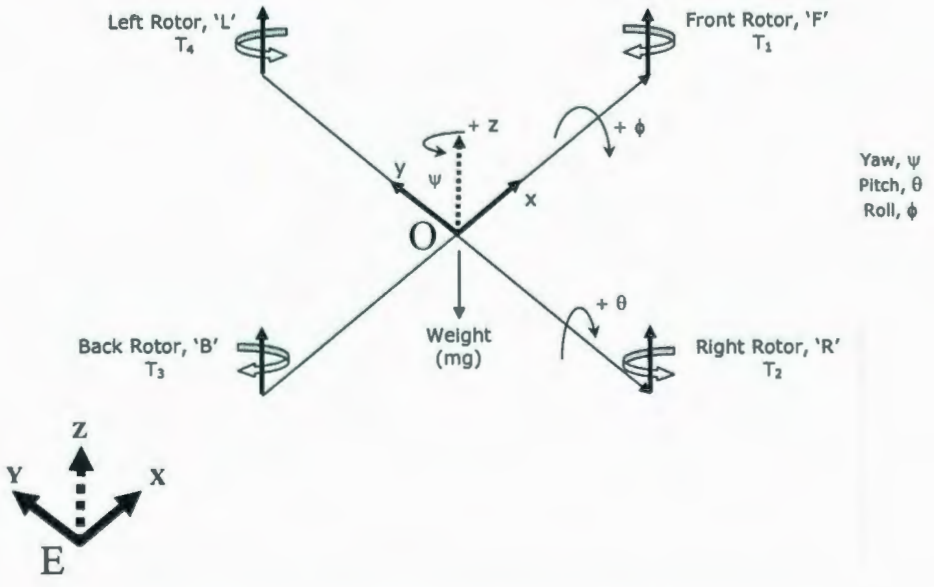

Figure A.1: Co-ordinate System for Modeling

The linear position $\boldsymbol{\Gamma^e}$ of the helicopter is determined by the coordinates of the vector distances between the origin of the O-frame and the origin of the E-frame respect to the E-frame according to equation (A.1). Figure A.1 shows the coordinate

frames.

$$\mathbf{\Gamma}^{e} = \begin{bmatrix} X & Y & Z \end{bmatrix}^{T} \tag{A.1}$$

The angular position (or attitude) Θ^{e} of the helicopter is defined by the orientation of the O-frame with respect to the E-frame. This is given by three consecutive rotations about the main axes which take the E-frame into the O-frame. In this work the "roll-pitch-yaw" set of Euler angles were used. Equation (A.2) shows the attitude vector.

$$\mathbf{\Theta}^{e} = \begin{bmatrix} \phi & \theta & \psi \end{bmatrix}^{T} \tag{A.2}$$

The rotation matrix $\boldsymbol{R}$ is obtained by post-multiplying the three basic rotation matrices in the following order:

- Rotation about the Z_E axis of the angle ψ (yaw) through $\boldsymbol{R}(\psi, z)$

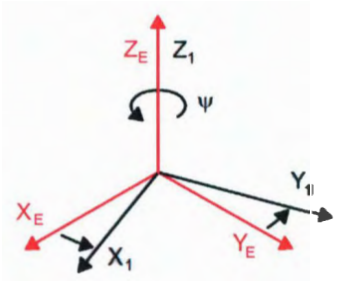

$$\boldsymbol{R}(\psi, z) = \begin{bmatrix} \cos\psi & -\sin\psi & 0 \\ \sin\psi & \cos\psi & 0 \\ 0 & 0 & 1 \end{bmatrix} \tag{A.3}$$

- Rotation about the Y_1 axis of the angle θ (pitch) through $\boldsymbol{R}(\theta, y)$

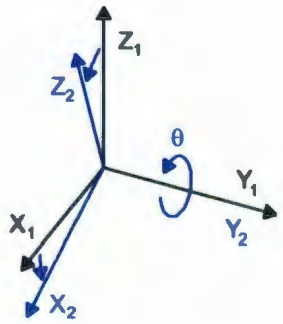

$$\boldsymbol{R}(\theta, y) = \begin{bmatrix} \cos\theta & 0 & \sin\theta \\ 0 & 1 & 0 \\ -\sin\theta & 0 & \cos\theta \end{bmatrix} \tag{A.4}$$

- Rotation about the X_2 axis of the angle ϕ (roll) through $\boldsymbol{R}(\phi, x)$

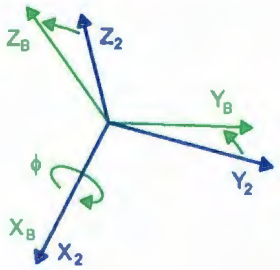

$$\boldsymbol{R}(\phi, x) = \begin{bmatrix} 1 & 0 & 0 \\ 0 & \cos\phi & -\sin\phi \\ 0 & \sin\phi & \cos\phi \end{bmatrix} \tag{A.5}$$

Equation (A.6) shows the composition of the rotation matrix $\boldsymbol{R}$.

$$\begin{aligned} \boldsymbol{R} &= \boldsymbol{R}(\psi, z)\boldsymbol{R}(\theta, y)\boldsymbol{R}(\phi, x) \\ &= \begin{bmatrix} \cos\theta\cos\psi & -\cos\phi\sin\psi + \sin\phi\sin\theta\cos\psi & \sin\phi\sin\psi + \cos\phi\sin\theta\cos\psi \\ \cos\theta\sin\psi & \cos\phi\cos\psi + \sin\phi\sin\theta\sin\psi & -\sin\phi\cos\psi + \cos\phi\sin\theta\sin\psi \\ -\sin\theta & \sin\phi\cos\theta & \cos\phi\cos\theta \end{bmatrix} \end{aligned} \tag{A.6}$$

As stated before, the linear $\boldsymbol{v^b}$ and the angular $\boldsymbol{\omega^b}$ velocities are expressed in the body-fixed frame. Their compositions are defined according to equations (A.7) and (A.8).

$$\boldsymbol{v^b} = \begin{bmatrix} v_x & v_y & v_z \end{bmatrix}^T \tag{A.7}$$

$$\boldsymbol{\omega^b} = \begin{bmatrix} \omega_x & \omega_y & \omega_z \end{bmatrix}^T \tag{A.8}$$

It is possible to combine linear and angular quantities to give a complete representation of the body in the space. Two vectors, can be thus defined: the generalized position $\boldsymbol{\xi}$ and the generalized velocity $\boldsymbol{\nu}$, as reported in equations (A.9) and (A.10).

$$\boldsymbol{\xi} = \begin{bmatrix} \boldsymbol{\Gamma^e} & \boldsymbol{\Theta^e} \end{bmatrix}^T = \begin{bmatrix} X & Y & Z & \phi & \theta & \psi \end{bmatrix}^T \tag{A.9}$$

$$\boldsymbol{\nu} = \begin{bmatrix} \boldsymbol{v^b} & \boldsymbol{\omega^b} \end{bmatrix}^T = \begin{bmatrix} v_x & v_y & v_z & \omega_x & \omega_y & \omega_z \end{bmatrix}^T \tag{A.10}$$

The relation between the linear velocity in the body-fixed frame $\boldsymbol{v^b}$ and that one in the earth frame $\dot{\boldsymbol{\Gamma}}^{\boldsymbol{e}}$ $[m\ s^{-1}]$ involves the rotation matrix $\boldsymbol{R}$ according to equation (A.11).

$$\dot{\boldsymbol{\Gamma}}^{\boldsymbol{e}} = \boldsymbol{R}\,\boldsymbol{v^b} \tag{A.11}$$

As for the linear velocity, it is also possible to relate the angular velocity in the earth frame (or Euler rates) $\dot{\boldsymbol{\Theta}}^{\boldsymbol{e}}$ $[rad\ s^{-1}]$ to that one in the body-fixed frame $\boldsymbol{\omega^b}$. thanks to the transfer matrix $\boldsymbol{T_\Theta}$. Equations (A.12) and (A.13) show the relation specified above.

$$\boldsymbol{\omega}^b = \boldsymbol{T}_{\boldsymbol{\Theta}}^{-1}\, \dot{\boldsymbol{\Theta}}^e \tag{A.12}$$

$$\dot{\boldsymbol{\Theta}}^e = \boldsymbol{T}_{\boldsymbol{\Theta}}\, \boldsymbol{\omega}^b \tag{A.13}$$

The transfer matrix T_Θ can be determined by resolving the Euler rates $\dot{\boldsymbol{\Theta}}^e$ into the body-fixed frame as shown in equations (A.14), (A.15) and (A.16).

$$\begin{bmatrix} \omega_x \\ \omega_y \\ \omega_z \end{bmatrix} = \begin{bmatrix} \dot{\phi} \\ 0 \\ 0 \end{bmatrix} + \boldsymbol{R}(\boldsymbol{\phi}, \boldsymbol{x})^{-1} \begin{bmatrix} 0 \\ \dot{\theta} \\ 0 \end{bmatrix} + \boldsymbol{R}(\boldsymbol{\phi}, \boldsymbol{x})^{-1} \boldsymbol{R}(\boldsymbol{\theta}, \boldsymbol{y})^{-1} \begin{bmatrix} 0 \\ 0 \\ \dot{\psi} \end{bmatrix} = \boldsymbol{T}_{\boldsymbol{\Theta}}^{-1} \begin{bmatrix} \dot{\phi} \\ \dot{\theta} \\ \dot{\psi} \end{bmatrix} \tag{A.14}$$

$$\boldsymbol{T}_{\boldsymbol{\Theta}}^{-1} = \begin{bmatrix} 1 & 0 & -\sin\theta \\ 0 & \cos\phi & \cos\theta \sin\phi \\ 0 & -\sin\phi & \cos\phi \cos\theta \end{bmatrix} \tag{A.15}$$

$$\boldsymbol{T}_{\boldsymbol{\Theta}} = \begin{bmatrix} 1 & \sin\phi \tan\theta & \cos\phi \tan\theta \\ 0 & \cos\phi & -\sin\phi \\ 0 & \frac{-\sin\phi}{\cos\theta} & \frac{\cos\phi}{\cos\theta} \end{bmatrix} \tag{A.16}$$

It is possible to describe equations (A.11) and (A.13) in just one equivalence which relate the derivative of the generalized position in the earth frame $\dot{\boldsymbol{\xi}}$ to the generalized velocity in the body frame $\boldsymbol{\nu}$. The transformation is possible thanks to the generalized matrix $\boldsymbol{J}_{\boldsymbol{\Theta}}$. Equations (A.17) and (A.18) shows the relation described above.

$$\dot{\xi} = J_{\Theta}\nu \tag{A.17}$$

where,

$$J_{\Theta} = \begin{bmatrix} R & 0_{3\times3} \\ 0_{3\times3} & T_{\Theta} \end{bmatrix} \tag{A.18}$$

A.2 Dynamics

Dynamics is a branch of mechanics which studies the effects of forces and moments on the motion of a body or system of bodies. There are several techniques which can be used to derive the equations of a rigid body with 6 DoF. The Newton-Euler formulation has been adopted in this work.

The equations of motion are more conveniently formulated in a body-fixed frame because:

- The inertia matrix is time-invariant.
- Advantage of body symmetry can be taken to simplify the equations.
- Measurements taken on-board are easily converted to body-fixed frame.
- Control forces are almost always given in the body-fixed frame.

The decision to describe the equations of motion in the body-fixed frame trades off complexity in the acceleration terms for relative simplicity in the force terms. Two assumptions have been made in this approach:

- The first one states that the origin of the body-fixed frame O is coincident with the center of mass (CoM) of the body. Otherwise, another point (CoM) should be taken into account which considerably complicates the body equations.

- The second one specifies that the axes of the O-frame coincide with the body principal axes of inertia. In this case the inertia matrix $\boldsymbol{I}$ is diagonal and, once again, the body equations become easier.

From the Eulers first axiom of the Newton's second law follows the derivation of the linear components of the body motion, according to equation (A.19).

$$\begin{aligned} m\,\ddot{\boldsymbol{\Gamma}}^{\boldsymbol{e}} &= \boldsymbol{F}^{\boldsymbol{e}} \\ m\,\dot{\widehat{\boldsymbol{R}\boldsymbol{v}^{\boldsymbol{b}}}} &= \boldsymbol{R}\boldsymbol{F}^{\boldsymbol{b}} \\ m\,(\boldsymbol{R}\dot{\boldsymbol{v}}^{\boldsymbol{b}} + \dot{\boldsymbol{R}}\boldsymbol{v}^{\boldsymbol{b}}) &= \boldsymbol{R}\boldsymbol{F}^{\boldsymbol{b}} \\ m\,\boldsymbol{R}(\dot{\boldsymbol{v}}^{\boldsymbol{b}} + \boldsymbol{\omega}^{\boldsymbol{b}} \times \boldsymbol{v}^{\boldsymbol{b}}) &= \boldsymbol{R}\boldsymbol{F}^{\boldsymbol{b}} \\ m\,(\dot{\boldsymbol{v}}^{\boldsymbol{b}} + \boldsymbol{\omega}^{\boldsymbol{b}} \times \boldsymbol{v}^{\boldsymbol{b}}) &= \boldsymbol{F}^{\boldsymbol{b}} \\ m\,\dot{\boldsymbol{v}}^{\boldsymbol{b}} + \boldsymbol{\omega}^{\boldsymbol{b}} \times m\boldsymbol{v}^{\boldsymbol{b}} &= \boldsymbol{F}^{\boldsymbol{b}} \end{aligned} \tag{A.19}$$

Where $m[kg]$ is the quad-rotor mass, $\ddot{\boldsymbol{\Gamma}}^{\boldsymbol{e}}$ $[ms^{-2}]$ is the quad-rotor linear acceleration vector with respect to E-frame, $\boldsymbol{F}^{\boldsymbol{e}}$ $[N]$ is the quad-rotor forces vector with respect to E-frame, $\dot{\boldsymbol{v}}^{\boldsymbol{b}}$ $[ms^{-2}]$ is the quad-rotor linear acceleration vector with respect to O-frame and $\dot{\boldsymbol{R}}$ is the rotation matrix derivative. Furthermore, the symbol '$\times$' denotes the vector cross product.

Equation (A.20) shows the derivation of the angular components of the body motion from the Eulers second axiom of the Newtons second law.

$$
\begin{aligned}
I\,\ddot{\Theta}^{e} &= M^{e} \\
I\,\widehat{\dot{T}_{\Theta}\omega^{b}} &= T_{\Theta}M^{b} \\
&\vdots \\
I\,(\dot{\omega}^{b} + \omega^{b} \times \omega^{b}) &= M^{b} \\
(I\,\dot{\omega}^{b} + \omega^{b} \times I\,\omega^{b}) &= M^{b}
\end{aligned}
\tag{A.20}
$$

In equation (A.20) $\boldsymbol{I}$ $[N\ m\ s^2]$ is the body inertia matrix (in the body-fixed frame), $\ddot{\Theta}^{e}$ $[rad\ s^{-2}]$ is the quad-rotor angular acceleration vector with respect to E-frame, $\dot{\omega}^{b}$ $[rad\ s^{-2}]$ is the quad-rotor angular acceleration vector with respect to O-frame and $\boldsymbol{M^{e}}$ $[N\ m]$ is the quad-rotor moment vector with respect to E-frame.

By putting together equations (A.19) and (A.20), it is possible to describe the motion of a 6 DOF rigid body. Equation (A.21) shows a matrix formulation of the dynamics with respect to body frame (O frame).

$$
\begin{bmatrix} m\boldsymbol{I_{3\times 3}} & \boldsymbol{0_{3\times 3}} \\ \boldsymbol{0_{3\times 3}} & \boldsymbol{I} \end{bmatrix} \begin{bmatrix} \dot{v}^{b} \\ \dot{\omega}^{b} \end{bmatrix} + \begin{bmatrix} \omega^{b} \times (mv^{b}) \\ \omega^{b} \times (I\omega^{b}) \end{bmatrix} = \begin{bmatrix} \boldsymbol{F^{b}} \\ \boldsymbol{M^{b}} \end{bmatrix} \tag{A.21}
$$

Where the notation $\boldsymbol{I_{3\times 3}}$ means an identity matrix with dimension 3 times 3. In addition, it is easy to see that the first matrix in equation (A.21) is diagonal and constant. Here, $\dot{\boldsymbol{v}}^{b}$ $[m\ s^{-2}]$ is the quad-rotor linear acceleration vector with respect to O-frame while $\dot{\omega}^{b}$ $[rad\ s^{-2}]$ is the quad-rotor angular acceleration vector with respect to O-frame. In addition, $\boldsymbol{F^{b}}$ $[N]$ is the quad-rotor forces vector with respect to O-frame and $\boldsymbol{M^{b}}$ $[N\ m]$ is the quad-rotor moments vector with respect to O-frame.

A generalized force vector $\boldsymbol{\Lambda}$ can be defined according to equation (A.22).

$$\Lambda = \begin{bmatrix} \boldsymbol{F^b} & \boldsymbol{M^b} \end{bmatrix}^T = \begin{bmatrix} F_x & F_y & F_z & M_x & M_y & M_z \end{bmatrix}^T \tag{A.22}$$

Therefore it is possible to rewrite equation (A.21) in a matrix form:

$$\boldsymbol{\Delta_I^b}\,\dot{\boldsymbol{\nu}} + \boldsymbol{\Delta_C^b}(\boldsymbol{\nu})\,\boldsymbol{\nu} = \boldsymbol{\Lambda} \tag{A.23}$$

Where $\dot{\boldsymbol{\nu}}$ is the generalized acceleration vector with respect to O-frame. $\boldsymbol{\Delta_I^b}$ is the system inertia matrix and $\boldsymbol{\Delta_C^b}$ is the Coriolis-centripetal matrix, both with respect to O-frame. Equation (A.24) shows the system inertia matrix.

$$\boldsymbol{\Delta_I^b} = \begin{bmatrix} m\boldsymbol{I_{3\times 3}} & \boldsymbol{0_{3\times 3}} \\ \boldsymbol{0_{3\times 3}} & \boldsymbol{I} \end{bmatrix} = \begin{bmatrix} m & 0 & 0 & 0 & 0 & 0 \\ 0 & m & 0 & 0 & 0 & 0 \\ 0 & 0 & m & 0 & 0 & 0 \\ 0 & 0 & 0 & I_{XX} & 0 & 0 \\ 0 & 0 & 0 & 0 & I_{YY} & 0 \\ 0 & 0 & 0 & 0 & 0 & I_{ZZ} \end{bmatrix} \tag{A.24}$$

It is easy to see that $\boldsymbol{\Delta_I^b}$ is diagonal and constant. Equation (A.25) shows the Coriolis-centripetal matrix.

$$\Delta_C^b = \begin{bmatrix} \mathbf{0_{3\times3}} & -m\,\boldsymbol{S}(\boldsymbol{v}^b) \\ \mathbf{0_{3\times3}} & -\boldsymbol{S}(\boldsymbol{I}\,\boldsymbol{\omega}^b) \end{bmatrix} = \begin{bmatrix} 0 & 0 & 0 & 0 & m\,v_z & -m\,v_y \\ 0 & 0 & 0 & -m\,v_z & 0 & m\,v_x \\ 0 & 0 & 0 & m\,v_y & -m\,v_x & 0 \\ 0 & 0 & 0 & 0 & I_{ZZ}\,\omega_z & -I_{YY}\,\omega_y \\ 0 & 0 & 0 & -I_{ZZ}\,\omega_z & 0 & I_{XX}\,\omega_x \\ 0 & 0 & 0 & I_{YY}\,\omega_y & -I_{XX}\,\omega_x & 0 \end{bmatrix} \tag{A.25}$$

In this equation the skew-symmetric operator $\boldsymbol{S}(\cdot)$ has been adopted. For a generic three dimension vector $\boldsymbol{k}$, the skew-symmetric matrix of $\boldsymbol{S}(\boldsymbol{k})$ is defined according to equation (A.26).

$$\boldsymbol{S}(\boldsymbol{k}) = \text{-}\boldsymbol{S}^T(\boldsymbol{k}) = \begin{bmatrix} 0 & -k_3 & k_2 \\ k_3 & 0 & -k_1 \\ -k_2 & k_1 & 0 \end{bmatrix} \qquad \boldsymbol{k} = \begin{bmatrix} k_1 \\ k_2 \\ k_3 \end{bmatrix} \tag{A.26}$$

Equation (A.23) is totally generic and is valid for all rigid bodies subject to the assumptions (or simplifications) previously made. It is used in this work to model the quad-rotor helicopter, hence the last vector contains specific information about its dynamics. $\boldsymbol{\Lambda}$ can be divided in three components according to the nature of the quad-rotor contributions.

Among the contribution of external forces, the drag due to frictional resistance of the body has not been considered throughout the work. However, it has been

defined in Equation 3.3 of Chapter 3 and been neglected in simulation and further analysis. Thus the first contribution is the gravitational vector $\Delta_g^b(\xi)$ given from the acceleration due to gravity g $[m\,s^{-2}]$. It is easy to understand that it affects just the linear and not the angular equations since it is a force and not a torque/moment. Equation (A.27) shows the transformations to get $\Delta_g^b(\xi)$.

$$\Delta_g^b(\xi) = \begin{bmatrix} F_g^b \\ 0_{3\times1} \end{bmatrix} = \begin{bmatrix} R^{-1}\,F_g^e \\ 0_{3\times1} \end{bmatrix} = \begin{bmatrix} R^T \begin{bmatrix} 0 \\ 0 \\ -m\,g \end{bmatrix} \\ 0_{3\times1} \end{bmatrix} = \begin{bmatrix} m\,g\,\sin\theta \\ -m\,g\,\cos\theta\sin\phi \\ -m\,g\,\cos\theta\cos\phi \\ 0 \\ 0 \\ 0 \end{bmatrix} \quad \text{(A.27)}$$

Where F_g^b $[N]$ is the gravitational force vector with respect to O-frame and F_g^e $[N]$ is that one with respect to E-frame. Furthermore, since R is an orthogonal normalized matrix, its inverted R^{-1} is equal to the transposed one R^T.

The second contribution takes into account the gyroscopic effects produced by the propeller rotation. Since two of them are rotating clockwise and the other two counter-clockwise, there is a overall imbalance when the algebraic sum of the rotor speeds is not equal to zero. If, in addition, the roll or pitch rates are also different than zero, the quad-rotor experiences a gyroscopic torque according to equation (A.28). Let us take a matrix Δ_G^b for gyroscopic effect. Therefore,

$$\Delta_G^b(\nu)\,\Omega = \begin{bmatrix} \mathbf{0_{3\times 1}} \\ -\sum_{k=1}^{4} I_r \left(\boldsymbol{\omega}^b \times \begin{bmatrix} 0 \\ 0 \\ 1 \end{bmatrix} \right) (-1)^k \Omega_k \end{bmatrix}$$

$$= \begin{bmatrix} \mathbf{0_{3\times 1}} \\ I_r \begin{bmatrix} -\omega_y \\ \omega_x \\ 0 \end{bmatrix} \Omega \end{bmatrix} = I_r \begin{bmatrix} 0 & 0 & 0 & 0 \\ 0 & 0 & 0 & 0 \\ 0 & 0 & 0 & 0 \\ \omega_y & -\omega_y & \omega_y & -\omega_y \\ -\omega_x & \omega_x & -\omega_x & \omega_x \\ 0 & 0 & 0 & 0 \end{bmatrix} \boldsymbol{\Omega} \tag{A.28}$$

Here, I_r $[N\ m\ s^2]$ is the total rotational moment of inertia around the propeller axis calculated in Chapter 6. It is easy to see that the gyroscopic effects produced by the propeller rotation are just related to the angular and not the linear equations.

Equation (A.29) defines the overall propeller speed Ω $[rad\ s^{-1}]$ and the propellers speed vector $\boldsymbol{\Omega}$ $[rad\ s^{-1}]$ used in equation (A.28). However, the propeller speed has been denoted in Chapter 3 as ω_i, where i is the i^{th} propeller. The modification has been adopted to reduce confusion between notations.

$$\Omega = -\Omega_1 + \Omega_2 - \Omega_3 + \Omega_4 \qquad \boldsymbol{\Omega} = \begin{bmatrix} \Omega_1 \\ \Omega_2 \\ \Omega_3 \\ \Omega_4 \end{bmatrix} \tag{A.29}$$

Where Ω_1 is the front propeller speed, Ω_2 is the right propeller speed, Ω_3 is the

rear propeller speed and Ω_4 is the left propeller speed.

The third contribution takes into account the forces and moments directly produced by the main maneuvering inputs. From aerodynamics consideration, it follows that both forces and moments are proportional to the squared propellers speed. Therefore the maneuver matrix $\boldsymbol{\Delta_U^b}$ is multiplied by $\boldsymbol{\Omega^2}$ to get the maneuver vector $\boldsymbol{U^b(\Omega)}$. The values for aerodynamic contributions (thrust b $[N\ s^2]$ and drag d $[N\ m\ s^2]$ factors) are calculated in Chapter 6 using information extracted from the dynamometer experiment described in Chapter 4.

Equation (A.30) shows the action of the maneuver vector on the quad-rotor helicopter dynamics.

$$\boldsymbol{U^b(\Omega)} = \boldsymbol{\Delta_U^b}\,\Omega^2 = \begin{bmatrix} 0 \\ 0 \\ U_1 \\ U_2 \\ U_3 \\ U_4 \end{bmatrix} = \begin{bmatrix} 0 \\ 0 \\ b(\Omega_1^2 + \Omega_2^2 + \Omega_3^2 + \Omega_4^2) \\ bl(\Omega_4^2 - \Omega_2^2) \\ bl(\Omega_3^2 - \Omega_1^2) \\ d(-\Omega_1^2 + \Omega_2^2 - \Omega_3^2 + \Omega_4^2) \end{bmatrix} \tag{A.30}$$

Where l $[m]$ is the distance between the CoM of the quad-rotor and the axis of rotation of a propeller. U_1, U_2, U_3 and U_4 are the variable maneuvering vector components. Their relation with the propellers' speeds comes from aerodynamic calculus. The reference for the derivation of the relation is mentioned in Chapter 3 and 5 where the expression of the moment produced by U_4 has been simplified by neglecting the $\dot{\boldsymbol{\Omega}}$ component. Therefore all the movements have a similar expression and make the controller easier to implement.

Therefore from the above relation we can extract the constant maneuver matrix shown in equation (A.31).

$$\Delta_U^b = \begin{bmatrix} 0 & 0 & 0 & 0 \\ 0 & 0 & 0 & 0 \\ b & b & b & b \\ 0 & -bl & 0 & bl \\ -bl & 0 & bl & 0 \\ -d & d & -d & d \end{bmatrix} \tag{A.31}$$

From equation (A.23) it is possible to describe the quad-rotor dynamics considering these last three contributions according to equation (A.32).

$$\Delta_I^b \, \dot{\nu} + \Delta_C^b(\nu) \, \nu = \Delta_g^b(\xi) + \Delta_G^b(\nu) \, \Omega + \Delta_U^b \, \Omega^2 \tag{A.32}$$

By rearranging equation (A.32) it is possible to isolate the derivative of the generalized velocity vector with respect to body-frame as $\dot{\nu}$.

$$\dot{\nu} = (\Delta_I^b)^{-1}(\, -\Delta_C^b(\nu) \, \nu + \Delta_g^b(\xi) + \Delta_G^b(\nu) \, \Omega + \Delta_U^b \, \Omega^2 \,) \tag{A.33}$$

Equation (A.34) shows the previous expression not in a matrix form, but in a form of system equations:

$$
\left.
\begin{aligned}
\dot{v}_x &= (v_y\,\omega_z - v_z\,\omega_y) + g\,\sin\theta \\
\dot{v}_y &= (v_z\,\omega_x - v_x\,\omega_z) - g\,\cos\theta\sin\theta \\
\dot{v}_z &= (v_x\,\omega_y - v_y\,\omega_x) - g\,\cos\theta\sin\phi + \frac{U_1}{m} \\
\dot{\omega}_x &= \frac{I_{YY} - I_{ZZ}}{I_{XX}}\,\omega_y\,\omega_z - \frac{I_r}{I_{XX}}\,\omega_y\,\Omega + \frac{U_2}{I_{XX}} \\
\dot{\omega}_y &= \frac{I_{ZZ} - I_{XX}}{I_{YY}}\,\omega_x\,\omega_z + \frac{I_r}{I_{YY}}\,\omega_x\,\Omega + \frac{U_3}{I_{YY}} \\
\dot{\omega}_z &= \frac{I_{XX} - I_{YY}}{I_{ZZ}}\,\omega_x\,\omega_y + \frac{U_4}{I_{ZZ}}
\end{aligned}
\right\} \qquad \text{(A.34)}
$$

Where the propellers speed inputs are given through equation (A.35)

$$
\left.
\begin{aligned}
U_1 &= b(\Omega_1^2 + \Omega_2^2 + \Omega_3^2 + \Omega_4^2) \\
U_2 &= lb(-\Omega_2^2 + \Omega_4^2) \\
U_1 &= lb(-\Omega_1^2 + \Omega_3^2) \\
U_1 &= d(-\Omega_1^2 + \Omega_2^2 - \Omega_3^2 + \Omega_4^2) \\
\Omega &= -\Omega_1 + \Omega_2 - \Omega_3 + \Omega_4
\end{aligned}
\right\} \qquad \text{(A.35)}
$$

The quad-rotor dynamic system in equation (A.34) is written in the body-fixed frame (O). As stated before, this reference is widely used in 6 DoF rigid-body equations. However in this case it can be convenient to express the dynamics with respect to a mixed frame system composed of linear equations with respect to earth-frame (E) and angular equations with respect to body-frame (O). Therefore the following equations will be expressed in the newly defined "mixed" frame naming as M-frame. This new reference is adopted because it is easy to express the dynamics combined with the control. Equation (A.36) shows the quad-rotor generalized velocity vector

with respect to mixed-frame ($\boldsymbol{\nu^m}$).

$$\boldsymbol{\nu^m} = \begin{bmatrix} \dot{\Gamma}^e & \boldsymbol{\omega^b} \end{bmatrix}^T = \begin{bmatrix} \dot{X} & \dot{Y} & \dot{Z} & \omega_x & \omega_y & \omega_z \end{bmatrix}^T \tag{A.36}$$

The dynamics of the system in the mixed-frame can be rewritten in a matrix form according to equation (A.37).

$$\boldsymbol{\Delta_I^m}\, \dot{\boldsymbol{\nu}}^{\boldsymbol{m}} + \boldsymbol{\Delta_C^m}(\boldsymbol{\nu^m})\, \boldsymbol{\nu^m} = \boldsymbol{\Delta_g^m} + \boldsymbol{\Delta_G^m}(\boldsymbol{\nu^m})\, \boldsymbol{\Omega} + \boldsymbol{\Delta_U^m}(\boldsymbol{\xi})\, \boldsymbol{\Omega^2} \tag{A.37}$$

Where $\dot{\boldsymbol{\nu}}^{\boldsymbol{m}}$ is the quad-rotor generalized acceleration vector with respect to mixed-frame. It now follows the definitions of all the matrices and vectors used in equation(A.37). The system inertia matrix with respect to mixed-frame $\boldsymbol{\Delta_I^m}$ is equal to that one with respect to body-frame and defined according to equations (A.24) and (A.38).

$$\boldsymbol{\Delta_I^m} = \boldsymbol{\Delta_I^b} = \begin{bmatrix} m\boldsymbol{I_{3\times 3}} & \boldsymbol{0_{3\times 3}} \\ \boldsymbol{0_{3\times 3}} & \boldsymbol{I} \end{bmatrix} = \begin{bmatrix} m & 0 & 0 & 0 & 0 & 0 \\ 0 & m & 0 & 0 & 0 & 0 \\ 0 & 0 & m & 0 & 0 & 0 \\ 0 & 0 & 0 & I_{XX} & 0 & 0 \\ 0 & 0 & 0 & 0 & I_{YY} & 0 \\ 0 & 0 & 0 & 0 & 0 & I_{ZZ} \end{bmatrix} \tag{A.38}$$

On the contrary, the Coriolis-centripetal matrix with respect to mixed-frame $\boldsymbol{\Delta_C^m}(\boldsymbol{\nu^m})$ is not equal to that one with respect to body-frame and defined according to equation (A.39).

$$\boldsymbol{\Delta}_{C}^{m}(\boldsymbol{\nu}^{m}) = \begin{bmatrix} \mathbf{0}_{3\times3} & \mathbf{0}_{3\times3} \\ \mathbf{0}_{3\times3} & -\boldsymbol{S}(\boldsymbol{I}\,\boldsymbol{\omega}^{b}) \end{bmatrix} = \begin{bmatrix} 0 & 0 & 0 & 0 & 0 & 0 \\ 0 & 0 & 0 & 0 & 0 & 0 \\ 0 & 0 & 0 & 0 & 0 & 0 \\ 0 & 0 & 0 & 0 & I_{ZZ}\,\omega_z & -I_{YY}\,\omega_y \\ 0 & 0 & 0 & -I_{ZZ}\,\omega_z & 0 & I_{XX}\,\omega_x \\ 0 & 0 & 0 & I_{YY}\,\omega_y & -I_{XX}\,\omega_x & 0 \end{bmatrix} \tag{A.39}$$

The gravitational vector with respect to mixed-frame $\boldsymbol{\Delta}_{g}^{m}$ is defined in equation (A.40). It can be seen that it does not affect all the three linear equations, just the third unlike in the previous case.

$$\boldsymbol{\Delta}_{g}^{m} = \begin{bmatrix} \boldsymbol{F}_{g}^{e} \\ \mathbf{0}_{3\times1} \end{bmatrix} = \begin{bmatrix} 0 \\ 0 \\ -m\,g \\ 0 \\ 0 \\ 0 \end{bmatrix} \tag{A.40}$$

The gyroscopic effects produced by the propeller rotation are unvaried because they affect only the angular equations are referred to the body-frame. Then, the gyroscopic propeller matrix with respect to mixed-frame $\boldsymbol{\Delta}_{G}^{m}(\boldsymbol{\nu}^{m})$ is defined according to equations (A.28) and (A.41).

$$\boldsymbol{\Delta}_G^m(\boldsymbol{\nu}^m)\,\boldsymbol{\Omega} = \boldsymbol{\Delta}_G^b(\boldsymbol{\nu})\,\boldsymbol{\Omega} = \begin{bmatrix} \mathbf{0_{3\times 1}} \\ I_r \begin{bmatrix} -\omega_y \\ \omega_x \\ 0 \end{bmatrix} \Omega \end{bmatrix} = I_r \begin{bmatrix} 0 & 0 & 0 & 0 \\ 0 & 0 & 0 & 0 \\ 0 & 0 & 0 & 0 \\ \omega_y & -\omega_y & \omega_y & -\omega_y \\ -\omega_x & \omega_x & -\omega_x & \omega_x \\ 0 & 0 & 0 & 0 \end{bmatrix} \boldsymbol{\Omega} \tag{A.41}$$

The maneuver matrix with respect to mixed-frame $\boldsymbol{\Delta_U^m(\xi)}$ is different from that one in the body-frame because the input U_1 affects all the three linear equations through the rotation matrix $\boldsymbol{R}$. The product between the movement matrix and the squared propellers' speed vector is shown in equation (A.42).

$$\boldsymbol{\Delta}_U^b(\boldsymbol{\xi})\,\Omega^2 = \begin{bmatrix} \boldsymbol{R} & \mathbf{0_{3\times 3}} \\ \mathbf{0_{3\times 3}} & \boldsymbol{I_{3\times 3}} \end{bmatrix} = \begin{bmatrix} (\sin\phi\sin\psi + \cos\phi\sin\theta\cos\psi)U_1 \\ (-\sin\phi\cos\psi + \cos\phi\sin\theta\sin\psi)U_1 \\ (\cos\phi\cos\theta)U_1 \\ U_2 \\ U_3 \\ U_4 \end{bmatrix} \tag{A.42}$$

By rearranging equation (A.37) it is possible to isolate the derivatives of the generalized velocity vector with respect to mixed-frame:

$$\dot{\boldsymbol{\nu}^m} = (\boldsymbol{\Delta}_I^m)^{-1}(-\boldsymbol{\Delta}_C^m(\boldsymbol{\nu}^m)\,\boldsymbol{\nu}^m + \boldsymbol{\Delta}_g^m + \boldsymbol{\Delta}_G^m(\boldsymbol{\nu}^m)\,\boldsymbol{\Omega} + \boldsymbol{\Delta}_U^m(\boldsymbol{\xi})\,\boldsymbol{\Omega^2}) \qquad \text{(A.43)}$$

Equation (A.44) shows the previous expression not in a matrix form, but in a form of system equations.

$$\left.\begin{aligned}
\ddot{X} &= (\sin\phi\sin\psi + \cos\phi\sin\theta\cos\psi)\,\frac{U_1}{m} \\
\ddot{Y} &= (-\sin\phi\cos\psi + \cos\phi\sin\theta\sin\psi)\,\frac{U_1}{m} \\
\ddot{Z} &= -g + (\cos\phi\cos\theta)\,\frac{U_1}{m} \\
\dot{\omega}_x &= \frac{I_{YY} - I_{ZZ}}{I_{XX}}\,\omega_y\,\omega_z - \frac{I_r}{I_{XX}}\,\omega_y\,\Omega + \frac{U_2}{I_{XX}} \\
\dot{\omega}_y &= \frac{I_{ZZ} - I_{XX}}{I_{YY}}\,\omega_x\,\omega_z + \frac{I_r}{I_{YY}}\,\omega_x\,\Omega + \frac{U_3}{I_{YY}} \\
\dot{\omega}_z &= \frac{I_{XX} - I_{YY}}{I_{ZZ}}\,\omega_x\,\omega_y + \frac{U_4}{I_{ZZ}}
\end{aligned}\right\} \qquad \text{(A.44)}$$

Appendix B

A Brief Introduction to Bond Graph

A bond graph is an energy based domain-independent graphical description of physical systems. This means that systems from different domains (electrical, mechanical, hydraulic, acoustical, thermodynamic) are described in the same way which makes it a powerful tool for modelling engineering systems, especially when different physical domains interact. The modelling is based on the assumption that it is possible to define the characteristics of the systems and subsystems and the connections between the subsystems, and that the exchange of energy between the subsystems goes without losses. The exchange of energy between the subsystems of a more complex system in bond graph modelling is of an essential significance. A bond graph is a directed graph whose nodes represent subsystems and the arrows represent the transfer of energy between the subsystems. The process of dividing into subsystems can go on and on until one ends up with elemental subsystems which can simply be described

by mathematical equations. That is how the hierarchical structure of systems and subsystems in bond graph model is made.

In conventional modeling technique to analyse a system response, one has to derive the mathematical model of the system first and than create a simulation model. However, in bond graph modeling, the system is represented using the flow of energy that takes place among components of a system or from one system to another system in a more intuitive manner. Since they work on the principle of conservation of energy, it is difficult to accidentally introduce extra energy into a system. Due to bidirectional flow of the bonds, systems which produce a 'back force' (e.g. a motor back emf) on the input are easily modelled without introducing extra feedback loops.

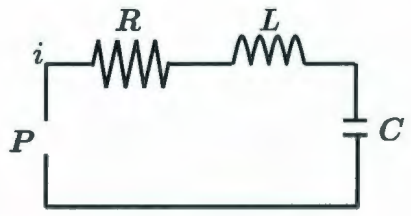

Figure B.1: A Simple RLC Circuit

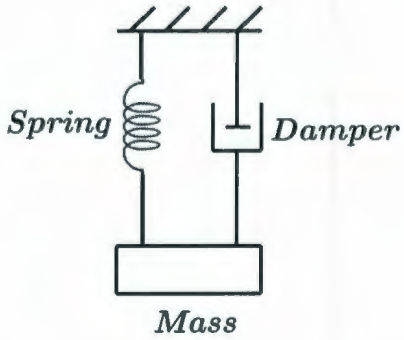

Figure B.2: A Simple Mass-Spring-Damper Arrangement

For example, the electric circuit in Figure B.1 is equivalent to the mechanical mass-spring-damper (MSD) system portrayed in Figure B.2. In this analogy, force in the MSD is the equivalent of voltage (or potential difference) P over the capacitor C, and the velocity is the equivalent of the current i flowing in the electric circuit. These equivalences follow the aforementioned fact of common energy conservation. This

energy always tends to dissipate and thus will flow to anywhere there is presently less energy. For example, a warm room will not cool if all the adjacent rooms are equally warm, whereas it will cool if adjacent rooms are cooler. When there is a flow of energy, there will always be a rate of this flow and a depending on the difference between the energy levels of the place the energy moves from one place to other. In bonds graph language, this difference is referred to as the effort. In this case, the greater the effort, the greater the flow. In an electrical circuit, for example, the rate of flow is referred to as the current and the effort as the voltage (or potential difference); in a mechanical system this rate would be referred to as the velocity and the effort as the force.

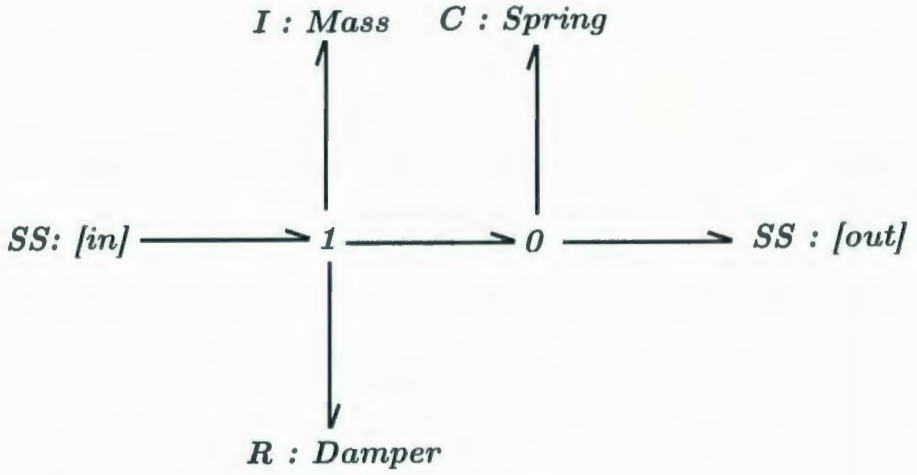

Figure B.3: The Corresponding Bond Graph of the MSD Shown in Figure B.2

A bond graphs model is composed of one or a combination of the following basic elements:

- Energy Source: this can either be a source of flow or a source of effort; for

example, gravity acting on a falling apple.

- Energy Store: this can either store a flow (e.g. a spring or a capacitor) or effort (e.g. mass). The accumulation of either flow or effort variables gives the system its state. The consequence of this is that the systems reaction to a certain input is dependent on the systems previous behaviour.

- Energy Dissipater: this is an element that simply dumps energy out of the system. For example, resistors and friction; both dissipate energy in the form of heat.

- Energy Transfer: these are elements that are responsible for transferring energy within the system. An energy transfer element can be either a junction, a transformer or a gyrator.

There are two types of junctions: the effort junction and the flow junction. In an effort junction (or 0 junction), the effort on the bond coming into the junction is equal to the effort in each of the bonds coming out of the junction (Figure B.4). In a flow junction (or 1 junction) the flow on the bond coming into the junction is equal to the flow in each of the bonds coming out of the junction (Figure B.5).

Although Figures B.4 and B.5 portray only examples using 3-port junctions, the reader should bear in mind that a junction can, in principle, have any number of ports. Transformers and gyrators, however, have only two ports (Figure B.6). The transformer (TR) specifies an output effort e_2 using the relationship $e_2 = k\,e_1$, where k is the transformer ratio. The value of f_2 is then forced to be f_1/k so that $e_1\,f_1 = e_2\,f_2$. The gyrator (GY) is similar to the transformer, except that it specifies the output flow

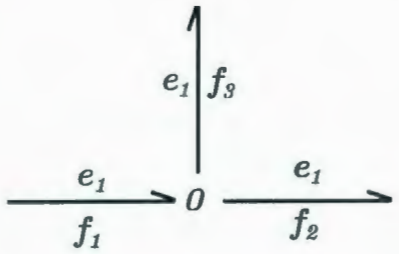

Figure B.4: A Common Effort Junction where
$e_1 f_1 = e_1 f_2 + e_1 f_3$

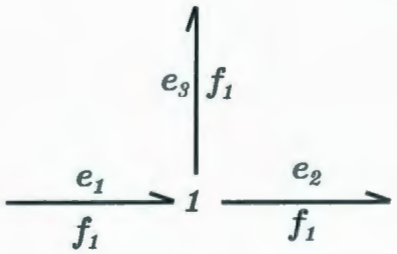

Figure B.5: A Common Flow Junction where
$e_1 f_1 = e_2 f_1 + e_3 f_1$

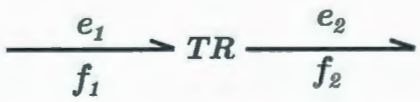

Figure B.6: The Transformer Element

f_2 using the relationship $f_2 = g\, e_1$, where g is referred to as the mutual inductance.

Appendix C

Moment of Inertia Calculation

The moment of inertia describes the dynamic behavior of a body in rotation around a defined axis. It has the same role in rotational dynamics as mass does in basic dynamics. The moment of inertia can be divided in two quantities:

- Scalar moment of inertia
- Moment of inertia tensor

The scalar moment of inertia is defined as:

$$\boldsymbol{I} = \int\int\int_V \rho\, r^2\, dV \tag{C.1}$$

where $\boldsymbol{I}$ $[kgm^2]$ is the moment of inertia, V $[m^3]$ is the volume occupied by the object, ρ $[kgm^{-3}]$ is the spatial density function of the object and r $[m]$ is the (perpendicular) distance of the considered point to the axis of rotation. Since this appendix explains the theory of the moment of inertia, all its variables and constants are not

related to other sections. Therefore they are just initialized and used in this appendix as "stand alone" quantities.

For the same object, different axes of rotation can have different moments of inertia about those axes. The moment of inertia tensor is a convenient way to summarize all moments of inertia of an object with one quantity. The moment of inertia tensor is defined as:

$$\boldsymbol{I} = \begin{bmatrix} I_{XX} & I_{XY} & I_{XZ} \\ I_{YX} & I_{YY} & I_{YZ} \\ I_{ZX} & I_{ZY} & I_{ZZ} \end{bmatrix} \tag{C.2}$$

Here I_{XX} denotes the moment of inertia around the x-axis when the objects are rotated around the x-axis, I_{XY} denotes the moment of inertia around the y-axis when the objects are rotated around the x-axis, and so on.

The following show the moment of inertia calculus for the geometries used in this work mainly the motor inertia and the propeller inertia. In this case motor has been modeled as cylinder and the propeller as a flat plate/solid rectangular prism.

- Solid cylinder with radius R, height H, mass M and a constant density $\rho = \frac{M}{\pi R^2 H}$. Figure C.1 shows the geometry.

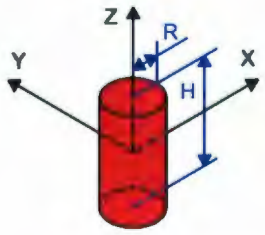

Figure C.1: Model of a Solid Cylinder

$$
\begin{aligned}
I_X &= \int_z \int_y \int_x \rho\,(y^2+z^2)\,dx\,dy\,dz \\
&= \rho \int_{-\frac{H}{2}}^{\frac{H}{2}} \int_{-\frac{R}{2}}^{\frac{R}{2}} \int_{-\sqrt{(\frac{R}{2})^2-y^2}}^{\sqrt{(\frac{R}{2})^2-y^2}} (y^2+z^2)\,dx\,dy\,dz \\
&= \rho \int_{-\frac{H}{2}}^{\frac{H}{2}} \int_0^{2\pi} \int_0^R \left(r^2 \sin^2\theta + z^2\right) r\,dr\,d\theta\,dz \\
&= \rho \left(H \int_0^R r^3\,dr \int_0^{2\pi} \sin^2\theta d\theta + 2\pi \int_0^R r dr \int_{-\frac{H}{2}}^{\frac{H}{2}} z^2 dz \right) \\
&= \frac{M}{\pi R^2 H} \left(H \frac{R^4}{4}\pi + 2\pi \frac{R^2}{2} \frac{H^3}{12} \right) = M \left(\frac{R^2}{4} + \frac{H^2}{12} \right) \qquad \text{(C.3)}
\end{aligned}
$$

$$
\begin{aligned}
I_Y &= \int_z \int_y \int_x \rho\,\left(x^2+z^2\right)\,dx\,dy\,dz = \ldots \\
&= \rho \int_{-\frac{H}{2}}^{\frac{H}{2}} \int_0^{2\pi} \int_0^R \left(r^2 \cos^2\theta + z^2\right) r\,dr\,d\theta\,dz \;= M \left(\frac{R^2}{4} + \frac{H^2}{12} \right) \qquad \text{(C.4)}
\end{aligned}
$$

$$
\begin{aligned}
I_Z &= \int_z \int_y \int_x \rho\,\left(x^2+y^2\right)\,dx\,dy\,dz = \ldots \\
&= \rho \int_{-\frac{H}{2}}^{\frac{H}{2}} \int_0^{2\pi} \int_0^R \left(r^2 \cos^2\theta + r^2 \sin^2\theta\right) r\,dr\,d\theta\,dz \;= M \left(\frac{R^2}{2} \right) \qquad \text{(C.5)}
\end{aligned}
$$

- Solid rectangular prism with length L, width W, height H, mass M, and a constant density $\rho = \frac{M}{L\,W\,H}$. Figure C.2 shows the geometry.

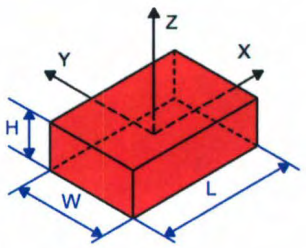

Figure C.2: Model of a Rectangular Prism

$$
\begin{aligned}
I_X &= \int_z \int_y \int_x \rho\,(y^2+z^2)\,dx\,dy\,dz \\
&= \rho \int_{-\frac{H}{2}}^{\frac{H}{2}} \int_{-\frac{W}{2}}^{\frac{W}{2}} \int_{-\frac{L}{2}}^{\frac{L}{2}} (y^2+z^2)\,dx\,dy\,dz \\
&= \rho \left(L\,H \int_{-\frac{W}{2}}^{\frac{W}{2}} y^2 dy + L\,W \int_{-\frac{H}{2}}^{\frac{H}{2}} z^2 dz \right) \\
&= \frac{M}{L\,W\,H} \left(L\,H\,\frac{W^3}{12} + L\,W\,\frac{H^3}{12} \right) = M \left(\frac{W^2}{12} + \frac{H^2}{12} \right) \qquad \text{(C.6)} \\
I_Y &= \int_z \int_y \int_x \rho\,\left(x^2+z^2\right)\,dx\,dy\,dz \\
&= \rho \int_{-\frac{H}{2}}^{\frac{H}{2}} \int_{-\frac{W}{2}}^{\frac{W}{2}} \int_{-\frac{L}{2}}^{\frac{L}{2}} (x^2+z^2)\,dx\,dy\,dz = \cdots = M \left(\frac{L^2}{12} + \frac{H^2}{12} \right) \qquad \text{(C.7)} \\
I_Z &= \int_z \int_y \int_x \rho\,\left(x^2+y^2\right)\,dx\,dy\,dz \\
&= \rho \int_{-\frac{H}{2}}^{\frac{H}{2}} \int_{-\frac{W}{2}}^{\frac{W}{2}} \int_{-\frac{L}{2}}^{\frac{L}{2}} (x^2+y^2)\,dx\,dy\,dz = \cdots = M \left(\frac{L^2}{12} + \frac{W^2}{12} \right) \qquad \text{(C.8)}
\end{aligned}
$$

Appendix D

Blade Element Theory

Blade Element Theory is widely used to calculate aerodynamic forces and torques that act on a rotor. The forces and torques are calculated by integrating the individual forces acting on smaller blade elements over the entire rotor. Figure D.1 shows the model of the propeller section.

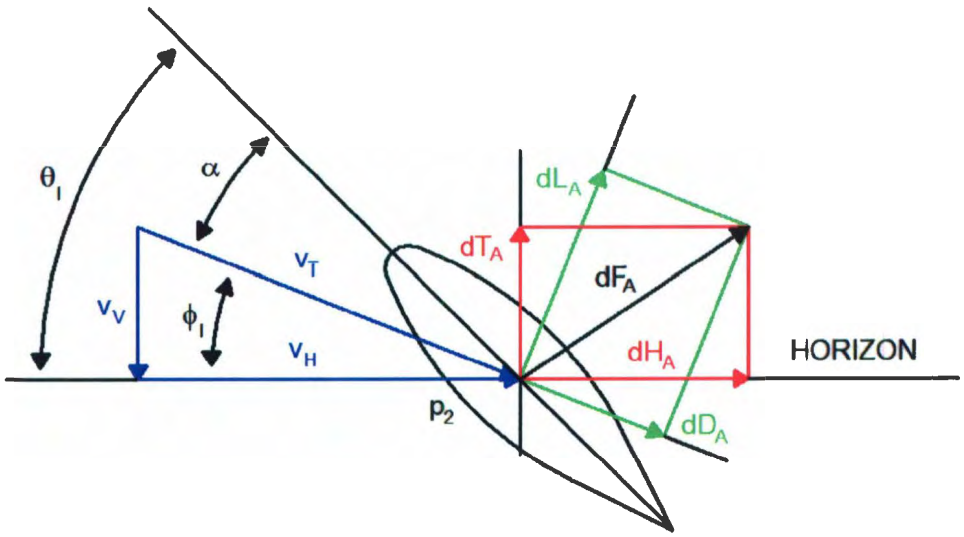

Figure D.1: Blade Element Theory

Here, the "horizon line is perpendicular to the rotor shaft (hovering condition). θ_I $[rad]$ is the angle of incidence between the horizon line and the blade chord line. α $[rad]$ is the angle of attack between the blade chord line and the local air flow velocity vector v_T $[ms^{-1}]$. v_T is the vector sum of the horizontal v_H $[ms^{-1}]$ and vertical v_V $[ms^{-1}]$ air flow velocity. The angle between the horizon and the local velocity vector is the local inflow angle ϕ_I $[rad]$. dD_{BET} $[Nm^{-1}]$ is the infinitesimal drag force while dL_{BET} $[Nm^{-1}]$ is the infinitesimal lift force. The vector sum of dD_{BET} and dL_{BET} is the infinitesimal aerodynamic resultant force dF_{BET} $[Nm^{-1}]$. dF_{BET} can be also be divided into two infinitesimal aerodynamic vertical dT_{BET} $[Nm^{-1}]$ and horizontal dH_{BET} $[Nm^{-1}]$ components.

The v_V velocity vector is due to the inflow motion of the rotor, thus, it is uniform for every section. On the other hand, the v_H velocity is due to the angular speed of the blade element, hence it depends on the radial position of section r $[m]$. The previous statements are simplified according to the hovering hypothesis. Equation D.1 and D.2 shows the velocity components.

$$v_V = \omega_P R_P \lambda \tag{D.1}$$

$$v_H = \omega_P r = \omega_P R_P \left(\frac{r}{R_P}\right) \tag{D.2}$$

Where ω_P $[rads^{-1}]$ is the propeller speed, R_P [m] is the propeller radius and λ is the inflow ratio (a quantity used to relate inflow speed to the rotor tip speed). In order to evaluate λ we need to find v_V using Momentum Theory:

$$v_V = \sqrt{\frac{W_P}{2\,\rho_A\,A}} \tag{D.3}$$

Here, W_P $[N]$ is weight carried by propeller, ρ_A $[kgm^{-3}]$ is the air density and A $= \pi\,R_P^2$ $[m^2]$ is the area of disk created by the propeller. Therefore:

$$\lambda = \frac{v_V}{\omega_P\,R_P} \tag{D.4}$$

To continue with the thrust and torque calculus, a few things have to be taken into consideration. The infinitesimal lift dL_{BET} and dD_{BET} forces according to aerodynamics theory [23], are determined by equations D.5 and D.6.

$$dL_{BET} = \frac{1}{2}\,\rho_A\,v_H^2\,C_L\,c\,dr \tag{D.5}$$

$$dD_{BET} = \frac{1}{2}\,\rho_A\,v_H^2\,C_D\,c\,dr \tag{D.6}$$

Where C_L is the lift coefficient, C_D is the drag coefficient and c $[m]$ is the average chord of the propeller blade. The coefficient of the lift C_L varies linearly with the angle of attack through the lift slope a $[rad\ s^{-1}]$.

$$C_L = a\,\alpha = a\,(\theta_I - \phi_I) \tag{D.7}$$

The blade twist is assumed to vary linearly with radial position. Thus the model includes the two constants zero angle of incidence θ_{I_0} $[rad]$ and twist angle of incidence $\theta_{I_{tw}}$ $[rad]$, according to Equation D.8.

$$\theta_I = \theta_{I_0} - \theta_{I_{tw}} \frac{r}{R_P} \tag{D.8}$$

Furthermore the angular velocity of the blade section is much larger than the total inflow through the blade. Then, small angle approximation can be used to define the inflow angle ϕ_I.

$$\phi_I = \frac{v_V}{v_H} \tag{D.9}$$

According to Equations D.5, D.7, D.8 and D.9; the infinitesimal lift force dL_{BET} can be rewritten as Equation D.10.

$$dL_{BET} = \frac{1}{2} \rho_A v_H^2 a \left(\theta_{I_0} - \theta_{I_{tw}} \frac{r}{R_P} - \frac{v_V}{v_H} \right) c \, dr \tag{D.10}$$

The infinitesimal vertical force dT_{BET} can be simplified considering the previous small angle approximations and that the lift acting on the blade is about an order of magnitude higher than the drag. Equation D.11 shows the approximation.

$$dT_{BET} = dL_{BET}\cos\phi_I - dD_{BET}\sin\phi_I \approx dL_{BET} \tag{D.11}$$

The thrust T_{BET} is finally found by integrating the vertical forces acting on all the blade element sections. The constant N_B identifies the number of blades per propeller.

$$\begin{aligned} T_{BET} &= N_B \int_0^{R_P} \frac{dT_{BET}}{dr}\, dr \\ &= \frac{N_B\,\rho_A\,a\,c}{2} \int_0^{R_P} \left(\theta_{I_0} v_H^2 - \frac{\theta_{I_{tw}}\, r}{R_P} v_H^2 - v_V\, v_H \right) dr \\ &= \frac{N_B\,\rho_A\,a\,c\,\omega_P^2\,R_P^2}{2} \int_0^{R_P} \left(\frac{\theta_{I_0}}{R_P^2}\, r^2 - \frac{\theta_{I_{tw}}}{RP^3}\, r^3 - \frac{\lambda}{R_P}\, r \right) dr \\ &= N_B\,\rho_A\,a\,c\,\omega_P^2\,R_P^3 \left(\frac{\theta_{I_0}}{6} - \frac{\theta_{I_{tw}}}{8} - \frac{\lambda}{4} \right) \end{aligned} \tag{D.12}$$

The infinitesimal horizontal force dH_{BET} can be simplified considering the previous angle approximation, but this case both terms are significant. Equation D.13 shows the approximation.

$$dH_{BET} = dD_{BET}\cos\phi_I + dL_{BET}\sin\phi_I \approx dD_{BET} + dL_{BET}\frac{v_V}{v_H} \tag{D.13}$$

The propeller torque Q_{BET} $[Nm]$ is found by integrating the horizontal forces multiplied by the moment arm on all the blade element sections.

$$
\begin{aligned}
Q_{BET} &= N_B \int_0^{R_P} \left(\frac{dD_{BET}}{dr} + \frac{dL_{BET}}{dr} \frac{v_V}{v_H} \right) dr \\
&= \frac{N_B \rho_A a c}{2} \int_0^{R_P} \left(v_H^2 C_D r + v_V v_H a \theta_{I_0} r - v_V v_H a \frac{\theta_{t_{tw}}}{R_P} r^2 - v_V^2 a r \right) dr \\
&= \frac{N_B \rho_A c \omega_P^2 R_P^2}{2} \int_0^{R_P} \left(\frac{C_D}{R_P^2} r^3 + a \lambda \left(\frac{\theta_{I_0}}{R_P} r^2 - \frac{\theta_{I_{tw}}}{R_P^2} r^3 - \lambda r \right) \right) dr \\
&= N_B \rho_A c \omega_P^2 R_P^4 \left(\frac{C_D}{8} + a \lambda \left(\frac{\theta_{I_0}}{6} - \frac{\theta_{I_{tw}}}{8} - \frac{\lambda}{4} \right) \right) \qquad \text{(D.14)}
\end{aligned}
$$

In order to calculate the aerodynamic values for the quad-rotor helicopter of this work, some constant has been borrowed from [50]

- lift slope, $a = 2\pi$
- drag coefficient, $C_D = 0.05$
- air density, $\rho_A = 1.2\ [kgm^{-3}]$

Rest of the geometric constants obtained from the quad-rotor are:

- Number of blades of a propeller, $N_B = 2$
- Propeller radius, $R_P = 0.155\ [m]$
- Blade chord, $c = 0.02\ [m]$
- Zero angle of incidence of the Blade, $\theta_{I_0} = 20\ [deg] = 0.349\ [rad]$
- Twist angle of incidence, $\theta_{I_{tw}} = 8.6\ [deg] = 0.1511\ [rad]$

Therefore, from Equation D.3 and D.4 we can write,

$$v_V = \sqrt{\frac{W_P}{2\,\rho_A\,A}}$$

$$= \sqrt{\frac{4.375}{2 \times 1.2 \times \pi 0.127^2}} = 5.998\ [ms^{-1}] \tag{D.15}$$

$$\text{and, } \lambda = \frac{v_V}{\omega_P\,R_P}$$

$$= \frac{5.998}{552.9 \times 0.127} = 0.08542 \tag{D.16}$$

Here, W_P is the thrust produced by the propeller while running at a speed of ω_P (from table 6.1). All these values have been utilized in section 6.4 for evaluating the thrust and torque according to Blade Element Theory.